

Simulation of Hypersonic Flowfields Using STAR-CCM+

by
Peter G. Cross and Michael R. West
*Aeromechanics and Thermal Analysis Branch
Weapons Airframe Division*

JANUARY 2019

DISTRIBUTION STATEMENT A. Approved for public release; distribution is unlimited.

NAVAL AIR WARFARE CENTER WEAPONS DIVISION
China Lake, CA 93555-6100

FOREWORD

Engineers in the Aeromechanics and Thermal Analysis Branch at the Naval Air Warfare Center Weapons Division (NAWCWD), China Lake, California, performed computational fluid dynamics simulations of hypersonic flowfield test cases using the STAR-CCM+ flow solver. The analyses presented in this report were completed as part of two discrete science and technology (S&T) projects: the first took place from May through August 2014 and the second from June through September 2018. This two-part effort validated the ability of the STAR-CCM+ flow solver to predict hypersonic flows with acceptable accuracy. Lessons learned and recommended best practices are documented herein, making this report a valuable resource that can be used to guide future hypersonic flow simulations to a rapid and accurate completion.

This report was reviewed for technical accuracy by Joe-Ray Gramanzini.

S. BARLOW, *Head*
Weapons Airframe Division
23 January 2019

REPORT DOCUMENTATION PAGE			<i>Form Approved</i> OMB No. 0704-0188	
The public reporting burden for this collection of information is estimated to average 1 hour per response, including the time for reviewing instructions, searching existing data sources, gathering and maintaining the data needed, and completing and reviewing the collection of information. Send comments regarding this burden estimate or any other aspect of this collection of information, including suggestions for reducing the burden, to the Department of Defense, Executive Service Directorate (0704-0188). Respondents should be aware that notwithstanding any other provision of law, no person shall be subject to any penalty for failing to comply with a collection of information if it does not display a currently valid OMB control number. PLEASE DO NOT RETURN YOUR FORM TO THE ABOVE ORGANIZATION.				
1. REPORT DATE (DD-MM-YYYY) 23-01-2019		2. REPORT TYPE Final		3. DATES COVERED (From - To) 1 May 2014 – 30 September 2018
4. TITLE AND SUBTITLE Simulation of Hypersonic Flowfields Using STAR-CCM+ (U)			5a. CONTRACT NUMBER N/A	
			5b. GRANT NUMBER N/A	
			5c. PROGRAM ELEMENT NUMBER N/A	
6. AUTHOR(S) Peter G. Cross and Michael R. West			5d. PROJECT NUMBER N/A	
			5e. TASK NUMBER N/A	
			5f. WORK UNIT NUMBER N/A	
7. PERFORMING ORGANIZATION NAME(S) AND ADDRESS(ES) Naval Air Warfare Center Weapons Division 1 Administration Circle China Lake, California 93555-6100			8. PERFORMING ORGANIZATION REPORT NUMBER NAWCWD TM 8824	
9. SPONSORING/MONITORING AGENCY NAME(S) AND ADDRESS(ES) Naval Air Warfare Center Weapons Division 1 Administration Circle China Lake, California 93555-6100			10. SPONSOR/MONITOR'S ACRONYM(S) N/A	
			11. SPONSOR/MONITOR'S REPORT NUMBER(S) N/A	
12. DISTRIBUTION/AVAILABILITY STATEMENT DISTRIBUTION STATEMENT A. Approved for public release; distribution is unlimited.				
13. SUPPLEMENTARY NOTES None.				
14. ABSTRACT (U) See next page.				
15. SUBJECT TERMS Computational Fluid Dynamics, Cone-Flare, Cylinder-Flare, Double Cone, Hypersonic Flowfields, Shock/Boundary Layer Interaction, Shock/Shock Interaction, STAR-CCM+				
16. SECURITY CLASSIFICATION OF:			17. LIMITATION OF ABSTRACT SAR	18. NUMBER OF PAGES 116
a. REPORT UNCLASSIFIED	b. ABSTRACT UNCLASSIFIED	c. THIS PAGE UNCLASSIFIED		
			19b. TELEPHONE NUMBER (include area code) (760) 939-8433	

14. ABSTRACT (CONTD.)

(U) Hypersonic flowfields are characterized by high temperature physical processes that are dormant in lower speed regimes. Recent versions of the commercial off-the-shelf flow solver STAR-CCM+ include models for many of the high temperature physical processes relevant to hypersonic flow. However, before the results produced from these new models can be fully trusted, it is necessary to validate the simulations against experimental data. It is also necessary to establish a set of best practices to guide the most efficient and successful use of the STAR-CCM+ software when simulating hypersonic flows.

(U) The report documents a research effort with the simultaneous goals of (1) validating the capabilities of STAR-CCM+ and (2) establishing best practices for using STAR-CCM+ to simulate hypersonic flows.

(U) Selected test case geometries include the double cone and short hollow cylinder-flare (shock/laminar boundary layer interactions), the cone-flare and large hollow cylinder-flare (shock/turbulent boundary layer interactions), and a shock/shock interaction test case. Agreement with the experiments is sufficient to validate the hypersonic capabilities in STAR-CCM+. Additionally, results produced by STAR-CCM+ are typically equivalent to or better than those obtained using specialized solvers. Best practice recommendations are documented and can be used to guide future hypersonic flow simulations to a rapid and accurate completion.

CONTENTS

Executive Summary 7

1.0 Introduction..... 9

 1.1 Objective 9

 1.2 Scope..... 9

 1.3 Background 10

2.0 Test Cases 12

 2.1 Double Cone 13

 2.2 Small Cylinder-Flare..... 17

 2.3 Cone-Flare..... 18

 2.4 Large Cylinder-Flare..... 21

 2.5 Shock/Shock Interaction 22

3.0 Methodology 25

 3.1 Air Property Models..... 25

 3.1.1 One Species Air Model 26

 3.1.2 Two Species Air Model..... 26

 3.1.3 Five Species Air Model 27

 3.1.4 Equilibrium Air Model..... 28

 3.2 Solver Settings 28

 3.3 Boundary Conditions 31

 3.4 Initial Conditions..... 32

 3.5 Mesh..... 33

 3.5.1 Structured Directed Mesh..... 33

 3.5.2 Pressure Gradient Mesh Refinement 35

 3.5.3 Normalized Pressure Gradient Mesh Refinement 39

4.0 Results..... 43

 4.1 Double Cone 43

 4.1.1 FY14 Effort 43

 4.1.2 FY18 Effort 60

 4.2 Small Cylinder-Flare..... 70

 4.3 Cone-Flare..... 78

 4.3.1 FY14 Effort 78

 4.3.2 FY18 Effort 82

 4.4 Large Cylinder-Flare..... 91

 4.5 Shock/Shock Interaction 100

5.0 Lessons Learned and Recommendations 105

6.0 Conclusions..... 109

References..... 112

Nomenclature..... 115

Figures:

1. Temperature Effects on Air 11

2. Geometry for 25-/55-Degree Double Cone Configuration..... 13

3. Geometry for Small, Hollow Cylinder-Flare Configuration..... 17

4. Geometry for 6-/42-Degree Cone-Flare Configuration 19

5. Geometry for 7-/40-Degree Cone-Flare Configuration 19

6. Geometry for Large, Hollow Cylinder-Flare Configuration..... 21

7. Schematic of Shock/Shock Interaction Test Case Geometry 23

8. Illustration of Structured Directed Mesh Used for FY14 Simulations of
Double Cone Test Case..... 34

9. Example of Mesh Refinement Using Initial Pressure Gradient Technique..... 36

10. Cell Refinement Flag Computed From Baseline Solution for
Shock/Shock Interaction Test Case 38

11. Example of Mesh Refinement Using Normalized Pressure
Gradient Technique..... 41

12. Example of Normalized Pressure Gradient Mesh Refinement Applied to
Three-Dimensional Simulation of Waverider..... 42

13. Flowfield Around Waverider Computed Using Refined Mesh 43

14. Heat Flux Convergence Behavior for Single Species, Thermal
Equilibrium Simulation of Double Cone Run 80 46

15. Heat Flux as Predicted by Single Species, Thermal Equilibrium
Simulation of Double Cone Run 80, Compared to
Experimental Measurements..... 46

16. Averaged Temperature, Mach Number, and Velocity as Predicted
by Single Species, Thermal Equilibrium Simulation of
Double Cone Run 80..... 47

17. Detailed View of Flow Separation as Predicted by Single Species,
Thermal Equilibrium Simulation of Double Cone Run 80..... 48

18. Heat Flux as Predicted by Single Species, Thermal Nonequilibrium
Simulation of Double Cone Run 80, Compared to
Experimental Measurements..... 49

19. Averaged Translation-Rotational and Vibrational-Electronic
Temperature and Mach Number as Predicted by Single Species,
Thermal Nonequilibrium Simulation of Double Cone Run 80..... 50

20. Comparison of Vibrational-Electronic Temperature Predicted by Single
and Multiple Species Simulations for Double Cone Run 80 51

21. Detailed View of Translational-Rotational and Vibrational-Electronic Temperatures in Separated Flow Region as Predicted by Multiple Species, Thermal Nonequilibrium Simulation for Double Cone Run 80 52

22. Comparison of Heat Flux as Predicted by Different Simulations for Double Cone Run 80..... 53

23. Comparison of Temperature Distribution as Predicted by Different Simulations for Double Cone Run 80..... 54

24. Detail of Flowfield Near Separation Bubble for Equilibrium and Nonequilibrium Single Species Simulations for Double Cone Run 80..... 55

25. Heat Flux as Predicted by Equilibrium Air Simulation of Double Cone Run 39, Compared to Experimental Measurements 56

26. Primary and Secondary Flow Separation Bubbles Predicted by Equilibrium Air Simulation of Double Cone Run 39 56

27. Heat Flux as Predicted by Multiple Species, Non-Reacting Simulation of Double Cone Run 39, Compared to Experimental Measurements 57

28. Heat Flux as Predicted by Multiple Species, Reacting Simulation of Double Cone Run 39, Compared to Experimental Measurements 58

29. Comparison of Heat Flux as Predicted by Different Simulations for Double Cone Run 39..... 58

30. Comparison of Temperature Distribution as Predicted by Different Simulations for Double Cone Run 39..... 59

31. Mass Fraction Distribution for Dissociation Product Species as Predicted by Multiple Species, Reacting Simulation of Double Cone Run 39 60

32. Numerical Schlieren Images of Flowfield Predicted for Double Cone Run 1..... 61

33. Heat Flux Distribution for Double Cone Run 1 as Predicted Using Five Species Air Model, Compared to Experimental Measurements..... 62

34. Pressure Distribution for Double Cone Run 1 as Predicted Using Five Species Air Model, Compared to Experimental Measurements..... 62

35. Numerical Schlieren Images of Flowfield Predicted for Double Cone Runs 2, 3, and 5 63

36. Heat Flux Distribution for Double Cone Run 2 as Predicted Using Five Species Air Model, Compared to Experimental Measurements..... 64

37. Pressure Distribution for Double Cone Run 2 as Predicted Using Five Species Air Model, Compared to Experimental Measurements..... 64

38. Heat Flux Distribution for Double Cone Run 3 as Predicted Using Five Species Air Model, Compared to Experimental Measurements..... 65

39. Pressure Distribution for Double Cone Run 3 as Predicted Using Five Species Air Model, Compared to Experimental Measurements..... 65

40. Heat Flux Distribution for Double Cone Run 5 as Predicted Using Five Species Air Model, Compared to Experimental Measurements..... 67

41. Pressure Distribution for Double Cone Run 5 as Predicted Using Five Species Air Model, Compared to Experimental Measurements..... 67

42. Temperature of Two Energy Modes, as Predicted for Double Cone Run 3..... 68

43. Species Mass Fractions, as Predicted for Double Cone Run 3 69

44. Numerical Schlieren Images of Flowfield Predicted for Small Cylinder-Flare Test Cases 72

45. Heat Flux Distribution for Small Cylinder-Flare Run 1 as Predicted Using Five Species Air Model, Compared to Experimental Measurements..... 73

46. Pressure Distribution for Small Cylinder-Flare Run 1 as Predicted Using Five Species Air Model, Compared to Experimental Measurements..... 73

47. Heat Flux Distribution for Small Cylinder-Flare Run 2 as Predicted Using Five Species Air Model, Compared to Experimental Measurements..... 74

48. Pressure Distribution for Small Cylinder-Flare Run 2 as Predicted Using Five Species Air Model, Compared to Experimental Measurements..... 74

49. Heat Flux Distribution for Small Cylinder-Flare Run 3 as Predicted Using Five Species Air Model, Compared to Experimental Measurements..... 75

50. Pressure Distribution for Small Cylinder-Flare Run 3 as Predicted Using Five Species Air Model, Compared to Experimental Measurements..... 75

51. Heat Flux Distribution for Small Cylinder-Flare Run 4 as Predicted Using Five Species Air Model, Compared to Experimental Measurements..... 76

52. Pressure Distribution for Small Cylinder-Flare Run 4 as Predicted Using Five Species Air Model, Compared to Experimental Measurements..... 76

53. Heat Flux Distribution for Small Cylinder-Flare Run 5 as Predicted Using Five Species Air Model, Compared to Experimental Measurements..... 77

54. Pressure Distribution for Small Cylinder-Flare Run 5 as Predicted Using Five Species Air Model, Compared to Experimental Measurements..... 77

55. Stanton Number as Predicted by Cone-Flare Run 4 Simulations Employing Four Different Turbulence Models, Compared to Experimental Measurements..... 80

56. Pressure Ratio as Predicted by Cone-Flare Run 4 Simulations Employing Four Different Turbulence Models, Compared to Experimental Measurements..... 80

57. Comparison of Mach Number Distributions as Predicted by Cone-Flare Run 4 Simulations Employing Four Different Turbulence Models 81

58. Comparison of Velocity Field in Vicinity of Cone-Flare Junction as Predicted by Cone-Flare Run 4 Simulations Employing Four Different Turbulence Models 81

59. Stanton Number as Predicted by Select FY18 6-/42-Degree Cone-Flare Run 4 Simulations, Compared to Experimental Measurements 86

60. Pressure Ratio as Predicted by Select FY18 6-/42-Degree Cone-Flare Run 4 Simulations, Compared to Experimental Measurements 86

61. Numerical Schlieren Images of the Flowfield as Predicted by Select FY18 6-/42-Degree Cone-Flare Run 4 Simulations 87

62. Heat Flux Distribution Predictions for 7-/40-Degree Cone-Flare Run 33, Compared to Experimental Measurements 88

63. Pressure Distribution Predictions for 7-/40-Degree Cone-Flare Run 33, Compared to Experimental Measurements 88

64. Numerical Schlieren Images of Flowfield Predicted for 7-/40-Degree Cone-Flare Run 33 89

65. Numerical Schlieren Images of Flowfield Predicted for 7-/40-Degree Cone-Flare Run 45 89

66. Heat Flux Distribution Predictions for 7-/40-Degree Cone-Flare Run 45, Compared to Experimental Measurements 90

67. Pressure Distribution Predictions for 7-/40-Degree Cone-Flare Run 45, Compared to Experimental Measurements 90

68. Numerical Schlieren Images of Flowfield Predicted for Large Cylinder-Flare Run 18 93

69. Heat Flux Distribution Predictions for Large Cylinder-Flare Run 18, Compared to Experimental Measurements 94

70. Pressure Distribution Predictions for Large Cylinder-Flare Run 18, Compared to Experimental Measurements 94

71. Numerical Schlieren Images of Flowfield Predicted for Large Cylinder-Flare Run 11 96

72. Heat Flux Distribution Predictions for Large Cylinder-Flare Run 11, Compared to Experimental Measurements 97

73. Pressure Distribution Predictions for Large Cylinder-Flare Run 11, Compared to Experimental Measurements 97

74. Numerical Schlieren Images of Flowfield Predicted for Large Cylinder-Flare Run 13 98

75. Heat Flux Distribution Predictions for Large Cylinder-Flare Run 13, Compared to Experimental Measurements 99

76. Pressure Distribution Predictions for Large Cylinder-Flare Run 13, Compared to Experimental Measurements 99

77. Numerical Schlieren Images of Flowfield as Predicted for Shock/Shock Test Case Runs 103 and 59 101

78. Numerical Schlieren Images of Flowfield as Predicted by Shock/Shock Run 60 Simulations 102

79. Temperature and Velocity Predictions as Predicted by Nonequilibrium Simulation of Shock/Shock Run 60 Test Case 103

80. Heat Flux Distribution Predictions for Shock/Shock Run 60, Compared to Experimental Measurements 104

81. Pressure Distribution Predictions for Shock/Shock Run 60,
Compared to Experimental Measurements 104

Tables:

1. Freestream Conditions for Double Cone Cases Considered in FY14 Effort ... 15
2. Freestream Conditions for Double Cone Cases Considered in FY18 Effort ... 17
3. Freestream Conditions for Small, Hollow Cylinder-Flare Test Cases 18
4. Freestream Conditions for 6-/42- and 7-/40-Degree Cone-Flare Cases 20
5. Freestream Conditions for Large, Hollow Cylinder-Flare Test Cases 22
6. Geometry and Freestream Conditions for Shock/Shock Interaction Cases 24
7. Specific Heat Polynomial Coefficients for Air 26
8. Forward Reaction Rates for Dunn/Kang Mechanism 28
9. Flow Separation Position, in Inches, for Small Cylinder-Flare Test Cases 71
10. Summary of 6-/42-Degree Cone-Flare Turbulence Model Investigation 83

EXECUTIVE SUMMARY

Hypersonic flight (i.e., flight in excess of Mach 5) produces high temperatures that activate certain physical processes, including temperature-dependent properties, thermodynamic nonequilibrium, dissociation, and ionization, normally dormant for slower flight regimes. When simulating hypersonic flow, it is very important to model these additional physical processes, which require the inclusion of specialized models into the flow solver. However, the resultant simulations are much more challenging to solve than typical lower speed flow problems. As a result, the common practices used for simulating lower speed flows are often unsuitable when applied to the higher speed problem. Thus, both new tools and new practices are needed in order to be able to accurately predict hypersonic flows.

Recent versions of the commercial off-the-shelf (COTS) flow solver STAR-CCM+ include models for many of the high temperature physical processes relevant to hypersonic flow. However, before the results produced from these new models can be fully trusted, it is necessary to validate the simulations against experimental data. It is also necessary to establish a set of best practices to guide the most efficient and successful use of the STAR-CCM+ software when simulating hypersonic flows.

To address these needs, the activity described in this report has two main objectives. The first is to investigate the capabilities and the suitability of the STAR-CCM+ flow solver to simulate hypersonic flowfields. This is accomplished by attempting simulations of multiple test cases and comparing the predictions to experimental data, thus validating the accuracy of STAR-CCM+. The second goal is to establish best practices for using STAR-CCM+ to simulate hypersonic flowfields with thermodynamic nonequilibrium and chemical reactions. This is accomplished by documenting lessons learned, the successes, and the failures encountered during the execution of this effort.

In this effort, numerous hypersonic test cases are simulated, with selected test case geometries including the double cone and short hollow cylinder-flare (investigating shock/laminar boundary layer interactions), the cone-flare and large hollow cylinder-flare (investigating shock/turbulent boundary layer interactions), and a shock/shock interaction test case. Agreement with the experiments is not perfect but is sufficient to validate the hypersonic capabilities in STAR-CCM+. Additionally, results produced by STAR-CCM+ are typically equivalent, and in some cases are superior, to results obtained by other analysts using specialized, research-oriented flow solvers. Based on the lessons learned in the course of completing these simulations, best practices have been established. These recommendations are documented in this report and can be used to guide future hypersonic flow simulations to a rapid and accurate completion.

This page intentionally left blank.

1.0 INTRODUCTION

1.1 OBJECTIVE

The objective of this effort is to investigate the capabilities and suitability of using a commercial off-the-shelf (COTS) computational fluid dynamics (CFD) software package (specifically, the STAR-CCM+ program) for simulating hypersonic flowfields. Of particular interest in this work are flowfields involving shock/shock interactions, shock/boundary layer interactions, and flow separation, as these physical phenomena are particularly challenging to simulate accurately, yet can have a large impact on the design of a hypersonic flight vehicle.

The goal for this work is to determine if the physics models available in the STAR-CCM+ software package, which is the preferred CFD solver extensively employed by the Aeromechanics and Thermal Analysis Branch, are capable of modeling the additional important physical processes that become active in the hypersonic flow regime. Should the STAR-CCM+ solver be found suitable, a secondary goal of this effort is to establish a set of best practices to follow when simulating hypersonic flows with this solver.

Future analyses of hypersonic flight vehicles can leverage the lessons learned in this effort and use the identified best practices to produce high-quality analysis results with a rapid turnaround time and reduced learning curve. This will in turn increase the capability of the Aeromechanics and Thermal Analysis Branch and the Naval Air Warfare Center Weapons Division (NAWCWD) to participate in the design and analysis of hypersonic weapons and flight vehicles.

1.2 SCOPE

This report documents work performed as part of two discrete science and technology (S&T) projects: one performed in fiscal year 2014 (FY14) and a subsequent project in FY18. The goals of the two periods of activity were largely the same: investigate the capability of the STAR-CCM+ flow solver to simulate hypersonic flows and to establish best practices. Due to the similar nature of these two activities, and since the FY14 project had not been previously documented in an official report, the results from both projects are included in this report.

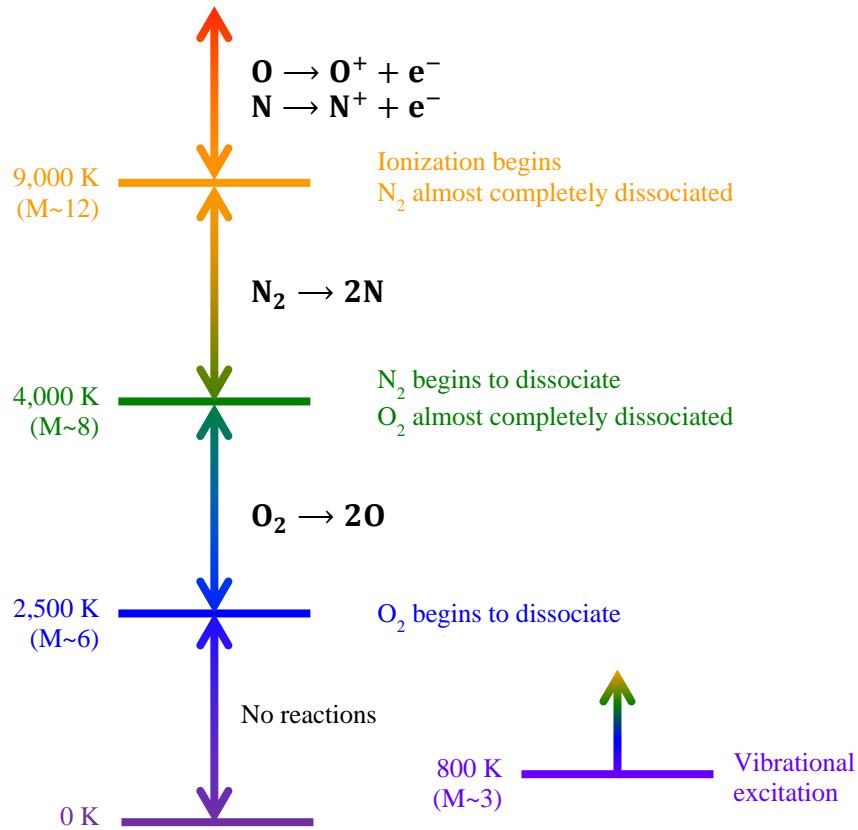
The FY14 effort revealed that STAR-CCM+ has some capability for modeling hypersonic flows but also identified some shortcomings and challenges that needed to be resolved before the STAR-CCM+ solver could be used to perform routine, production simulations of hypersonic flows. Unfortunately, due to the limited time and resources available for the FY14 effort, it was not possible at that time to investigate these issues further. However, the FY14 effort laid important groundwork for the FY18 project.

The intent of the FY18 effort is to build upon the lessons learned and to try to resolve some of the challenges identified in the earlier effort. Several of the test cases explored in the FY14 effort are revisited, but new test cases are also investigated. A newer version of the STAR-CCM+ software is used in the FY18 effort, which is expected to have increased capability and performance relative to the version used in FY14. Another significant difference is that the FY18 largely uses unstructured meshes adapted to the flow solution, while the FY14 effort predominantly used structured meshes.

1.3 BACKGROUND

Hypersonic flow is generally taken to be flow at Mach numbers in excess of 5 but is more appropriately defined as the flow regime where certain physical phenomena that are dormant at lower speeds have increasing importance. These characteristic phenomena include thin shock layers, viscous interactions, temperature-dependent properties, nonequilibrium effects, chemistry, and ionization (Reference 1). Because of these additional physical processes, hypersonic flows are significantly more challenging to simulate than conventional subsonic or supersonic flows. As a result, the numerical models, methods, and best practices used to successfully obtain predictions for lower speed flows are insufficient to handle the complexities posed by hypersonic flow.

The large kinetic energy associated with hypersonic flight leads to very large temperatures behind shock waves and in the boundary layers adjacent to vehicle walls. These high temperatures lead to the activation of physical processes (see Figure 1, reproduced after Figure 9.12 in Reference 1) that are unimportant at the lower temperatures associated with lower speed flows. The vibrational energy mode for diatomic molecules (O_2 , N_2) becomes excited at temperatures above 800 K (approximately Mach 3), leading to temperature-dependent thermal properties. At even higher temperatures, chemistry takes place (predominantly dissociation reactions), with oxygen beginning to dissociate at 2,500 K (about Mach 6) and dissociation of nitrogen beginning at 4,000 K (near Mach 8). Ionization of air begins at around 9,000 K (approximately Mach 12), leading to the formation of a plasma.



Note: Mach numbers are approximations.

FIGURE 1. Temperature Effects on Air.

Vibrational excitation and chemical reactions are finite-rate processes, with the time required for completion related to the collision frequency of the gas molecules (and thus a function of density). For low-speed and high-density flows, the characteristic times associated with completion of excitation or reactions are quite small compared to the characteristic time of the flow. These relaxation processes therefore occur almost instantaneously within the thickness of a shock wave, and the flow can be assumed to be in thermodynamic and chemical equilibrium. However, at very high flow speeds and at low densities, the flow characteristic time becomes comparable to the relaxation characteristic time. Under these conditions, the flow immediately downstream of shocks is in thermodynamic and chemical nonequilibrium, with the vibrational excitation and chemical reactions processes not reaching completion until a significant distance downstream of the shock. Nonequilibrium effects can be particularly important for hypersonic vehicles flying at high altitudes. Simulation of hypersonic flows with thermochemical nonequilibrium remains a very active area of research.

Another characteristic of the flow around hypersonic flight vehicles is the interaction of multiple shocks and the interaction of shocks with boundary layers. These interactions can have a very strong impact on the aeroheating experienced by the flight vehicle. The heat flux in the vicinity of these interactions can be many times greater than that experienced away from the interaction region, leading to strong, localized heating. Flow separation, and the subsequent reattachment of the flow, can also be induced by these shock interactions. The occurrence of flow separation and the size of the region of separated flow also strongly affect the aeroheating experienced by a hypersonic vehicle. Historically, predicting the magnitude and extent of flow separation has been extremely challenging; this is still an area of active research.

In order to be able to accurately predict hypersonic flowfields, these additional physical processes (vibrational excitation, chemistry, nonequilibrium, shock/shock and shock/boundary layer interactions, and flow separation) must be captured correctly in the simulations. The STAR-CCM+ flow solver used by the Aeromechanics and Thermal Analysis Branch contains a number of relatively new physical models that are advertised as being capable of modeling these processes. However, before this tool can be relied upon, it must be validated and shown to produce accurate results. Additionally, before hypersonic simulations can be completed quickly and cost-effectively, experience needs to be gained with these advanced physics models. Best practices also need to be established to ensure quality analysis results. The goals of this effort are to provide validation of the hypersonic physics models in STAR-CCM+, to gain the necessary experience with these features, and to establish a set of best practices.

By improving the ability to accurately predict these separated hypersonic flowfields, it will be possible to greatly reduce the uncertainty associated with the aeroheating experienced by a high-speed weapons system. By reducing this uncertainty, it will be possible to develop refined, more optimized weapon designs that can survive these conditions. These optimized concepts would also provide more performance than can be obtained from a system that has been over-designed with conservatism to address these uncertainties.

2.0 TEST CASES

A survey of the literature is performed to identify appropriate hypersonic test cases for which experimental data are available. A discussion of the key features of each of these test cases is given in this section. Wherever possible, the test runs deemed most suitable for simulation validation comparisons have been identified.

Some of the best hypersonic test cases available appear to have been performed in facilities at the Calspan-University at Buffalo Research Center (CUBRC). A large number of experiments have been performed for a wide range of model geometries. The data collected also appear to be quite extensive, including pressure and heat transfer

measurements along the length of the model. Unfortunately, documentation for these experiments is surprisingly poor. A single paper often describes multiple test campaigns; likewise a single test campaign can be found discussed in multiple papers. Occasionally, citations refer to documents that were apparently never made available in the open literature. Most concerning is that different freestream values are sometimes reported in different papers for the same test run. Freestream conditions and experimental measurements do not appear to be available in the open literature for many test runs; it appears necessary to contact the experimentalists directly in order to obtain these data. An attempt has been made to sift through this sometimes conflicting information to identify the test runs that are most thoroughly described and are therefore the best candidates for validation cases.

2.1 DOUBLE CONE

One model geometry that has been explored quite extensively by CUBRC across multiple test campaigns over the years is the 25-/55-degree double cone configuration, illustrated in Figure 2. Most test runs were performed using a sharp nose, though a few select tests investigated the effects of different nose bluntness values. The compression corner on this model typically produces a large region of separated flow. However, the boundary layer remains laminar even after reattachment of this separated flow, making this a particularly valuable test case.

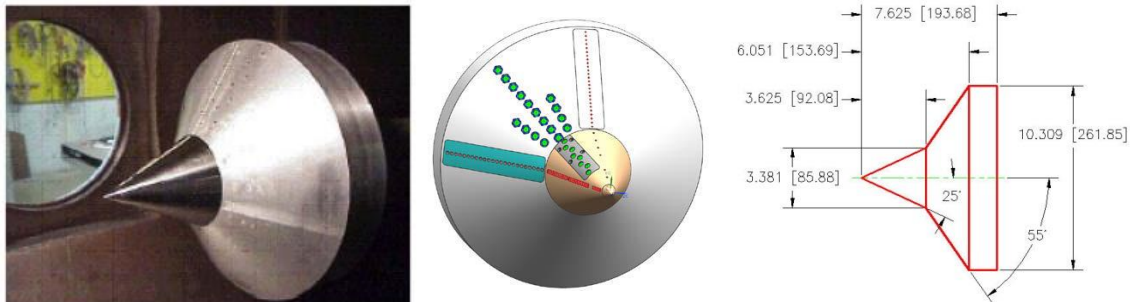


FIGURE 2. Geometry for 25-/55-Degree Double Cone Configuration.

A good overview of the earlier test campaigns performed with this model is presented in Reference 2. Additional information on one of the earliest test campaigns is given in References 3 and 4. Detailed freestream conditions are not available in the American Institute of Aeronautics and Astronautics (AIAA) paper (Reference 3) but are included in the North Atlantic Treaty Organization (NATO) report (Reference 4). Unfortunately, there is disagreement between the two references for the freestream Mach and Reynolds numbers. Due to the quality of writing and due to the fact that it is the more recent document, values presented by the NATO report are believed to be more reliable. Freestream Mach numbers ranged from 10.3 to 12.5. The working fluid for these experiments was nitrogen in order to avoid the effects of the dissociation of oxygen.

Sharp and blunt-nosed geometries were investigated. The experimental measurements were only presented graphically and were not tabulated.

Comparisons were made between the experimental measurements and computational results obtained by solving the Navier-Stokes equations as well as by using a direct simulation Monte-Carlo (DSMC) technique. Remarkably good agreement was obtained between CFD and experiments for run 28. Otherwise, the tendency was for the Navier-Stokes solutions to slightly under-predict the size of the separation bubble (flow was predicted to separate farther aft than was observed experimentally), which affected the predictions of peak pressure and heat transfer at the reattachment point. Agreement between the experiments and the DSMC solutions was quite poor, with the DSMC simulations predicting very small separation bubbles. This discrepancy was attributed to the relatively high density of the flow, which poses challenges to the DSMC technique.

To address these challenges, a subsequent test campaign was performed to investigate lower density flows (References 2 and 5). Navier-Stokes simulations agreed well with the experimental measurements, with the inclusion of a slip wall boundary condition leading to improved agreement for the heat flux upstream of the separation on the first cone and downstream of the reattachment on the second cone. The DSMC solutions agreed much better with the experimental measurements, though the size of the separation bubble was still under-predicted.

While most of the double cone experiments were conducted at zero degrees angle of attack (thus producing an axisymmetric flowfield), one test campaign did consider the double cone model at 2 degrees angle of attack (References 2 and 6). This resulted in three-dimensional flow interactions. One simulation predicted separation on the leeward side in good agreement with the experiment but another solution under-predicted the leeward separation. The extent of flow separation on the windward side of the model was always under-predicted.

The experimental campaigns described thus far appear to have only considered nitrogen as the test gas and were conducted at relatively low total enthalpies. To explore the effects of increased flow nonequilibrium (especially dissociation), a test campaign was conducted that explored nitrogen, air, and oxygen/argon mixtures as the test gases, and also included experiments with increased flow total enthalpy (References 2, 7, and 8). These experiments are discussed extensively in Reference 7, and the measurements are presented graphically in non-dimensional form. The freestream conditions are also tabulated but differ from the values reported in Reference 8. Because it is the more recent paper, the values presented in Reference 8 are considered to be preferred. Tabulated heat flux measurements are also provided in Reference 8; units are not given in the paper but have been determined to be $\text{btu}/\text{ft}^2\text{s}$. Heat flux measurements are reported to be accurate within $\pm 6\%$; pressure measurement accuracy is reported as $\pm 4\%$ (Reference 7).

Freestream conditions and heat flux measurements are available for three runs considering pure nitrogen (runs 40, 42, and 80), two runs with air (runs 39 and 43), and

two runs for pure oxygen (runs 90 and 91). Simulations of run 40 yielded unsteady flow, even though the flow in the experiment was observed to be steady. To investigate this, run 80 was performed with reduced density; the resultant simulations showed steady flow (Reference 2). Run 80 is therefore preferred over run 40 as a test case. Experiments performed at lower enthalpy values (runs 39, 80, and 90) were not expected to produce significant dissociation (Reference 7). At these lower enthalpy values there was little difference in the size of the separation bubble for nitrogen or air. Increasing flow enthalpy was found to reduce the size of the separation bubbles. The impact of flow enthalpy on the size of the separation bubble was much larger for air than it was for nitrogen. A few additional runs were also performed for models with a blunt nose. Nose bluntness did not appear to have made a significant impact on the results.

Because of the large amount of data available, and because the lower enthalpy cases were reported to be easier to simulate, run 80 (nitrogen) and run 39 (air) were selected as the primary validation cases for the FY14 effort. The freestream conditions for these runs are given in Table 1. Most values were taken from Reference 8 but wall temperature was only available in Reference 7; wall temperature for run 80 was assumed to be the same as that for run 40. Mach number and pressure were computed from the other properties.

TABLE 1. Freestream Conditions for Double Cone Cases
Considered in FY14 Effort.

Parameter	Run 80	Run 39	Units
Temperature	298.8	399.6	°R
Vibrational Temperature	4,880	1,013	°R
Wall Temperature	532	531	°R
Velocity	10.06	10.17	kft/s
Mach	11.675	10.356	---
Total Enthalpy	5.277	5.212	MJ/kg
Density N ₂	2.51E-06	3.98E-06	slug/ft ³
Density O ₂	---	1.12E-06	slug/ft ³
Density NO	---	2.91E-07	slug/ft ³
Density N	3.13E-13	---	slug/ft ³
Density O	---	5.18E-09	slug/ft ³
Pressure	1.328	3.713	lbf/ft ²

The runs selected for the FY14 effort, along with most of the early experiments previously discussed, were performed in the LENS I or 48-inch shock tunnels at CUBRC. Due to the nature of the operation of these two tunnels, significant levels of nonequilibrium exist in the freestream flow. This is not representative of flight conditions and can have a significant impact on the flow over the model (Reference 8). (Additionally, as will be discussed later, STAR-CCM+ lacks the capability to model freestream flow with nonequilibrium, which reduces the value of these test cases.) The CUBRC experimentalists concluded that nonequilibrium in the freestream should be avoided (Reference 9) and therefore performed a new set of experiments in the LENS XX facility.

The LENS XX facility was specifically constructed to perform hypersonic flow experiments with little or no freestream nonequilibrium. Plans for these experiments were discussed in Reference 8, and a small selection of results was presented in Reference 9. However, the most detailed discussions of this test campaign and of experimental and numerical results are in an unpublished paper and a presentation available from the CUBRC website (References 10 and 11). Freestream conditions are provided, and pressure and heat flux measurements are presented both graphically and in tabular form. Wall temperature was assumed to be constant at 300 K. The working fluid was air, assumed to be 76.5% nitrogen and 23.5% oxygen by mass. The runtime of the experiments was only 1 ms. Mach number ranged from 10.9 to 13.2. Numerical predictions produced by multiple researchers are graphically compared to the measurements in Reference 11.

Six different runs were performed for the double cone model; all experienced separation. The size of the separation bubble increased with increasing Reynolds number. Any of these test cases should make good validation cases, but runs 1, 2, 3, and 5 should probably be given priority. Run 1 had the lowest enthalpy and should therefore be the least challenging to simulate. Total enthalpy was increased by about a factor of two for run 2, then again by another factor of two for runs 3 and 5. Runs 3 and 5 both have the same nominal total enthalpy value, but the Reynolds number differs by a factor of two. Thus, runs 3 and 5 are particularly useful for investigating Reynolds number effects. Freestream conditions for these selected runs are given in Table 2.

TABLE 2. Freestream Conditions for Double Cone Cases Considered in FY18 Effort.

Parameter	Run 1	Run 2	Run 3	Run5	Units
Temperature	315	700	938	941	°R
Wall Temperature	540	540	540	540	°R
Velocity	10.65	14.11	19.77	19.67	kft/s
Mach	12.2	10.9	13.23	13.14	---
Density Air	9.68E-07	1.91E-06	9.90E-7	2.05E-06	slug/ft ³
Pressure	0.523	2.293	1.594	3.312	lbf/ft ²
Unit Re	4.3E+04	5.8E+04	3.4E+04	7.0E+4	1/ft

2.2 SMALL CYLINDER-FLARE

Another model geometry that has been explored in parallel to the double cone model is a small, hollow cylinder-flare configuration, illustrated in Figure 3. Because of the short length of the cylinder, the flow over this model remains laminar, even when flow separation is encountered. While the small cylinder-flare was included in the early test campaigns (References 2, 3, 4, 5, and 6), attention in this work is only given to the most recent test campaign performed in the LENS XX facility. Plans for these experiments were given in Reference 8, and a few results were discussed in Reference 9, but the most detailed information for these experiments and companion simulations is found in unpublished documents available from the CUBRC website (References 10 and 11). Freestream conditions are provided, and pressure and heat flux measurements are presented both graphically and in tabular form. Wall temperature was assumed to be constant at 300 K. The working fluid was air, assumed to be 76.5% nitrogen and 23.5% oxygen by mass. Mach number ranged from 11.3 to 13.2. Simulations were also performed by a number of researchers; their predictions were graphically compared to the experimental measurements in Reference 11.

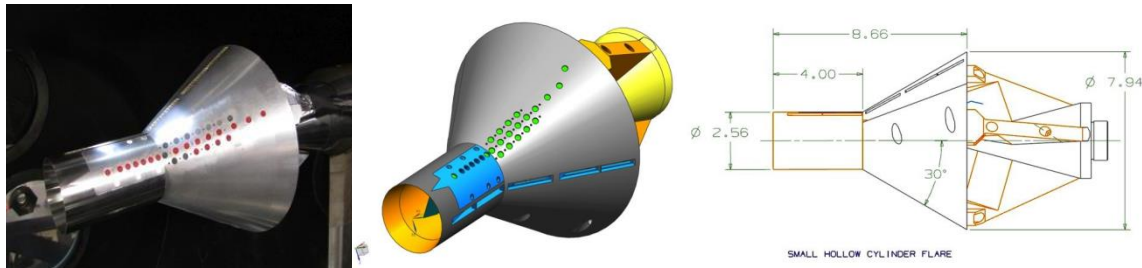


FIGURE 3. Geometry for Small, Hollow Cylinder-Flare Configuration.

Five different experimental runs were performed for the small cylinder-flare model, all of which appear to be useful validation cases. Freestream conditions are given in Table 3. The flow for run 2 remained attached, while a significant separation bubble was observed for runs 3 and 4. Runs 1 and 5 experienced a small amount of separation in the immediate vicinity of the cylinder-flare junction.

TABLE 3. Freestream Conditions for Small, Hollow Cylinder-Flare Test Cases.

Parameter	Run 1	Run 2	Run 3	Run 4	Run 5	Units
Temperature	340	572	689	1024	1112	°R
Wall Temperature	540	540	540	540	540	°R
Velocity	10.24	14.75	15.28	17.94	21.37	kft/s
Mach	11.3	12.6	11.9	11.5	13.2	---
Density Air	1.23E-06	9.68E-07	3.40E-06	4.30E-06	1.84E-06	slug/ft ³
Pressure	0.718	0.950	4.015	7.556	3.507	lbf/ft ²
Unit Re	4.6E+04	3.7E+04	1.13E+05	1.28E+05	6.1E+04	1/ft

2.3 CONE-FLARE

A model geometry that has been used to explore the interaction between shock waves and turbulent boundary layers is the cone-flare. Early tests were performed with air as the working fluid in the LENS II facility and used a model featuring a long 6-degree cone with a 42-degree flare; this geometry is illustrated in Figure 4. Data describing one test run (run 4) for this geometry are provided in Reference 12. Nondimensionalized heat flux and pressure measurements are presented in tabular form. The freestream conditions provided are tabulated here in Table 4. Note that wall temperature was not provided in the report and an assumed value was used. Pressure was computed based on temperature and density. The issue of freestream nonequilibrium for turbulent experiments conducted in the LENS II facility was not discussed in the literature; it is therefore assumed that the freestream flow is in thermal equilibrium. While the basic operation of the LENS I and LENS II facilities is the same, and though the LENS I laminar experiments are known to feature freestream nonequilibrium, it is possible that the relatively high densities in the LENS II turbulent experiments would lead to freestream equilibrium.

A later test campaign explored the interaction between shock waves and turbulent boundary layers on a slightly modified geometry with a 7-degree cone and a 40-degree flare; this geometry is illustrated in Figure 5. Plans for these experiments were discussed in Reference 12, and limited results were presented in Reference 9, but the most detailed discussions of this test campaign and the experimental results are in an unpublished paper and a presentation available from the CUBRC website (References 13 and 14). Freestream conditions are provided, as are pressure and heat flux measurements

(presented both graphically and in tabular form). Accuracy is reported as $\pm 5\%$ for the pressure measurements and $\pm 3\%$ for the heat flux. The working fluid was air, assumed to be 76.5% nitrogen and 23.5% oxygen by mass. Transition from laminar to turbulent flow occurs far forward on the cone, well away from the shock interaction region.

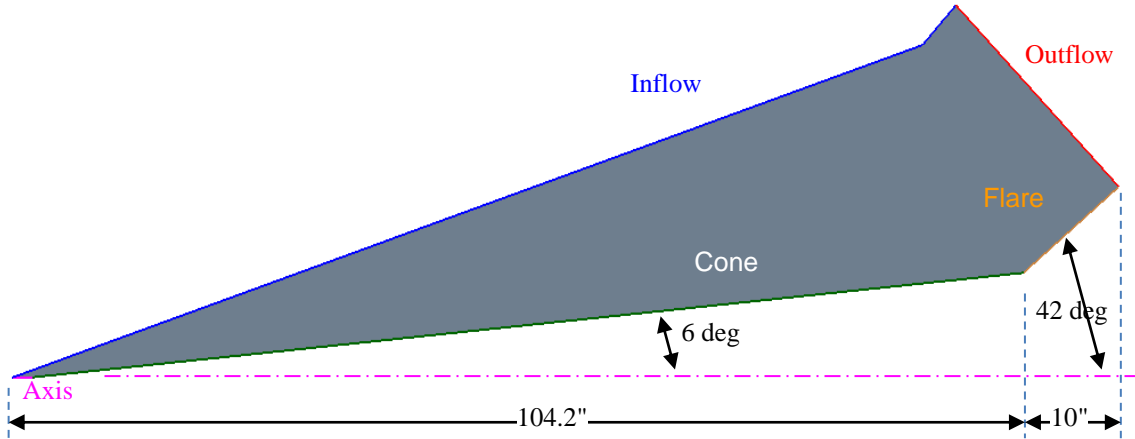


FIGURE 4. Geometry for 6-/42-Degree Cone-Flare Configuration.

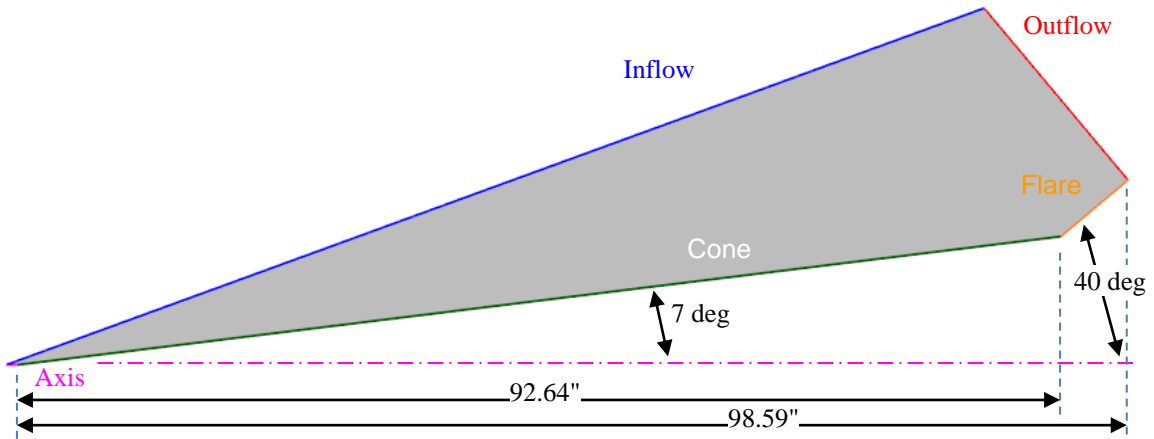


FIGURE 5. Geometry for 7-/40-Degree Cone-Flare Configuration.

TABLE 4. Freestream Conditions for 6-/42- and 7-/40-Degree Cone-Flare Cases.

Parameter	Run 4	Run 33	Run 45	Units
Geometry	6/42 deg	7/40 deg	7/40 deg	---
Temperature	121	102	440	°R
Wall Temperature	532	532	532	°R
Velocity	5.92	3.055	6.077	kft/s
Mach	11.0	6.17	5.9	---
Density Air	6.345E-05	1.43E-04	2.16E-04	slug/ft ³
Pressure	13.175	25.030	163.089	lbf/ft ²

Experiments were performed for flows with nominal Mach numbers of 5, 6, 7, and 8. At each Mach number one experimental run was performed for a “cold” flow and one for a “hot” flow (where flight representative velocities and enthalpies were achieved). Additional, intermediate “warm” flow experiments were performed at Mach 6 and 8. It was observed that for Mach 5 the hot flow experiment produced a much smaller separation region than was observed for the cold flow run. At the higher Mach numbers the hot flow experiments all produce attached flow, although insipient separation is reported for Mach 6 and 8. It was also observed that the size of the separation region decreased as the Mach number was increased.

An additional unpublished presentation includes comparisons with multiple simulations from different analysts (Reference 15). Multiple simulations used the Menter shear stress transport (SST) turbulence model, while one simulation for each run used the Spalart-Allmaras model. In general, the simulations using the Spalart-Allmaras model were more accurate in predicting the occurrence of flow separation and the size of the resulting pressure bubble. The resulting pressure distributions generally agreed well with the experimental measurements, but the heat flux predictions did not agree very well. For most, but not all, cases the Spalart-Allmaras turbulence model significantly under-predicted heat flux on the flare. The simulations with the Menter SST model all over-predicted flow separation. For a given run, simulations by different analysts would often predict different points of flow separation. However, these simulations generally predicted heat flux and pressure on the flare reasonably well. It was reported that the predictions were not strongly affected by how (or if) the transition process was numerically modeled.

The Mach 6 hot flow (run 45) and cold flow (run 33) experiments are selected as additional test cases to be explored in the FY18 effort. Freestream conditions for these runs are tabulated here in Table 4. Wall temperature is assumed to be constant at 532°R. (Values of the T_w/T_0 ratio were also provided by CUBRC, but computing wall temperature from this ratio leads to elevated wall temperature values that are known to be incorrect.)

2.4 LARGE CYLINDER-FLARE

A “large” variant of the hollow cylinder-flare test case featuring turbulent boundary layers was also considered in parallel to the cone-flare test case in the most recent test campaign. This test model consisted of a long (to result in a turbulent boundary layer), hollow cylinder terminating in a 36-degree flare, as illustrated in Figure 6. As was the case for the cone-flare test case, plans for the test campaign were presented in Reference 12, limited results were given in Reference 9, but the most detailed and comprehensive discussion of these tests comes from unpublished documents available from the CUBRC website (References 13 and 14). Freestream conditions are tabulated, and the experimental heat flux and pressure measurements are both tabulated and presented graphically. Measurement accuracy was reported to be $\pm 5\%$ for pressure and $\pm 3\%$ for heat flux. The working fluid was air, assumed to be 76.5% nitrogen and 23.5% oxygen by mass. Transition from laminar to turbulent flow occurs far forward on the cylinder, well away from the shock interaction region.

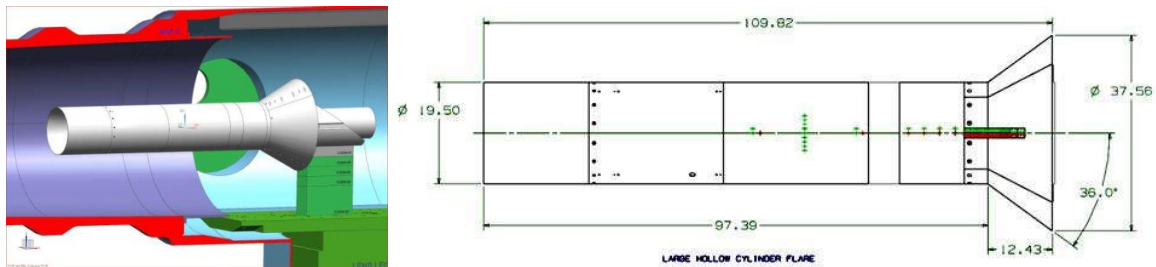


FIGURE 6. Geometry for Large, Hollow Cylinder-Flare Configuration.

Though it appears that a significant number of tests were performed for the large cylinder-flare model, the separation bubble produced for all the “cold” flow runs was so large that it exceeded the extent of the instrumentation. This rendered it impossible to accurately determine the true extent of separated flow. As a result, only the six “hot” flow runs (where flight representative velocities and enthalpies were achieved) were presented in detail by the experimentalists as potential validation cases. Nominal freestream Mach number ranged from 5 to 8. For Mach 5 and 6, experiments were performed at “low” and “high” Reynolds numbers, while experiments were performed only at “low” Reynolds numbers for Mach 7 and 8. It was observed that the size of the separation bubble did not change significantly with these changes to the unit Reynolds number, indicating that the effects of Reynolds number on separation are small. It was observed that the size of the separation bubble decreased with increasing Mach number.

Comparisons between experimental results and simulations performed by multiple analysts were also made graphically in an unpublished presentation (Reference 15). Most simulations used the Menter SST turbulence model, while one analyst considered the Spalart-Allmaras model. All simulations presented significantly over-predicted the length of the separation bubble. However, even though the predicted separation point was well

forward of the observed location, relatively good agreement with experiment was obtained for the pressure profiles predicted for the Mach 6 and 7 runs. The Menter SST turbulence model tended to over-predict heat flux on the flare, while the Spalart-Allmaras model usually produced under-predictions. Different analysts would often predict different flow separation points for any given run, though the scatter in the results was smaller than that for the cone-flare test case. Specifying the location of boundary layer transition (from laminar to turbulent flow) did not change the predictions.

The Mach 7 case (run 18) is selected as the primary large cylinder-flare test case for consideration in the FY18 effort, with the two Mach 6 cases (runs 11 and 13) selected as secondary test cases. Freestream conditions for these selected runs are presented here in Table 5. Wall temperature is assumed to be constant at 532°R, as was done for the cone-flare test case.

TABLE 5. Freestream Conditions for Large, Hollow Cylinder-Flare Test Cases.

Parameter	Run 11	Run 13	Run 18	Units
Temperature	364	347	404	°R
Wall Temperature	532	532	532	°R
Velocity	5.578	5.496	6.869	kft/s
Mach	5.95	6.01	6.96	---
Density Air	1.02E-04	3.06E-04	8.90E-05	slug/ft ³
Pressure	63.712	182.208	61.700	lbf/ft ²
Unit Re	1.73E+07	5.33E+07	1.70E+07	1/ft

2.5 SHOCK/SHOCK INTERACTION

Another interesting hypersonic flow problem is that arising from the interaction of multiple shocks. This can occur, for example, near the cowl lip for air-breathing propulsion systems, where the oblique shock system from the compression ramp interacts with the bow shock produced ahead of a blunted cowl lip. Other opportunities for such shock/shock interactions include (but are certainly not limited to) body shocks impinging on fins or the interaction between body shocks produced by staged vehicles. These shock/shock interactions can result in the direct impingement of a transmitted shock or a supersonic jet flow feature onto the cowl lip or fin. Such direct impingement leads to substantially higher heating than would be experienced in the stagnation region behind a bow shock in the absence of shock/shock interaction (Reference 16).

These shock/shock interactions were the subject of an extensive test campaign performed in the 48- and 96-inch shock tunnels at CUBRC (Reference 16). Most experiments considered the interaction of a single, planar oblique shock (produced by a plate inclined into the flow) with the bow shock produced by a 3-inch-diameter cylinder. A schematic of the test geometry is given in Figure 7. A large variety of shock/shock

interactions were explored by adjusting the length and inclination angle of the plate, as well as the position of the cylinder. Nominal freestream Mach numbers ranged from 6 to 19. The shear layers produced by the shock/shock interactions were completely turbulent for experiments conducted at Mach 6 and 8. Fully laminar shear layers were obtained for Mach 11 and above, though it should be noted that some runs for Mach 11 and 16 had transitional shear layers. (For Mach 11, runs 103, 104, and 113 appear to be laminar, while runs 34, 35, 36, and 37 were transitional or turbulent. At Mach 16, runs 106, 107, 114, and 115 were laminar, while run 43 was turbulent.) A few experiments conducted at Mach 8 considered the interaction of two oblique shocks with the bow shock or the interaction of single shock with the bow shock produced by a swept cylinder.

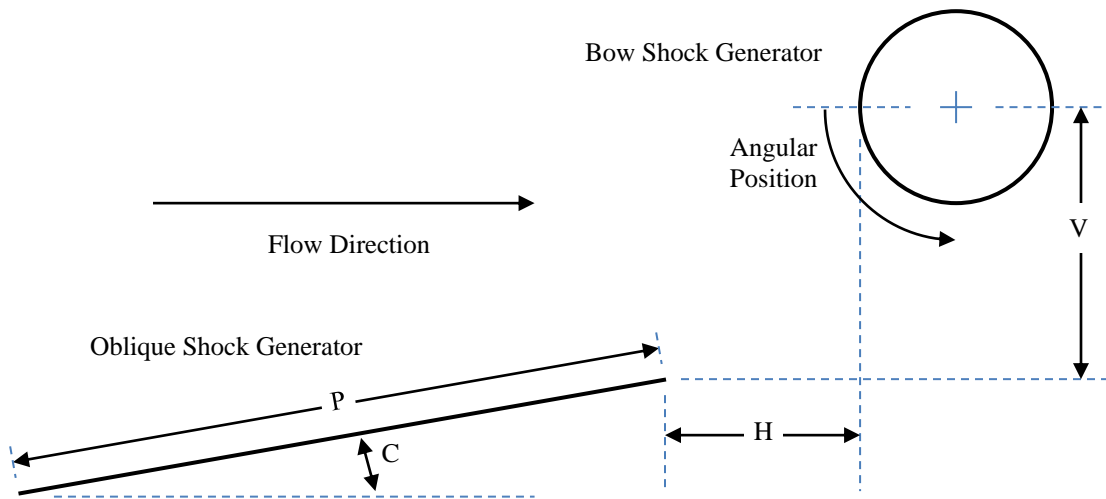


FIGURE 7. Schematic of Shock/Shock Interaction Test Case Geometry.

A large number of experimental runs were conducted, and the data presented are quite extensive. Geometry parameters and the freestream conditions are given for all cases, as well as the pressure, temperature, and heat flux measured at a number of points on the cylinder. These measurements are reported as a function of angular position, measured anti-clockwise from the leading edge of the cylinder (see Figure 7). Conveniently, these data are presented in both graphical and tabular form. The reported experimental uncertainty is $\pm 5\%$ for heat flux measurements and $\pm 3\%$ for pressure measurements. Cyclical variations due to flow unsteadiness are reported to be as large as $\pm 15\%$. Schlieren images are also presented, though image quality is often quite poor.

The first run considered as a test case in this work is run 103, selected primarily because it was reported to have a laminar shear layer, and there was some desire to avoid any uncertainty associated with the choice of turbulence model. However, as is discussed later in Section 0, the predicted flowfield is not consistent with the measurements. The second experimental run selected for simulation is run 59. This choice proved to be unlucky. After it was noted that, once again, the simulations did not match the

experimental measurements, it was observed that the geometric parameters listed for this run clearly do not match the Schlieren imagery in the test report. Since the geometric parameters are obviously in error for this run, this raises the possibility that the parameters listed for other runs (such as run 103) could also be in error. It is also noted that Reference 7 mentions a 1996 revision of the original National Aeronautics and Space Administration (NASA) test report. Presumably, this revised version includes corrections for these errors and others, but, unfortunately, it has not yet been possible to locate and obtain the revised document. The final run selected for simulation in this work is run 60. Simulations agree reasonably well with experiment for this run. The geometric parameters and freestream conditions for all three runs considered (runs 103, 59, and 60) are listed in TABLE 6 for completeness, though it is recommended that any future efforts not investigate runs 103 or 59, due to known or suspected errors in the reported values.

TABLE 6. Geometry and Freestream Conditions for Shock/Shock Interaction Cases.

Parameter	Run 103	Run 59	Run 60	Units
V	4.15	2.83	3.19	in
H	-1.40	2.76	1.81	in
C	10.0	12.5	12.5	degrees
P	46.25	26.5	26.5	in
Temperature	114.3	222	218.9	°R
Wall Temperature	529.97	529.97	529.97	°R
Velocity	6.099	5.872	5.832	kft/s
Mach	11.63	8.036	8.039	---
Density Air	3.219E-06	4.478E-05	4.493E-05	slug/ft ³
Pressure	0.629	17.064	16.877	lbf/ft ²

3.0 METHODOLOGY

All simulations performed as part of this work used the STAR-CCM+ software package. Those simulations completed in the FY14 effort employ version 9.04, while the FY18 effort makes use of version 12.06. STAR-CCM+, a product of the Siemens Company, is a highly integrated, all-in-one CFD package offering extremely sophisticated and robust automatic meshing capabilities, a complete set of advanced physics models, and powerful, parallelized post-processing tools.

The general approach taken for this effort is to begin with simple simulations that neglect high-temperature phenomena and then systematically add in models for high-temperature and nonequilibrium processes. Since the test cases investigated featured axisymmetric or planar two-dimensional geometries, only axisymmetric or two-dimensional simulations are performed. Three-dimensional simulations of these problems have not been attempted but in some cases, should potentially be investigated as part of future work.

3.1 AIR PROPERTY MODELS

The default air model in STAR-CCM+ employs constant values for the material properties (e.g., specific heat, viscosity, and thermal conductivity). While constant properties are appropriate for flows near room temperature, this assumption will lead to serious errors for the high-temperature flows typically associated with hypersonic flight. It is possible to capture the temperature-dependent properties in STAR-CCM+ using alternative property models. However, the default coefficients used in these temperature-dependent property models have been found to occasionally contain errors. It is recommended that material properties always be verified against accepted values.

Simulations performed as part of the FY18 effort make use of one of three different property models for air discussed later. The single species model captures the temperature dependence of the gas properties, while the two species model adds the ability to capture thermodynamic nonequilibrium, and the five species model includes dissociation reactions.

The gas property models used in the earlier FY14 effort are similar to the air models discussed here but are in general not as standardized and may have some significant differences. The details of the gas models used for the different FY14 simulations are presented in the relevant results sections. One notable air model used in some of the FY14 simulations is the equilibrium air model built into STAR-CCM+, which is also discussed later.

It is recommended that all future STAR-CCM+ simulations make use of one of these “standardized” air models, as appropriate.

3.1.1 One Species Air Model

For the single species air model, viscosity and thermal conductivity are both computed using a Sutherland's Law model. The default coefficients provided by STAR-CCM+ appear to be correct and are used without modification. Specific heat is modeled using a custom polynomial in temperature:

$$c_p = a_0 + a_1T + a_2T^2 + a_3T^3 + a_4T^4 + a_5T^5 \quad (1)$$

Five polynomial intervals are used to model the specific heat for temperatures ranging from 0 to 6,000 K. (The default specific heat polynomial included in STAR-CCM+ consists of a single interval for temperatures ranging from 200 to 1,000 K.) The coefficients and temperature limits for each interval are given in Table 7; temperature must be in units of K and specific heat is given in units of J/kg-K. These coefficients are obtained by performing new curve fits to the thermodynamic data provided in Reference 17.

TABLE 7. Specific Heat Polynomial Coefficients for Air.

T_{\min}	T_{\max}	a_0	a_1	a_2	a_3	a_4	a_5
0	200	1.003E+03	---	---	---	---	---
200	1,000	1.000E+03	9.486E-02	-8.455E-04	2.633E-06	-2.608E-09	8.668E-13
1,000	2,000	8.060E+02	5.181E-01	-2.177E-04	3.489E-08	---	---
2,000	4,000	1.040E+03	1.631E-01	-3.472E-05	2.880E-09	---	---
4,000	6,000	1.097E+03	1.093E-01	-1.816E-05	1.210E-09	---	---

3.1.2 Two Species Air Model

In the two species air model, air is modeled as being a mixture of molecular nitrogen and oxygen. This air model also makes use of the thermal nonequilibrium model in STAR-CCM+. Specific heats for the translational-rotational and vibrational-electronic modes are computed as a mass-weighted mixture of the two component species. Mixture viscosity and thermal conductivity for the two modes are computed based on Mathur-Saxena averaging. Diffusivity is computed based on Schmidt number. A constant value of 0.85 is specified for the Schmidt number based on chemical equilibrium calculations performed for air using the Chemics program (Reference 18). Vibrational mode relaxation time for the mixture is computed based on inverse mole-fraction averaging.

For each species, viscosity is computed using the Chapman-Enskog theory. Species thermal conductivities (for both energy modes) are computed using nonequilibrium kinetic theory. The default values for the parameters needed to compute the transport properties (e.g., dipole momentum, Lennard-Jones characteristic length, Lennard-Jones energy, rotational relaxation collision number) are compared to the CHEMKIN database (Reference 19) and appear to be correct.

Species specific heat for the translational-rotation mode is computed based upon a fully excited assumption. Specific heat for the vibrational-electronic mode is computed based on gas kinetics. Default values for the partition functions (characteristic temperatures and degeneracies) for the vibrational and electronic modes for the species appear to be reasonable. However, these values are updated with those taken from traceable sources in the literature (References 20 and 21). Mode relaxation time for each species is computed based on the Millikan, White, and Park correlation.

3.1.3 Five Species Air Model

In the five species model, air is modeled as being a mixture of: N₂, O₂, NO, N, and O. Mixture and species properties are computed using the same methods used in the two species air model. Default transport property parameters for the additional species are compared to the CHEMKIN database and are found to be correct. The vibrational and electronic mode partition functions are updated to use values from the literature.

This air model uses the “complex chemistry” solver in STAR-CCM+ to compute dissociation reactions as described by a truncated form of the Dunn/Kang mechanism. (The complete Dunn/Kang mechanism includes ionization reactions, which are excluded in this work. STAR-CCM+ appears to have some limited capabilities for modeling certain types of plasmas but does not appear to have a capability for modeling ionization reactions.) The clustering chemistry acceleration option, which is activated by default, is deactivated for all simulations presented in this work. Forward reaction rate coefficients are computed for each reaction based on a modified Arrhenius equation:

$$k = AT^b \exp\left(-\frac{T_a}{T}\right) \quad (2)$$

The reactions included in the Dunn/Kang mechanism are detailed in Table 8 and are taken from References 1 and 22. All reactions are reversible, with the reverse reaction rate computed from the equilibrium coefficient (which is a function of reaction thermodynamics). A STAR-CCM+ macro (essentially a special script written in Java) is created in this effort that can be used to automatically setup these reactions in new simulations. A Matlab script is also created that formats the reaction parameters required by the macro. These two tools can be used together to set up any alternative reaction mechanisms investigated as part of future efforts.

TABLE 8. Forward Reaction Rates for Dunn/Kang Mechanism.

Index	Reaction	A, cm ³ /mol-s	b	T _a , K
1	O ₂ + N = 2O + N	3.600E+18	-1	5.95E+04
2	O ₂ + NO = 2O + NO	3.600E+18	-1	5.95E+04
3	N ₂ + O = 2N + O	1.900E+17	-0.5	1.13E+05
4	N ₂ + NO = 2N + NO	1.900E+17	-0.5	1.13E+05
5	N ₂ + O ₂ = 2N + O ₂	1.900E+17	-0.5	1.13E+05
6	NO + O ₂ = N + O + O ₂	3.900E+20	-1.5	7.55E+04
7	NO + N ₂ = N + O + N ₂	3.900E+20	-1.5	7.55E+04
8	O + NO = N + O ₂	3.200E+09	1	1.97E+04
9	O + N ₂ = N + NO	7.000E+13	0	3.80E+04
10	N + N ₂ = 2N + N	4.085E+22	-1.5	1.13E+05
11	O ₂ + O = 2O + O	9.000E+19	-1	5.95E+04
12	O ₂ + O ₂ = 2O + O ₂	3.240E+19	-1	5.95E+04
13	O ₂ + N ₂ = 2O + N ₂	7.200E+18	-1	5.95E+04
14	N ₂ + N ₂ = 2N + N ₂	4.700E+17	-0.5	1.13E+05
15	NO + O = N + 2O	7.800E+20	-1.5	7.55E+04
16	NO + N = O + 2N	7.800E+20	-1.5	7.55E+04
17	NO + NO = N + O + NO	7.800E+20	-1.5	7.55E+04

3.1.4 Equilibrium Air Model

The equilibrium air model is a “real gas” model that is built into the STAR-CCM+ software package. When this gas model is selected, the gas material properties (viscosity, thermal conductivity, specific heat, and speed of sound) are automatically computed as functions of temperature and pressure. This model takes into account the effects of dissociation, ionization, and internal energy excitation (i.e., excitation of the vibrational and electronic energy modes). However, the key assumption associated with this model is that of thermochemical equilibrium, i.e., that the timescales required to complete these physical processes are very fast relative to the flow timescale. The curve fits used in this equilibrium air model are reported to be valid for temperatures up to 30,000 K and for pressures between 0.0001 and 100 atmospheres.

3.2 SOLVER SETTINGS

All simulations performed in this effort make use of the “coupled” solver in STAR-CCM+, which solves the mass, momentum, and energy equations simultaneously as a coupled system of equations. (The alternative, “segregated solver” solves the momentum and energy equations sequentially and is therefore unsuitable for modeling

compressible flow.) The default solver settings incorporated into STAR-CCM+ usually must be adjusted to meet the needs of any particular problem to be solved. This is particularly true for simulations of hypersonic flows, where the use of the default solver values most often will result in failure of the simulation.

One setting that has a particularly large impact on the success of the simulations is the method used to compute the inviscid fluxes. For all simulations presented in this work (both FY14 and FY18), the inviscid flux method is changed from the default Roe flux-difference splitting scheme (which is suitable for lower speed flows) to the AUSM+ flux-vector splitting scheme (which is better suited for high-speed flows). It is strongly recommended that the AUSM+ method be used for any STAR-CCM+ simulations of supersonic or hypersonic flows.

A few additional solver settings are explored as part of the FY14 effort. (These settings are discussed here for completeness, but significant improvements are made as part of the FY18 effort. It is strongly recommended that future simulations make use of the solver settings identified in the FY18 effort, to be discussed shortly.) For the FY14 simulations, the Courant-Friedrichs-Lewy (CFL) number is generally set to 1.0. A larger value for the CFL number causes the solution to converge faster but can also destabilize the solution and lead to failures. Conversely, lower values of the CFL number stabilize the solution but require more iterations in order to reach convergence. Occasionally a simulation will fail to solve even with a CFL number of 1.0 or less. In these cases, the cause for the failure is almost always found to be associated with some aspect of the problem setup (usually a mesh quality issue but also potentially some other solver setting or a specified boundary condition). It is therefore recommended that CFL numbers much below 1.0 not be used for future simulations, as these low CFL numbers usually indicate issues elsewhere in the problem setup that cannot be overcome with a low CFL number. The explicit relaxation factor is also changed from its default value of 1.0 to a value of 0.75 for many simulations performed in FY14. A lower value reduces the magnitude of the updates made to each variable for each iteration and therefore stabilizes the solution. Finally, it is observed that when the “expert driver” feature (discussed more shortly) is activated it overrides the user-specified values for some settings (i.e., CFL number, positivity rate limit, and explicit relaxation factor). Since in the FY14 effort this behavior is generally not desired, the “expert driver” feature is usually left deactivated (but this is no longer recommended).

In the FY18 effort, it has been possible to identify a much improved set of solver settings that is found to work exceptionally well for all the test cases explored. Identification of these solver settings is made possible by some recent improvements to the STAR-CCM+ software, the experience gained as part of the FY14 effort, and by improvements to the documentation for STAR-CCM+. The recommended notable (i.e., non-default) solver settings are listed below, with a more detailed discussion following.

- Discretization: MUSCL third-order/central-differencing scheme
- Coupled inviscid flux: AUSM+ flux-vector splitting

- CFL number: 10
- Algebraic multigrid linear solver:
 - Cycle type: F cycle
 - Pre-sweeps: 0
 - Post-sweeps: 3
 - Max levels: 2
- Grid sequencing initialization: activated
 - CFL number: 2.5
- Expert driver: activated
 - CFL ramp end iteration: 500
 - CFL limiting target algebraic multigrid cycles: 8
- Continuity convergence accelerator: activated
 - Enhance stability treatment: activated
 - Algebraic multigrid linear solver: as above

The MUSCL third-order scheme is a relatively new feature to STAR-CCM+. It provides third-order spatial accuracy, except in the vicinity of strong shocks, where, due to limiting, the spatial accuracy is reduced to second-order. The third-order MUSCL scheme provides improved (i.e., reduced) dissipation compared to the second-order discretization scheme (which is the default) yet remains robust.

The algebraic multigrid linear solver is the set of algorithms used to solve the linear equations produced by discretization of the problem. The algebraic multigrid technique is used to combine the equations for each cell in the domain to algebraically create equations describing a sequence of coarser meshes. By solving the equations on these different mesh levels, it is possible to more quickly converge to a final solution than by solving exclusively on the finest mesh. The settings listed here are recommended by the latest STAR-CCM+ documentation for use with hypersonic flow problems.

The “expert driver” feature in STAR-CCM+ automatically adjusts the CFL number and some other solver settings (such as the positivity rate limit factor and the explicit relaxation factor) in order to maximize the convergence rate of the simulation, while (usually) maintaining a stable simulation. Since the expert driver feature automatically reduces the CFL number during difficult portions of the simulation, then increases it once again when possible, it is possible to stably run a simulation at much higher CFL numbers than if a constant CFL is specified. As a result, the solutions can be converged much more quickly.

When these settings are specified as recommended, the result is that a CFL number of 2.5 is used for the grid sequencing initialization (discussed in more detail in Section 3.4). Then, during the main solution of the simulation, the CFL number is ramped up from an initial value of 0.25 to a final value of 10 over the course of 500 iterations. The CFL number is occasionally, temporarily reduced when necessary, as determined by the expert driver feature. All simulations performed in the FY18 effort run successfully with a maximum CFL number of 10. It seems likely that even higher values for the CFL

number could be utilized in conjunction with the expert driver feature. This has not been explored in this effort but is probably worthy of consideration in the future.

The continuity convergence accelerator (CCA) is a feature in STAR-CCM+ that solves a pressure-correction equation in order to accelerate the convergence of the continuity equation. This feature has no impact on the final solution, but simply provides a way for that final solution to be obtained more quickly under most circumstances. It is found in this work that the enhanced stability treatment option for this feature should be activated. Without this option activated it is found that the continuity convergence accelerator can cause poor residual convergence, or even destabilize the solution. The algebraic multigrid linear solver settings for the continuity convergence accelerator are set to be the same as those used for the main solver.

When performing simulations using the Menter SST turbulence model, the following non-default options are found to be recommended for hypersonic flows:

- Quadratic constitutive relation: activated
- Compressibility correction: deactivated
- a_1 coefficient: 0.355

Additional discussion of these turbulence model options is discussed later in Section 0. It should also be noted that the settings for the algebraic multigrid linear solver for the turbulence models are not changed from their default values.

The solver settings just described are found to work exceptionally well for all the test cases explored in the FY18 effort and are strongly recommended for use for all future hypersonic simulations performed with STAR-CCM+.

3.3 BOUNDARY CONDITIONS

The wetted surfaces of the models are modeled using a wall boundary condition. These non-slip walls are assumed to be aerodynamically smooth (no roughness effects are modeled). Walls have a constant, uniform temperature condition applied, though it is also possible to specify heat flux or impose an adiabatic condition. For simulations involving multiple species, the wall species option is set to “impermeable” (resulting in a noncatalytic wall with zero mass fraction gradients in the wall-normal direction). It is, however, also possible to specify the species mass (or mole) fractions or the species mass fluxes on the wall boundaries.

Inflow and far field boundaries are found to be best modeled using the freestream boundary condition option. It is necessary to specify Mach number, flow direction, and the static pressure and temperature for the freestream boundary. For simulations modeling thermodynamic nonequilibrium, the same temperature is used for both the translation-rotational and the vibrational-electronic energy modes. It is not possible to

specify freestream thermodynamic nonequilibrium with STAR-CCM+. This is perfectly appropriate for flight conditions but is not the case for several of the experimental test cases, where, due to the nature of the test facility, the resultant freestream is not in thermodynamic equilibrium. For simulations involving multiple species, the species mass (or mole) fractions in the freestream need to be specified. For the simulations using the reacting five species air model, the freestream mass fractions of the minor species (NO, N, and O) are set to a very small value (1.0E-10). Setting the mass fractions to be exactly zero can cause numerical issues when computing the reaction rates.

The freestream boundary condition can also be used for the outflow boundary, especially if the model geometry does not intersect the outflow boundary. However, for all of the test cases investigated in this work, the model geometry does, in fact, intersect the outflow boundary. A freestream boundary can be used in this situation, but it is found that this can sometimes lead to nonphysical flow features and other numerical issues. A better option under these situations is to use a pressure outlet boundary condition. It is necessary to specify the static pressure and temperature and (for multispecies simulations) the species mass (or mole) fractions on this boundary. The values should be set to the freestream conditions.

3.4 INITIAL CONDITIONS

This simplest way to initialize a simulation is to specify that freestream conditions exist everywhere within the domain at the start of the simulation. This produces an “impulsive start” initialization of the simulation, which can pose some numerical challenges (especially for higher velocity flows) that can lead to simulation failure. While it is found that several of the FY14 simulations can only be successfully initialized by using this impulsive start technique (e.g., some double cone simulations and all cone-flare simulations), many simulations cannot be successfully initialized in this manner.

A gentler approach to initializing the solution is to first impulsively start the simulation to a low-speed (or even zero velocity) condition, then ramp up the freestream Mach number over several hundred iterations to the final, desired value. This initialization approach is found to be necessary for some FY14 simulations (e.g., some double cone simulations) but leads to massive flow separation and simulation failure in others (e.g., the cone-flare simulations).

The most sophisticated way of initializing a simulation is to use the grid sequencing initialization feature included in STAR-CCM+. In this approach, STAR-CCM+ creates a sequence of coarse meshes, starting with a very coarse mesh with only a few cells in it and increasing in refinement until the final mesh is obtained. The inviscid flow solution is computed, starting with the coarsest mesh. Once a certain level of convergence is obtained (usually in under 50 iterations for each mesh), the results are interpolated onto the next mesh, and the process is completed until an inviscid solution is obtained on the finest mesh. Thus, the resulting initialization will include many of the important flow

features (i.e., shocks). Since this inviscid solution is obtained through a sequence of coarse meshes, it is possible to obtain this initial condition relatively quickly. This grid sequencing approach only works for some of the double cone simulations attempted in the FY14 effort but with the recommended solver settings previously listed, it is found to work for all simulations attempted in FY18.

The grid sequencing initialization option is therefore the recommended initialization technique for all future hypersonic STAR-CCM+ simulations. Should this approach not be successful, the ramping or impulsive start initialization options can also be considered. Failure of all three initialization options usually indicates an error elsewhere in the problem setup. The problem setup and mesh should be carefully reviewed before attempting more exotic initialization techniques.

3.5 MESH

The simulations performed in the FY14 effort make use of structured directed meshes. One mesh is created for the double cone test case, another for the cone-flare test case. These same meshes are used for all runs simulated for the respective test cases. There are weaknesses associated with this approach, so the FY18 work relies upon unstructured meshes, which are tailored to meet the needs of each test case run. These unstructured meshes are optimized through refinement based upon the flow solution. Two different methods for performing this refinement are developed. Details of these meshing strategies are detailed in the following sections.

3.5.1 Structured Directed Mesh

Early simulations performed during the FY14 effort explored the various unstructured mesh generators included in STAR-CCM+. Unfortunately, at that time there was difficulty in obtaining a mesh with the desired quality, but it was undesirable for the effort to get bogged down exploring different mesh options. In order to permit quicker exploration of the hypersonic physics models, unstructured meshes were abandoned, and the switch was made to a structured “directed mesh.” These directed meshes are constructed using the “directed mesh” generator included with STAR-CCM+, which lacks some sophisticated features available in traditional structured mesh generators (e.g., Pointwise). However, it is relatively easy to obtain a mesh that is mostly aligned with the expected shock structure. (It is desirable for mesh to be aligned with strong shocks in the flowfield whenever possible in order to be able to better capture the shock discontinuities.) Another benefit of these directed meshes is that finer or coarser meshes can easily be constructed by changing the edge cell count and cell sizes by a factor of two. Structured meshes are well suited for the simple, axisymmetric geometries of the test cases considered in this effort but are not suitable for complicated, three-dimensional shapes due to the very time-consuming, manual nature of the mesh generation process.

An example of the structured mesh used for the FY14 simulations of the double cone test case is illustrated in Figure 8. This mesh features 376 cells in the wall-tangent direction (160 on the first cone, 168 on the second cone, and 48 on the cylinder) and 120 cells in the wall-normal direction, for a total of 45,120 cells. Cells adjacent to the walls have a thickness of 5E-4 inches; maximum cell aspect ratio is 100. Biasing is used to cluster cells near the wall and near the corners of the geometry.

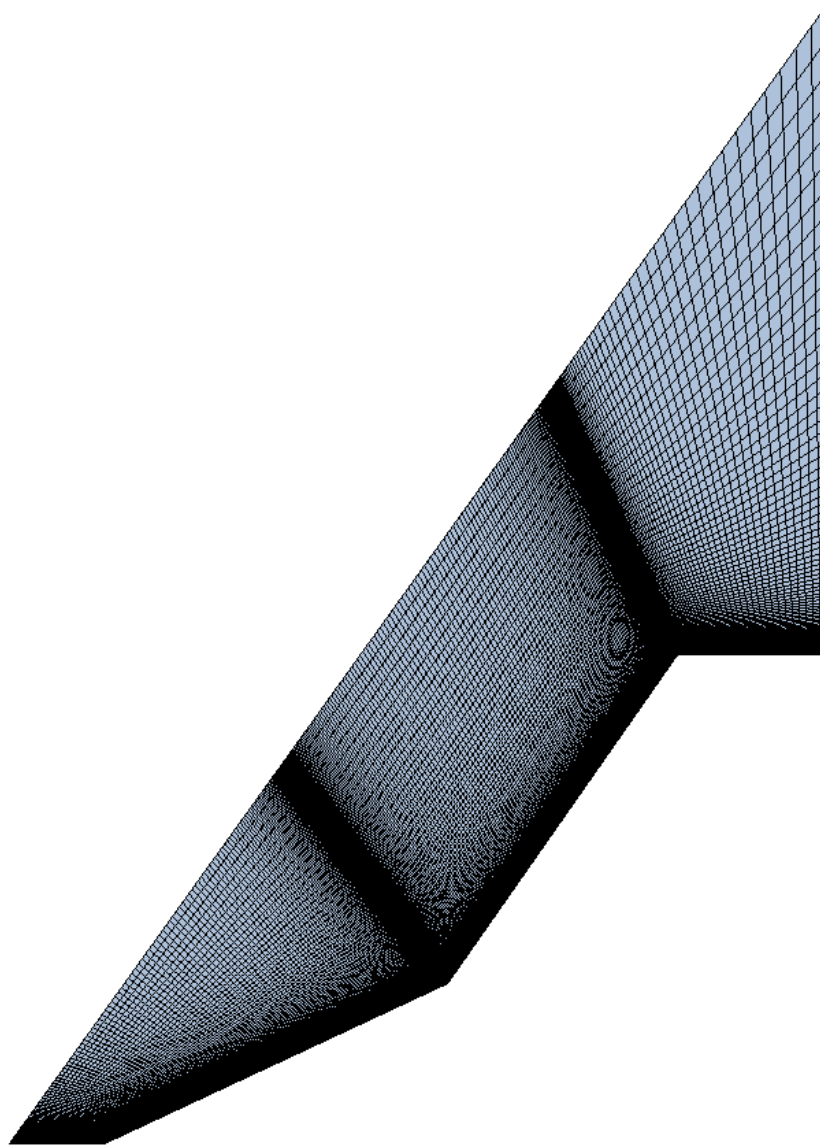


FIGURE 8. Illustration of Structured Directed Mesh Used for FY14 Simulations of Double Cone Test Case.

3.5.2 Pressure Gradient Mesh Refinement

Since structured directed meshes are labor intensive and not suitable for three-dimensional problems, one goal of the FY18 effort is to investigate the automated construction of unstructured meshes. A number of significant improvements to the mesh generation tools in STAR-CCM+ have been implemented since the conclusion of the FY14 effort, which have made it possible to obtain good quality unstructured meshes much more easily than previously. A secondary goal is to investigate techniques whereby the mesh can be refined based upon the flow solution. In theory, this should allow cells to be concentrated at important locations in the domain (such as near shocks), while having fewer cells in regions of uniform flow where coarser meshes are suitable.

The traditional approach for generating a mesh in STAR-CCM+ allows the user to locally refine the mesh in certain regions defined by simple geometric shapes (such as bricks, cylinders, or spheres). By specifying these refinement zones, it is possible to obtain a more refined mesh in some parts of the domain than others. However, this is a manual process, the user must have a good estimate of where important flow features will occur, and extra mesh refinement is often produced in regions where it is not needed (due to the limitations of available geometric shapes). However, one relative new feature in STAR-CCM+ is the use of a mesh refinement table to control cell size throughout the domain. This refinement table approach allows the mesh to be arbitrarily refined; it is simply necessary for the user to construct a table of points within the domain, along with the desired cell size at those points.

While STAR-CCM+ provides this refinement table capability, it is up to the user to determine how to compute appropriate cell size values for each point within the domain. By computing the desired cell size based upon the solution obtained with a given mesh, it is possible to refine or coarsen the mesh based upon the initial solution. One goal of this effort is to establish a suitable method for computing cell sizes from a solution such that flow features important for high speed flows (such as shocks) are refined, while the mesh is coarsened in regions of uniform flow.

Since shocks are the main flow feature to be resolved in these hypersonic flows, an initial technique is pursued that refines the mesh based upon the pressure gradients in the flow. (This refinement approach may not be suitable for other types of flows containing important flow features independent of pressure gradients.) In this approach, an initial solution is obtained using a fairly coarse and uniform initial mesh. This mesh is then refined, the solution from the old mesh is interpolated onto the new mesh as an initial condition, and the solution is run to convergence on the new mesh. This refinement process can be repeated several times, until an acceptable level of mesh refinement is obtained. Figure 9 shows the initial mesh and four subsequent refinements made using this initial pressure gradient technique for the shock/shock interaction test case. This pressure gradient technique was initially developed for the shock/shock interaction test case and is also used for the double cone test cases.

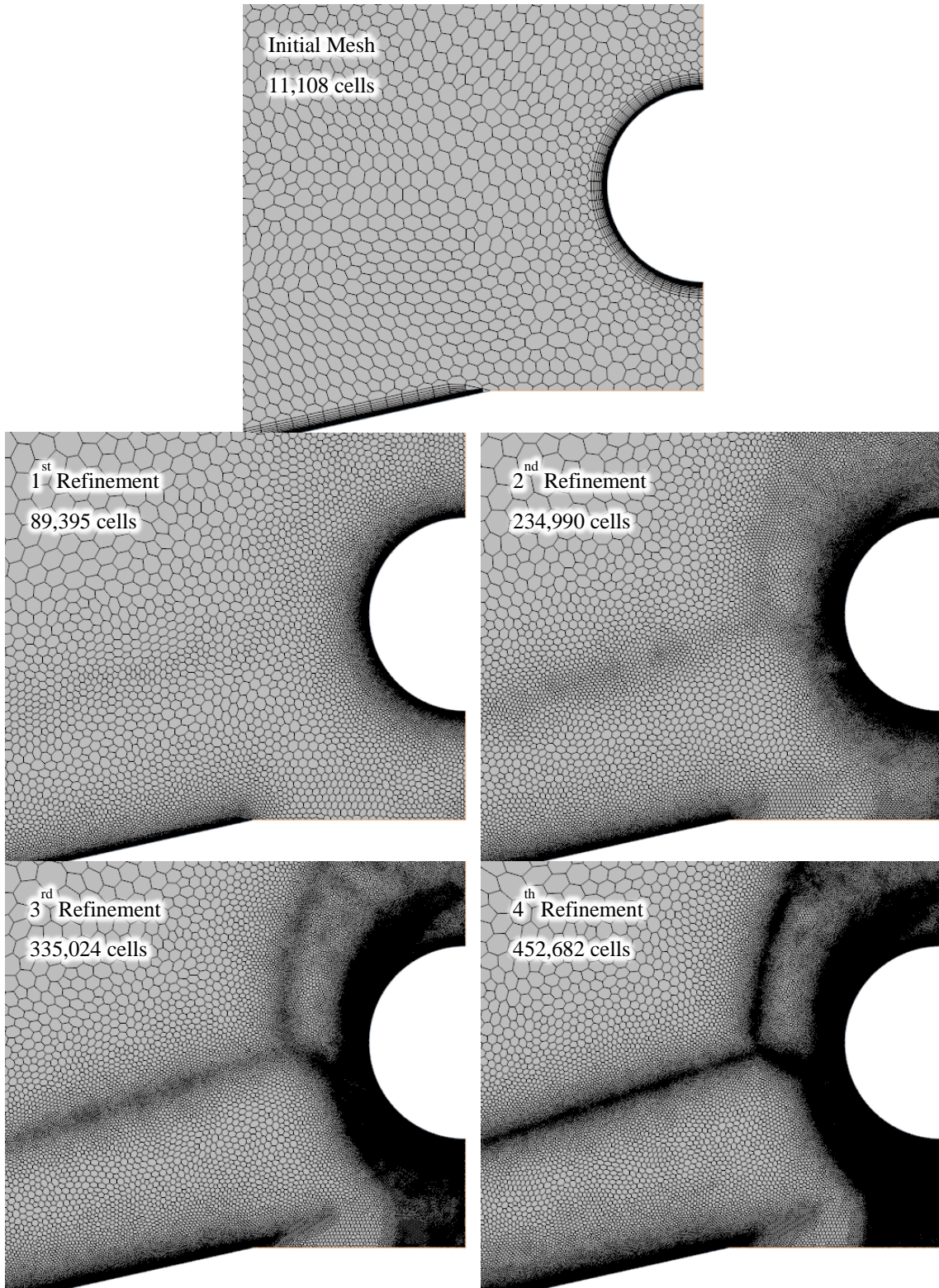


FIGURE 9. Example of Mesh Refinement Using Initial Pressure Gradient Technique.

In this technique, the quantity used for determining whether or not a cell in the baseline mesh should be refined is the pressure differential across the cell, computed as

$$\{\text{CellPressureDifferential}\} = \{\text{MagOfPressureGrad}\} * \{\text{CellSize}\} \quad (3)$$

(using STAR-CCM+ field function notation) where

$$\{\text{MagOfPressureGrad}\} = \text{mag}(\text{grad}(\{\text{AbsolutePressure}\})) \quad (4)$$

is the magnitude of the pressure gradient. Cell size (i.e., the average length across a cell) is based upon cell volume assuming that the cells are approximately isotropic and is computed differently depending on the dimensionality of the problem:

$$\{\text{CellSizeAxi}\} = \text{sqrt}(\{\text{Volume}\} / \{\text{RadialCoordinate}\}) \quad (5)$$

$$\{\text{CellSize2D}\} = \text{sqrt}(\{\text{Volume}\}) \quad (6)$$

$$\{\text{CellSize3D}\} = \text{pow}(\{\text{Volume}\}, (1/3)) \quad (7)$$

The pressure differential across a cell is then compared to user-specified threshold values to determine if a cell should be refined, coarsened, or left unchanged. A refinement flag variable is set based upon this comparison:

$$\{\text{CellRefinement}\} = (\{\text{CellPressureDifferential}\} > \{\text{CellRefineThreshold}\}) ? 1 : (\{\text{CellPressureDifferential}\} < \{\text{CellCoarsenThreshold}\}) ? -1 : 0 \quad (8)$$

This expression basically states that the cell refinement flag is set to 1 if the pressure differential across the cell is greater than the user-specified refinement threshold, or to -1 if the differential is less than the coarsening threshold. Otherwise, the flag is set to zero. Values of the refinement and coarsening threshold need to be specified by the user and will depend upon the problem being simulated. These values should be set such that the flow features the user wishes to refine are appropriately flagged, while regions of uniform flow are coarsened, as illustrated in Figure 10 for the shock/shock interaction test case run 60. As a point of reference, for this simulation the refinement threshold is set to 700 Pa, and the coarsening threshold is 0.1 Pa.

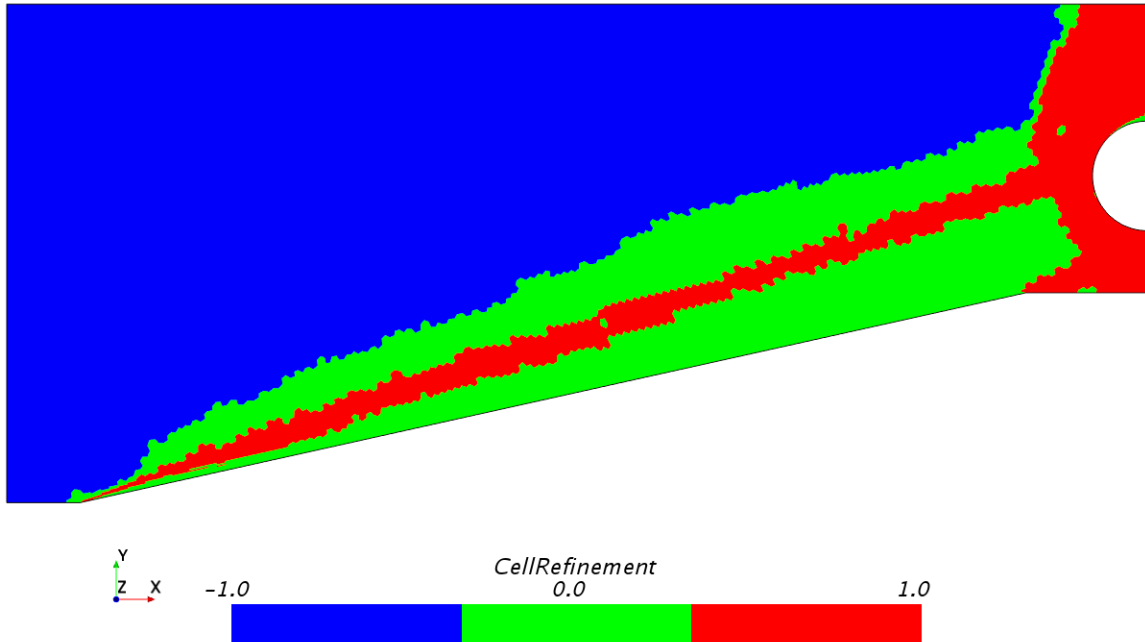


FIGURE 10. Cell Refinement Flag Computed From Baseline Solution for Shock/Shock Interaction Test Case.

The updated cell size is computed such that the change in cell size (before any limiting) does not exceed a factor of two:

$$\begin{aligned} \{\text{RefinedCellSize}\} = \max(\min(\{\text{CellRefinement}\} > 0) ? \{\text{CellSize}\}/2 : \\ (\{\text{CellRefinement}\} < 0) ? \{\text{CellSize}\}*2 : \\ \{\text{CellSize}\}, \{\text{MaxCellSize}\}, \{\text{MinCellSize}\}) \end{aligned} \quad (9)$$

Thus, the size of cells marked for refinement is cut in half, while cells marked for coarsening are doubled in size. These updated cell sizes are further limited to fall within user-specified maximum and minimum cell sizes. These limits prevent excessive refinement or coarsening of the mesh, and should be specified as suitable for any given problem.

This limited refined cell size is then extracted into an “internal” table and then used to specify the new cell size in the refined mesh. A STAR-CCM+ macro is written that adds all these necessary user field functions, sets up some useful scenes for visualizing the more important functions, and extracts the mesh refinement table. This macro allows this pressure gradient based mesh refinement to be applied to other STAR-CCM+ simulations.

This initial pressure gradient based mesh refinement technique is found to work rather well, but two areas for improvement have been identified. First of all, this

technique works well when all shocks have similar strength but if there are multiple shocks in the solution with significantly different strengths (such as is the case for the cylinder-flare test cases, for example), it is difficult to flag all shocks for refinement without also refining large areas that really do not require refinement. The second weakness is that this technique results in excessive refinement of the prism mesh in the boundary layer, even if these cells have not been flagged for refinement. This extra refinement comes as a result of how the cell size is computed based on an isotropic assumption, which is not appropriate for these highly anisotropic cells.

3.5.3 Normalized Pressure Gradient Mesh Refinement

The normalized pressure gradient mesh refinement technique is developed to address the two main weaknesses identified with the initial pressure gradient based refinement scheme. In order to be better able to refine multiple shocks of different strengths, cells are flagged for refinement based upon a normalized pressure differential:

$$\frac{\{\text{CellNormPressureDifferential}\}}{\{\text{AbsolutePressure}\}} = \frac{\{\text{MagOfPressureGrad}\} * \{\text{CellLength}\}}{\{\text{AbsolutePressure}\}} \quad (10)$$

This pressure differential is also computed based upon a cell length, instead of an average cell size. This cell length approximately corresponds to the largest dimension of a cell. For cells that are isotropic, this cell length and the average cell size are equivalent. However, for highly anisotropic cells (i.e., cells with low cell aspect ratio in the prism layer of the mesh), the cell length is larger than the cell size and provides a much more appropriate characterization of the cell. Computation of cell length is dependent upon the dimensionality of the problem:

$$\{\text{CellLengthAxi}\} = \frac{\text{sqrt}(\{\text{Volume}\} / \{\text{RadialCoordinate}\})}{\{\text{CellAspectRatio}\}} * (2 - \text{pow}(\{\text{CellAspectRatio}\}, 2)) \quad (11)$$

$$\{\text{CellLength2D}\} = \text{sqrt}(\{\text{Volume}\} / \{\text{CellAspectRatio}\}) * (2 - \text{pow}(\{\text{CellAspectRatio}\}, 2)) \quad (12)$$

$$\{\text{CellLength3D}\} = \text{pow}(\{\text{Volume}\} / \{\text{CellAspectRatio}\}, (1/3)) * (-1.0 * \text{pow}(\{\text{CellAspectRatio}\}, 3) + 1.0 * \text{pow}(\{\text{CellAspectRatio}\}, 2) - 0.68 * \{\text{CellAspectRatio}\} + 1.68) \quad (13)$$

Cell length is thus a function of both cell volume and cell aspect ratio. Cell aspect ratio is computed within STAR-CCM+ as a complex function of cell volume, number of faces, and face areas. Highly isotropic cells (such as perfect cubes) have an aspect ratio of one, while highly anisotropic cells (such as the thin cells in the prism layer) have aspect ratios approaching zero. The expressions for cell length are derived in this effort; the final

terms in these expressions are empirically derived correction factors to yield reasonable cell length values for all cell aspect ratios.

By using this cell length instead of the average cell size as the basis for the refined cell sizes, it is possible to avoid the unneeded refinement of the prism layer observed with the initial pressure gradient refinement method. Additionally, when flagging cells for refinement, an extra condition is introduced that prevents cells with aspect ratios below a user-defined threshold from being refined:

$$\begin{aligned} \{\text{CellNormRefinement}\} = & (\{\text{CellNormPressureDifferential}\} > \\ & \{\text{CellRefineNormThreshold}\}) ? ((\{\text{CellAspectRatio}\} < \\ & \{\text{PrismLayerRefineThreshold}\} ? 0 : 1) : \\ & (\{\text{CellNormPressureDifferential}\} < \\ & \{\text{CellCoarsenNormThreshold}\}) ? -1 : 0 \end{aligned} \quad (14)$$

This also helps prevent unnecessary refinement of the prism layer. The threshold value for cell aspect ratio used in this work is 0.1. It is also observed that the refinement and coarsening thresholds in this approach are less sensitive to freestream conditions and require less adjustment from problem to problem.

Finally, the refined (or coarsened) cell sizes are computed for the flagged cells based on the cell length of the baseline mesh:

$$\begin{aligned} \{\text{CellSizeNormRefined}\} = & \max(\min((\{\text{CellNormRefinement}\} > 0) ? \\ & \{\text{CellSize}\}/2 : (\{\text{CellNormRefinement}\} < 0) ? \{\text{CellSize}\}*2 : \\ & \{\text{CellLength}\}, \{\text{MaxCellSize}\}), \{\text{MinCellSize}\}) \end{aligned} \quad (15)$$

As before, this refined cell size is extracted into a table internal to the STAR-CCM+ simulation and used to specify the new cell size in the refined mesh. An example of a sequence of meshes for the small cylinder-flare test case refined using this normalized pressure gradient technique is illustrated in Figure 11. It can be observed that this method refines both the weak shock from the leading edge of the cylinder, as well as the stronger shock over the flare. Additionally, the prism layer mesh is not being excessively refined.

All the test cases considered in this effort are either two-dimensional or axisymmetric. However, the suitability of the normalized pressure gradient technique for three-dimensional problems has been evaluated by using this technique for simulations of a Mach 7 waverider vehicle. The baseline and refined meshes are visualized in Figure 12. It can be seen that the shocks and wake region are being refined, as expected, without excessive refinement in the prism layer. Additionally, the cell count is observed to increase by about a factor of three with each refinement, which seems reasonable. The resulting flowfield around the waverider is illustrated in Figure 13.

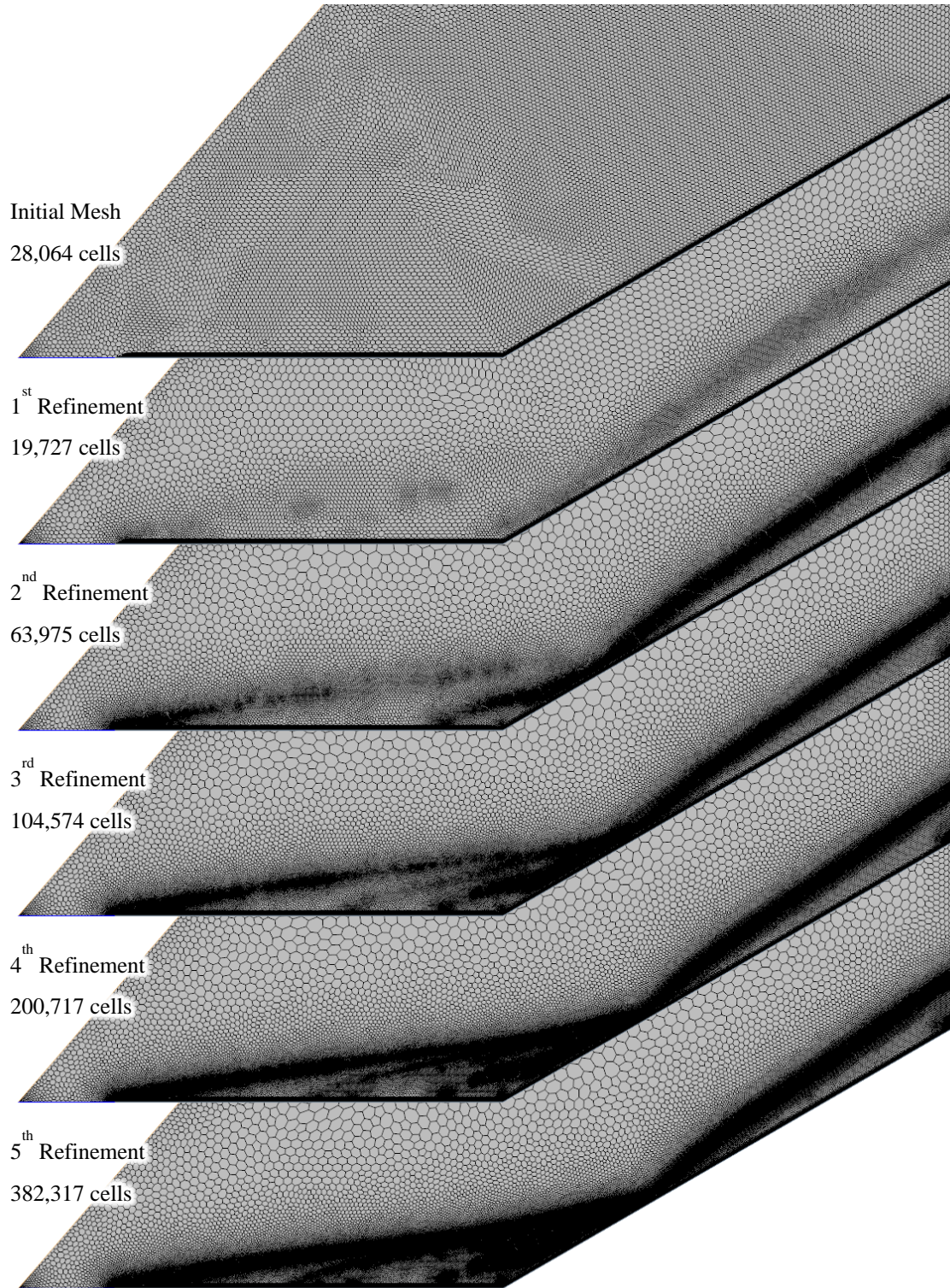


FIGURE 11. Example of Mesh Refinement Using Normalized Pressure Gradient Technique.

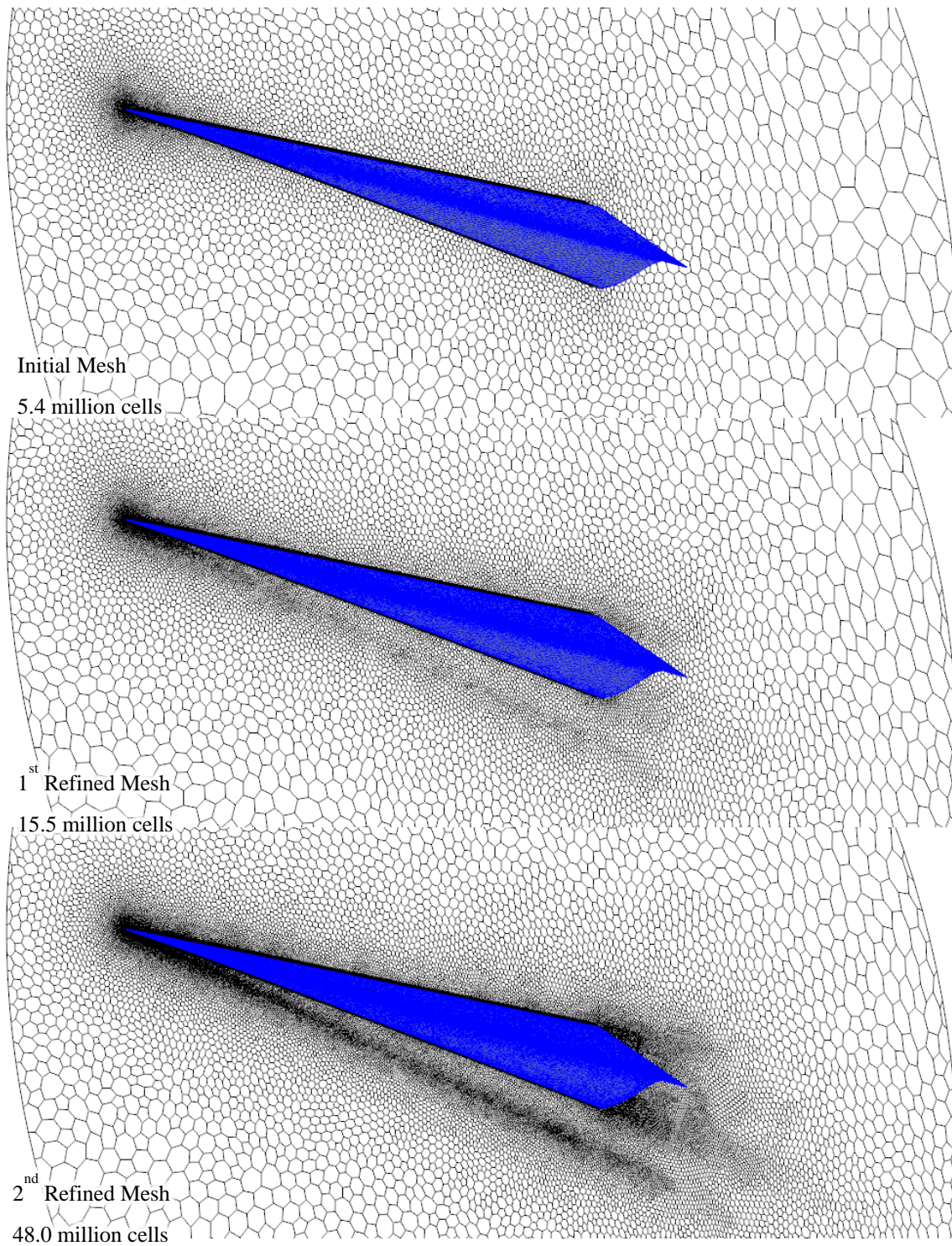


FIGURE 12. Example of Normalized Pressure Gradient Mesh Refinement Applied to Three-Dimensional Simulation of Waverider.

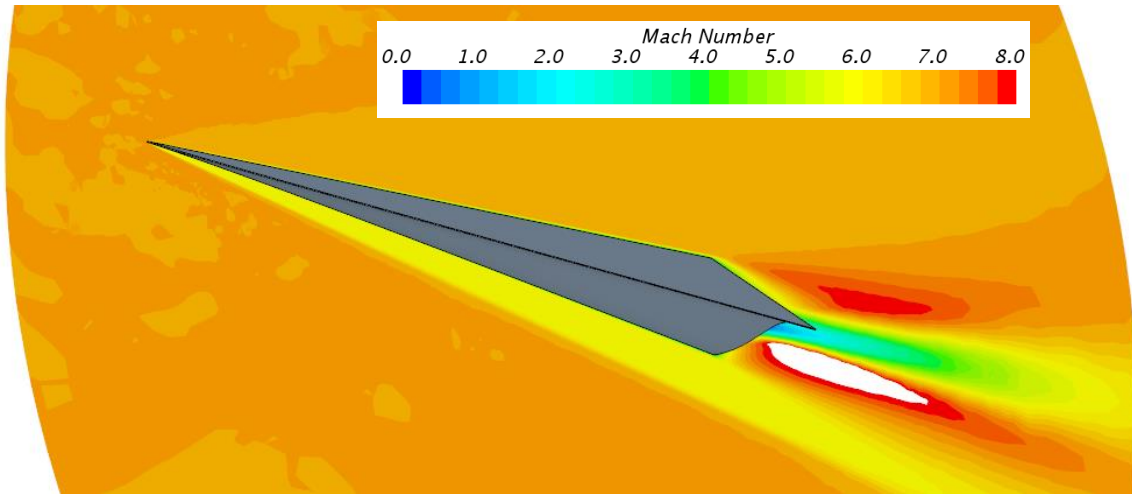


FIGURE 13. Flowfield Around Waverider Computed Using Refined Mesh.

A STAR-CCM+ macro is prepared that allows this normalized pressure gradient mesh refinement technique to be incorporated easily into other simulations. This technique is considered to be significantly superior to the initial method, and should be considered for use in future simulations of supersonic or hypersonic flows.

4.0 RESULTS

4.1 DOUBLE CONE

The double cone test case is the primary test case considered in the FY14 effort and is also revisited as part of the FY18 work. However, different test runs are simulated in the two efforts. The test runs simulated in the FY14 effort feature significant freestream nonequilibrium, which cannot be properly handled by STAR-CCM+. The FY18 work simulates newer test runs, unavailable at the time of the FY14 effort, which have thermodynamic equilibrium in the freestream, and can therefore be properly modeled by STAR-CCM+.

4.1.1 FY14 Effort

During the FY14 effort simulations were performed for the double cone experimental runs 80 (nitrogen) and 39 (air). Three noteworthy simulations were performed for each test case. (Numerous additional simulations were also performed as part of the process to identify the best analysis procedures, but these will not be discussed in detail.)

For run 80, these notable simulations are, in order of increasing complexity

- Single species (N_2) with thermal equilibrium,
- Single species (N_2) with thermal nonequilibrium,
- Multiple species (N_2 , N), non-reacting, with thermal nonequilibrium.

For run 39, the notable simulations are

- Equilibrium air model,
- Multiple species (N_2 , O_2 , NO, N, O), non-reacting, with thermal equilibrium,
- Multiple species (N_2 , O_2 , NO, N, O), Dunn/Kang reaction model, with thermal equilibrium.

A medium-density structured mesh is used for all of these simulations, as illustrated in Figure 8 and discussed in detail in Section 3.5.1. STAR-CCM+ version 9 is used for these FY14 simulations. Due to the small number of cells included in the mesh, computations are performed using only a single processor. Convergence of the simulations is determined by monitoring the integrated and peak heat flux on the double cone geometry.

The single species, thermal equilibrium simulation for the double cone run 80 uses the following notable solver settings in STAR-CCM+: AUSM+ flux method, a positivity rate limit of 0.2 (the default), an explicit relaxation value of 0.75, and a value of 1.0 for the CFL number. The “expert driver” feature is deactivated. Viscosity for nitrogen is tabulated as a function of temperature, based on Blottner’s curve fits (Reference 21). Similarly, thermal conductivity is tabulated as a function of temperature based upon Eucken’s relations (Reference 21) and includes the contributions from the translational-rotational and vibrational-electronic energy modes. Specific heat is specified as a polynomial with respect to temperature; this polynomial is refit to the data obtained from Reference 23 and is extended down to temperatures as low as 10 K. This simulation is initialized by ramping the freestream Mach number from a low starting value to the final condition over the course of several hundred iterations.

The second simulation for double cone run 80 builds upon the settings and properties used in the first simulation, with updates as necessary in order to be able to model thermal nonequilibrium. The thermal nonequilibrium solver is activated, with the Landau-Teller mode relaxation time model. The constants necessary for this model are taken from Reference 1. The specific heat for the translational-rotational model is modeled using the “fully excited” model, while the “gas kinetics” is used for the specific heat of the vibrational-electronic mode. The default values for the vibrational and electronic partition functions are in good agreement with Scalabrin (Reference 21) and are used without modification. Separate tables are computed for the thermal conductivity of the translational-rotational and vibrational-electronic energy modes, based upon Eucken’s relations.

The third double cone run 80 simulation includes setting updates permitting the modeling of a multi-species mixture. The Chapman-Enskog model is used to compute the viscosity of each species, while the non-equilibrium kinetic theory model is used to compute the thermal conductivity for the two energy modes. Mixture viscosity and thermal conductivities are computed from the species values based upon the Mathur-Saxena averaging method. One notable difference for this simulation from the previous is that the specific heat of the vibrational-electronic mode is computed based upon a polynomial with respect to temperature and not the gas kinetics model. The gas kinetics model is viewed as the preferred method, but significant difficulties were encountered that appear to be associated with near-zero or negative specific heat values computed for the low temperatures in the freestream. By using a modified polynomial for specific heat, it is possible to avoid these difficulties. It is also noteworthy that this simulation can be successfully initialized by setting freestream values everywhere in the domain.

The first simulation for the double cone run 39 uses the same solver settings as were used for the first simulation for run 80. However, the gas was modeled using the “equilibrium air” model built into STAR-CCM+. This equilibrium air model computes all gas properties as a function of temperature and pressure, assuming thermodynamic equilibrium and equilibrium chemistry. It is possible to initialize this simulation using the grid sequencing initialization feature.

The second simulation for this run does not use a built-in air model but instead models air as a non-reacting mixture of five species: N_2 , O_2 , NO , N , and O . For each species, the specific heat is computed based upon the default NASA polynomial included in the STAR-CCM+ material database. Species viscosity is computed using Blottner’s coefficients (Reference 21) and tabulated as a function of temperature; thermal conductivity is computed based on Eucken’s relations and likewise tabulated. This simulation does not initialize successfully using the grid sequencing initialization feature or by ramping the freestream conditions. However, an impulsive start initialization works well. The “expert driver” feature is activated for this simulation.

The third simulation for run 39 is based upon the second but models reactions using the Dunn/Kang mechanism (Table 8) and the eddy break-up (EBU) reaction model in STAR-CCM+. However, reaction rates are computed exclusively based upon the kinetic data (and not based upon mixing or turbulence as is usually the case when using the EBU reaction model).

For the single species, thermal equilibrium simulation performed for run 80, the “steady-state” solution converges to a constant amplitude oscillating solution. Convergence behavior for the integrated and peak heat flux on the double cone model is plotted in Figure 14. The heat flux profiles on the double cone geometry are shown in Figure 15, compared to the experimental measurements. Profiles corresponding to the instances of maximum and minimum peak heat flux are plotted, along with the two-cycle average heat flux.

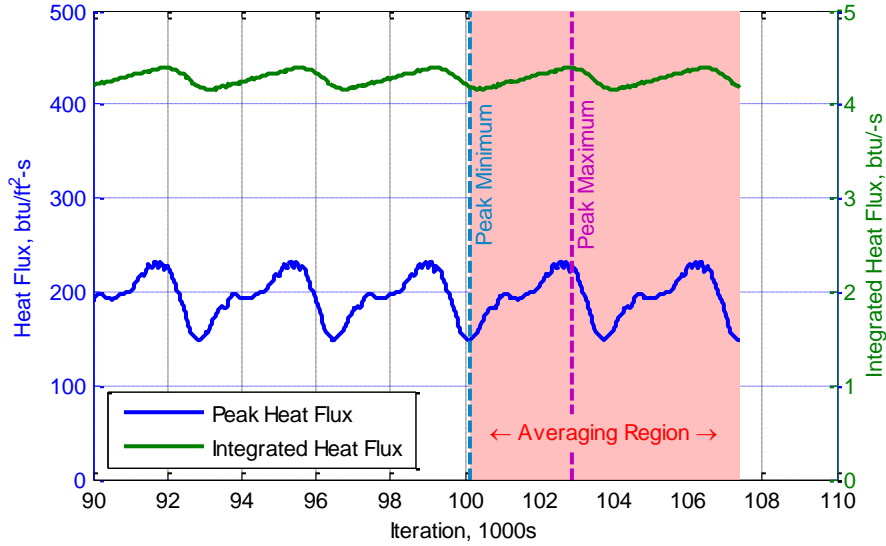


FIGURE 14. Heat Flux Convergence Behavior for Single Species, Thermal Equilibrium Simulation of Double Cone Run 80.

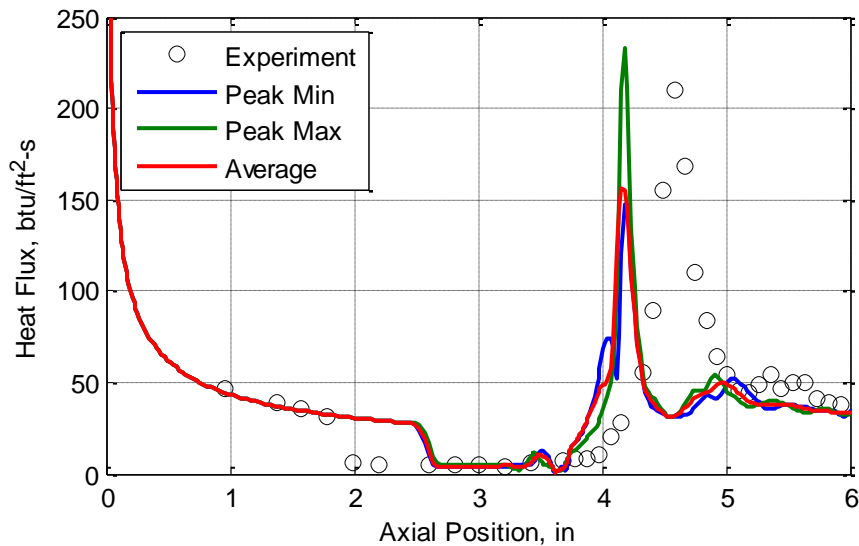


FIGURE 15. Heat Flux as Predicted by Single Species, Thermal Equilibrium Simulation of Double Cone Run 80, Compared to Experimental Measurements.

From these heat flux profiles, it is observed that the predicted separation bubble is smaller than that measured in the experiment. Separation of the flow is predicted to occur at an axial position of 2.5 inches, while in the experiment separation occurs slightly upstream of 2.0 inches. As a result of the delayed separation, the peak heat flux (which

correlates with flow reattachment) in the simulation is shifted upstream of the location observed in the experiment. However, the magnitude of the predicted heat flux does agree quite well upstream of flow separation, within the separation bubble, and downstream of flow reattachment.

Images of the flowfield (temperature, Mach number, and velocity) around the double cone model are presented in Figure 16. These values have been averaged over two periods of the converged oscillations, hence the smudging of some of the shocks. A closer view of the separation bubble is given in Figure 17. Investigations of the solution reveal that the point of flow separation remains essentially fixed. However, the thickness of the separation bubble in the wall-normal direction and the position of the separation shock are unsteady. The separation shock appears to be “flapping,” with the separation point as a pivot point, which causes the downstream flow features to also oscillate.

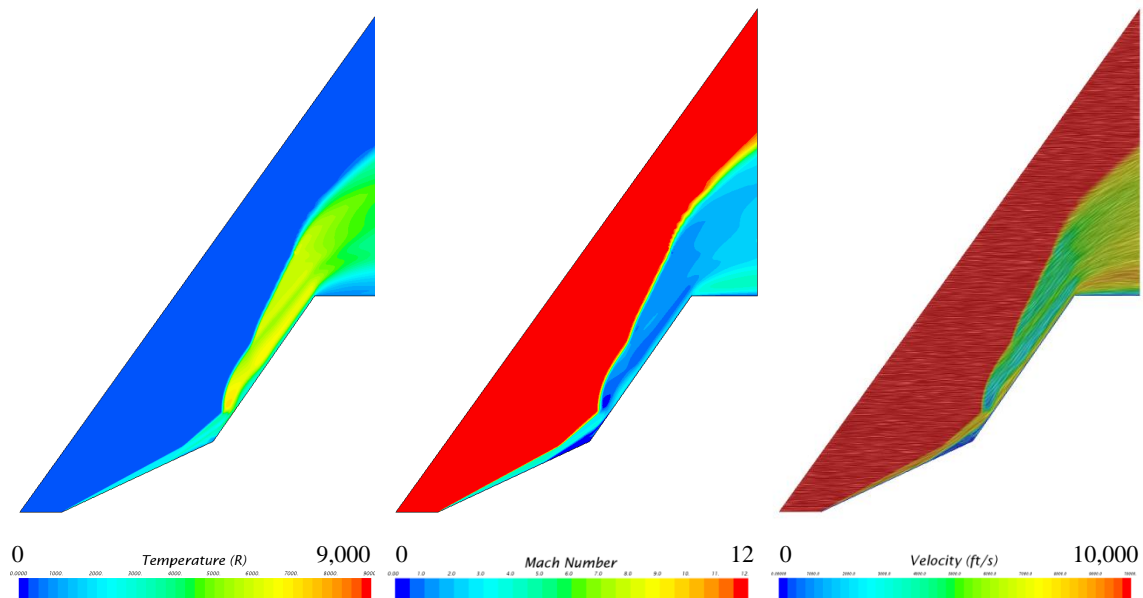


FIGURE 16. Averaged Temperature, Mach Number, and Velocity as Predicted by Single Species, Thermal Equilibrium Simulation of Double Cone Run 80.

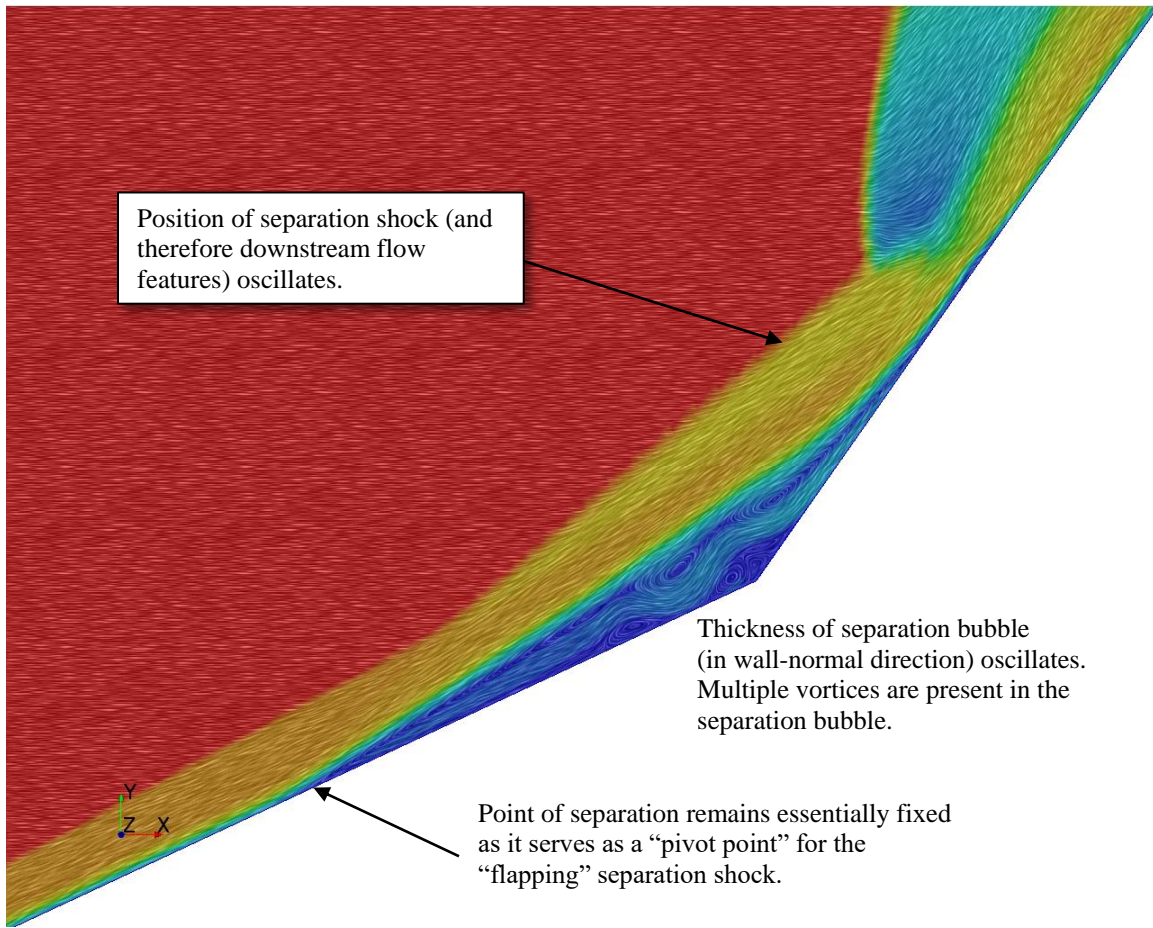


FIGURE 17. Detailed View of Flow Separation as Predicted by Single Species, Thermal Equilibrium Simulation of Double Cone Run 80.

The second simulation for run 80 models the effects of thermal nonequilibrium and as before, converges to an oscillating solution. One notable difference in this simulation is that the predicted point of flow separation has moved upstream to an axial position of 2.25 inches (see Figure 18). Thus, the agreement with the experiment is improved, but the size of the separation bubble remains under-predicted.

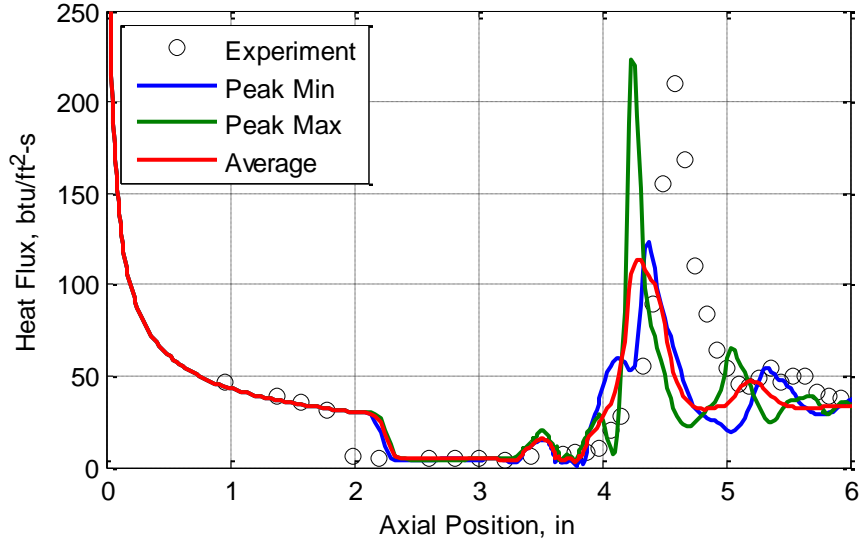


FIGURE 18. Heat Flux as Predicted by Single Species, Thermal Nonequilibrium Simulation of Double Cone Run 80, Compared to Experimental Measurements.

Images of the two temperatures (translational-rotational and vibrational-electronic) and Mach number are given in Figure 19; these values have been averaged over two periods of the converged oscillations. A spot of high translational-rotational temperature is observed above and to the left of the corner between the second cone and the cylinder portion of the geometry. This is believed to be caused by the structured directed mesh that was used, which has high skewness in this region. The vibrational-electronic temperature distribution is in line with expectations based on the finite-rate vibrational relaxation process. The highest vibrational-electronic temperatures occur some distance downstream of the strong shock over the second cone. Elevated vibrational-electronic temperatures are also observed in the separation bubble, which is believed to be due to the increased residence time of flow in this region. As with the previous simulation, the point of flow separation appears to be fixed, but the separation shock appears to be flapping, which affects the downstream flow.

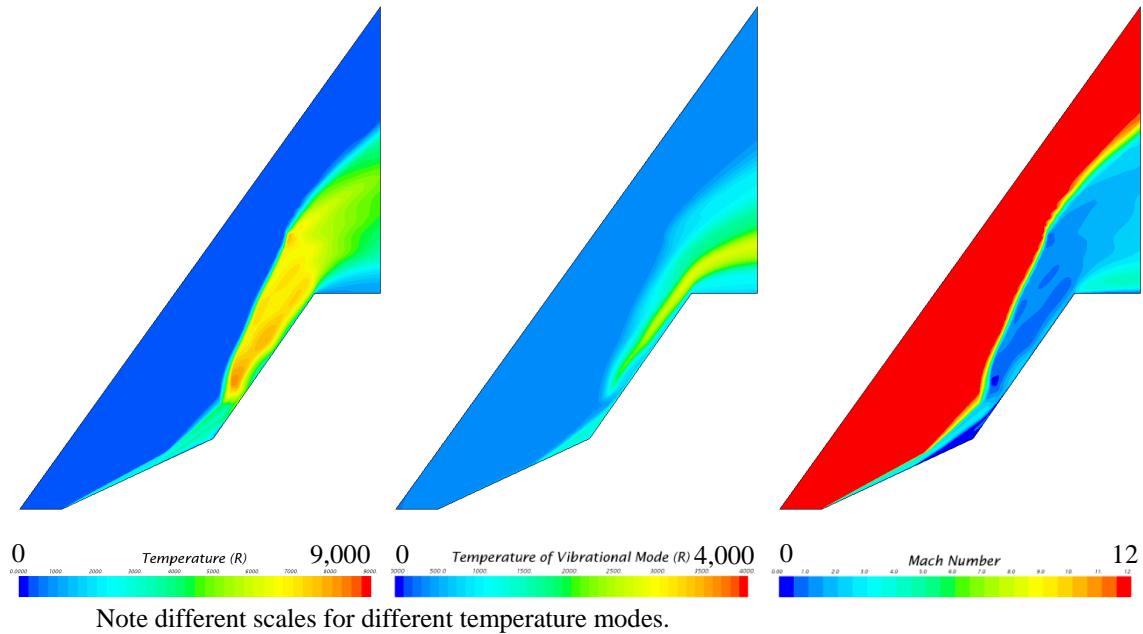


FIGURE 19. Averaged Translation-Rotational and Vibrational-Electronic Temperature and Mach Number as Predicted by Single Species, Thermal Nonequilibrium Simulation of Double Cone Run 80.

The final simulation for the double cone run 80 test case models multiple species (N_2 and N) produced in the nonequilibrium freestream. Chemical reactions are not modeled. The convergence behavior and heat flux profiles for this simulation are nearly identical to those from the previous simulation. However, the predicted distribution for vibrational-electronic temperature is somewhat different from that predicted by the single species simulation and appears to have nonphysical features produced by numerical difficulties; see Figure 20. The vibrational-electronic temperatures predicted by the multiple species simulations overall are higher than those predicted with the single species simulation. This is possibly because collisions with N atoms are more efficient at equilibrating the vibrational mode than are collisions with N_2 molecules. However, the mass fraction of N atoms is so low that it seems unlikely to make such a difference. (It is also possible, but unlikely, that it is simply a post-processing issue where different color scales have inadvertently been applied. Unfortunately, the simulation files are unavailable so this cannot now be verified.)

Of greater concern are elevated vibrational-electronic temperatures predicted by the multispecies simulation in regions where lower values were predicted by the single species simulation. These appear to be nonphysical and are likely caused by numerical difficulties produced by the separation shock crossing skewed cells in the mesh, as illustrated in Figure 21. The multispecies simulation appears to be more sensitive to mesh quality, as this same mesh was used for the single species simulation without issue. The cause for this sensitivity is unknown.

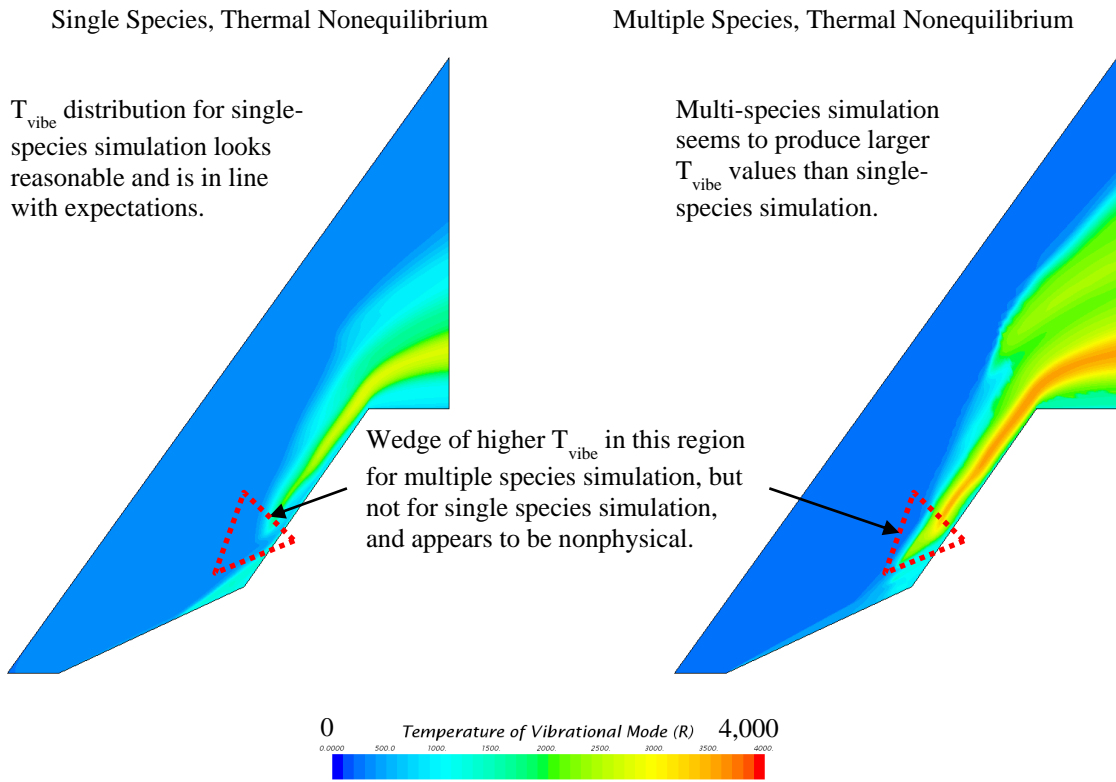


FIGURE 20. Comparison of Vibrational-Electronic Temperature Predicted by Single and Multiple Species Simulations for Double Cone Run 80.

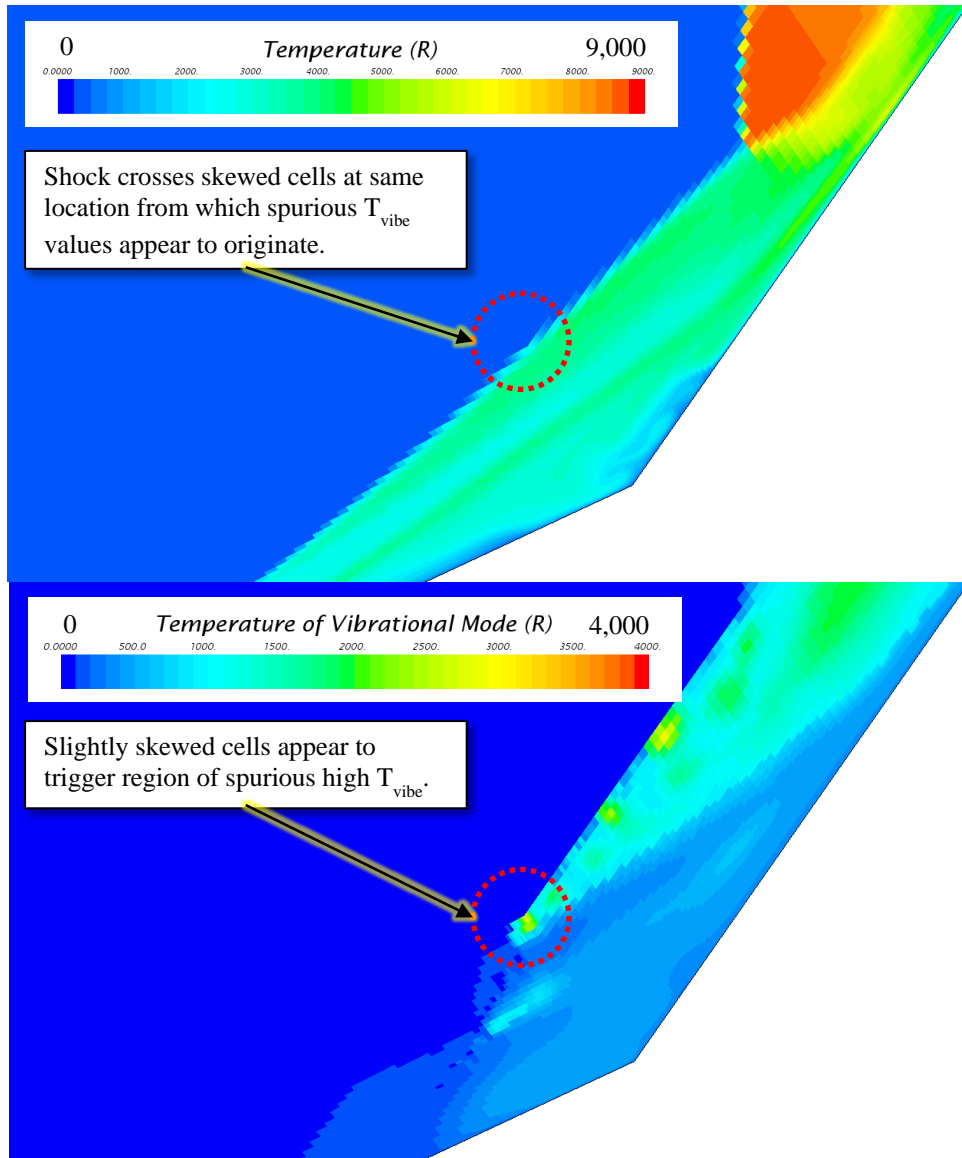


FIGURE 21. Detailed View of Translational-Rotational and Vibrational-Electronic Temperatures in Separated Flow Region as Predicted by Multiple Species, Thermal Nonequilibrium Simulation for Double Cone Run 80.

The heat flux profiles predicted by the three simulations for double cone run 80 are compared to experimental data in Figure 22. All simulations under-predict the size of the separation bubble, but the simulations modeling thermal nonequilibrium provide noticeably improved agreement with the measurements. Simulations capturing freestream nonequilibrium may lead to better agreement with the experiment, but STAR-CCM+ still does not have the capability to specify freestream nonequilibrium. There is negligible difference between the single and multiple species simulations, which is reasonable considering the low freestream mass fraction of N atoms and the fact that chemistry is not modeled. A simulation modeling chemistry is not attempted for this case, primarily due to the relatively low amount of dissociation expected at these conditions.

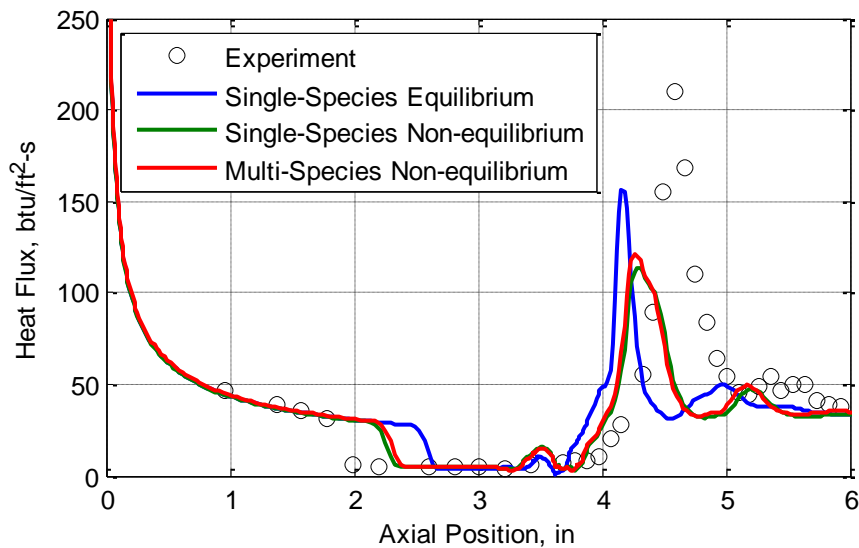


FIGURE 22. Comparison of Heat Flux as Predicted by Different Simulations for Double Cone Run 80.

The translational-rotational temperature distributions predicted by the three simulations for run 80 are compared in Figure 23. The thermal equilibrium simulation predicts lower translational-rotational temperatures than are predicted by the two nonequilibrium simulations (which are comparable to each other). This is as expected; the equilibrium model essentially assumes that the vibrational relaxation process is infinitely fast. As a result, more energy is transferred from the translational-rotational mode to the vibrational mode than would occur in the finite-rate process.

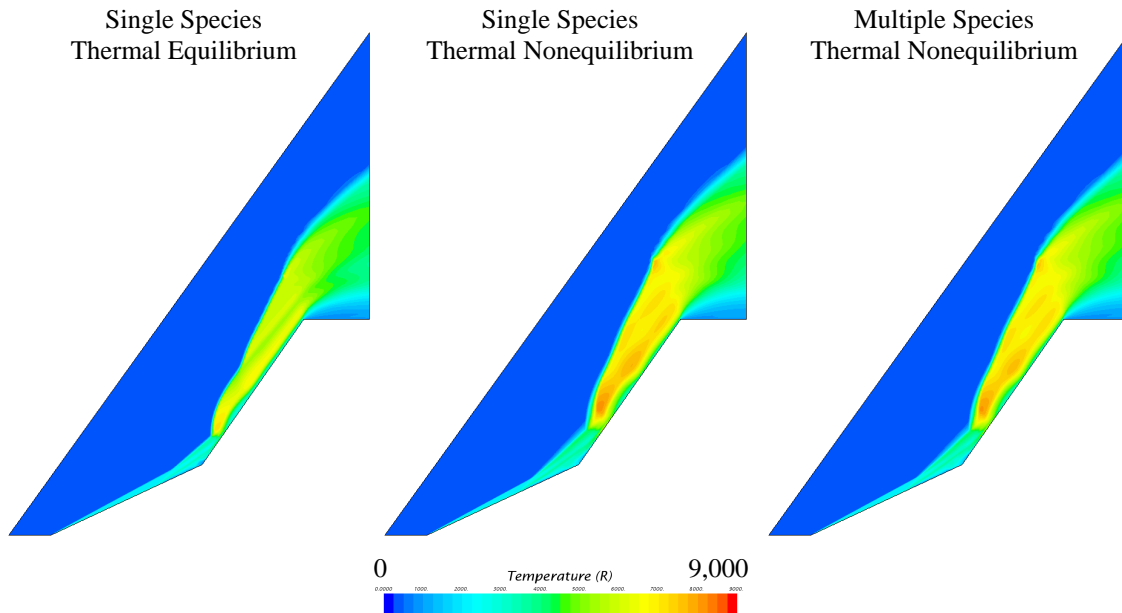


FIGURE 23. Comparison of Temperature Distribution as Predicted by Different Simulations for Double Cone Run 80.

The flowfields near the separation bubble as predicted by the two single species simulations for run 80 are compared in Figure 24. Arrows have been added as reference points to make comparisons easier. It is observed that the simulation modeling thermal nonequilibrium predicts a significantly larger separation bubble than is predicted by the simulation modeling thermal equilibrium. This, in turn, affects the stand-off distance of the separation shock, as well as downstream flow features.

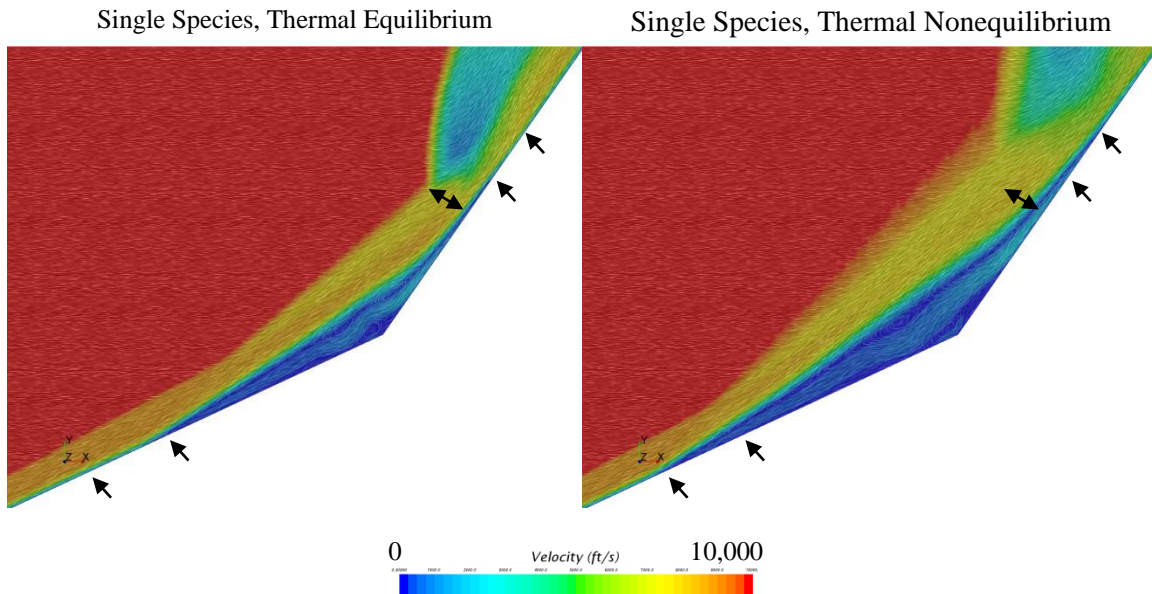


FIGURE 24. Detail of Flowfield Near Separation Bubble for Equilibrium and Nonequilibrium Single Species Simulations for Double Cone Run 80.

The first simulation attempted for the double cone run 39 uses the equilibrium air model included with STAR-CCM+. Interestingly, this simulation converges to a steady solution without oscillations. The predicted heat flux profile is presented in Figure 25. It is observed that the predicted separation bubble is much smaller than that observed experimentally. The point of separation is predicted to occur at an axial station of approximately 3.0 inches, while in the experiment separation was observed to take place just upstream of the 2.0-inch axial position. The region of high heat flux in the flow reattachment zone is divided into two peaks by a small, secondary separation bubble (see Figure 26). As was observed with run 80, the heat flux predictions are in good agreement with the measurements upstream of and within the flow separation and downstream of the flow reattachment.

The second simulation for run 39 models air with multiple species (N_2 , O_2 , NO , N , O) but does not model chemistry or thermal nonequilibrium. This simulation converges to a steady-state oscillating solution, as was encountered for the run 80 simulations. Heat flux profiles corresponding to the instances of maximum and minimum peak heat flux are plotted, along with the one-cycle average heat flux in Figure 27. The point of flow separation is at an axial position of about 2.5 inches. This is farther upstream than predicted with the equilibrium air model but still significantly downstream of the measured separation point.

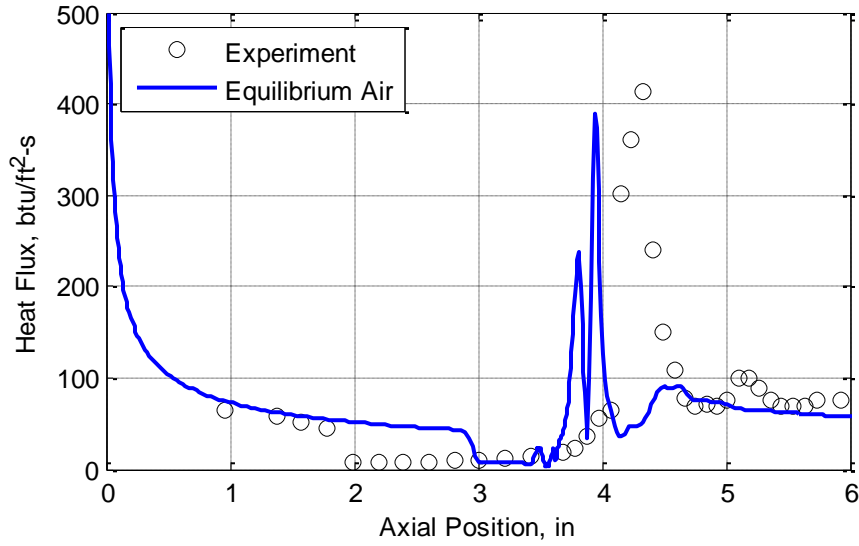


FIGURE 25. Heat Flux as Predicted by Equilibrium Air Simulation of Double Cone Run 39, Compared to Experimental Measurements.

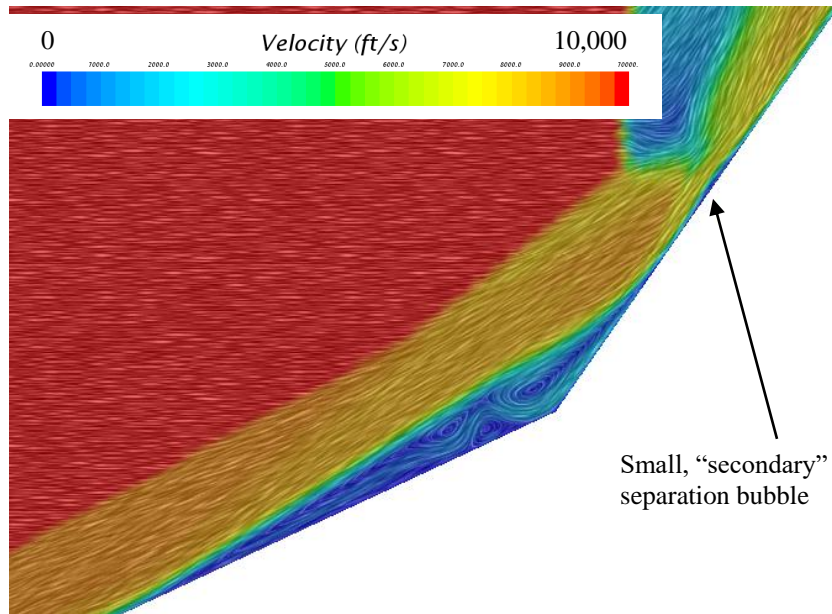


FIGURE 26. Primary and Secondary Flow Separation Bubbles Predicted by Equilibrium Air Simulation of Double Cone Run 39.

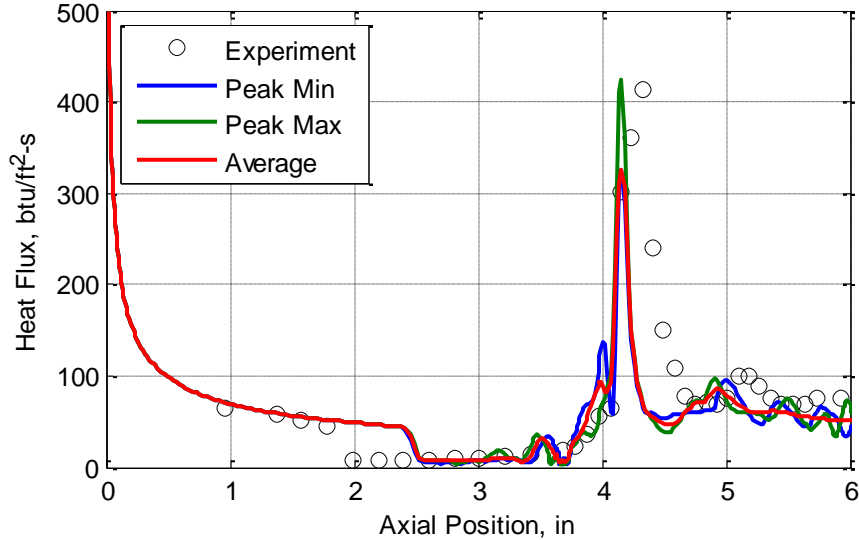


FIGURE 27. Heat Flux as Predicted by Multiple Species, Non-Reacting Simulation of Double Cone Run 39, Compared to Experimental Measurements.

The final simulation performed for run 39 models chemistry using the Dunn/Kang mechanism (see Table 8), thermal equilibrium is assumed. The heat flux profiles are presented in Figure 28; the average value is averaged over six cycles. The predicted heat flux profiles are very similar to those obtained from the non-reacting simulation. It should be noted that this simulation goes on to experience massive (nonphysical) flow separation. Attempting this simulation a second time from a fresh initialization produces the same result. The cause for this is unknown.

The average heat flux profiles from all three simulations for double cone run 39 are compared in Figure 29. This clearly shows how the multi-species simulations provide improved agreement with the experiment when predicting the size of the separation bubble. The equilibrium air model does not appear to be suitable for this type of flowfield. Modeling reactions with the Dunn/Kang mechanism appears to have minimal impact on heat flux predictions, which suggests that the extra expense of modeling the reactions is unnecessary. However, additional reaction mechanisms should probably be explored. It is also believed that better agreement with the experiment might be obtained if thermal nonequilibrium were modeled. However, it was not possible to complete these additional simulations as part of the FY14 effort.

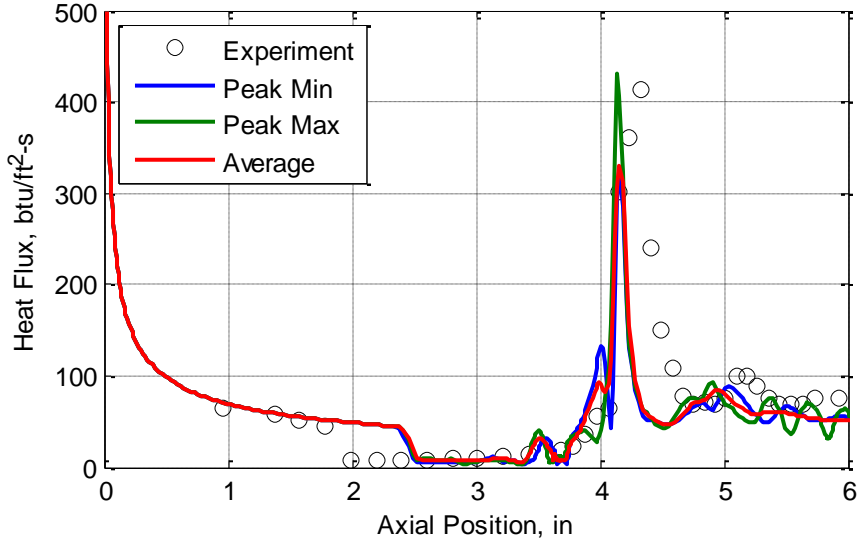


FIGURE 28. Heat Flux as Predicted by Multiple Species, Reacting Simulation of Double Cone Run 39, Compared to Experimental Measurements.

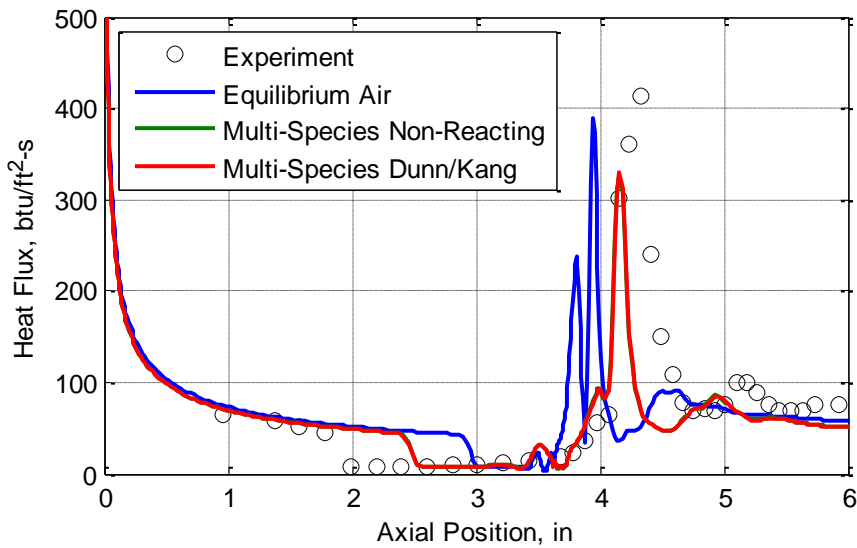


FIGURE 29. Comparison of Heat Flux as Predicted by Different Simulations for Double Cone Run 39.

The temperature distributions predicted by the three simulations for run 39 are compared in Figure 30. It is observed that lower temperatures are predicted for the equilibrium air simulation than are predicted for the other simulations. This is because the equilibrium air model essentially assumes that the vibrational relaxation and chemical reaction processes are infinitely fast; additional energy is being absorbed by these reactions and vibrational relaxation. The temperatures predicted by reacting-flow simulation are very similar to those predicted by non-reacting (frozen composition) simulation. This suggests that the time scale of the reactions is large compared to flow characteristic time.

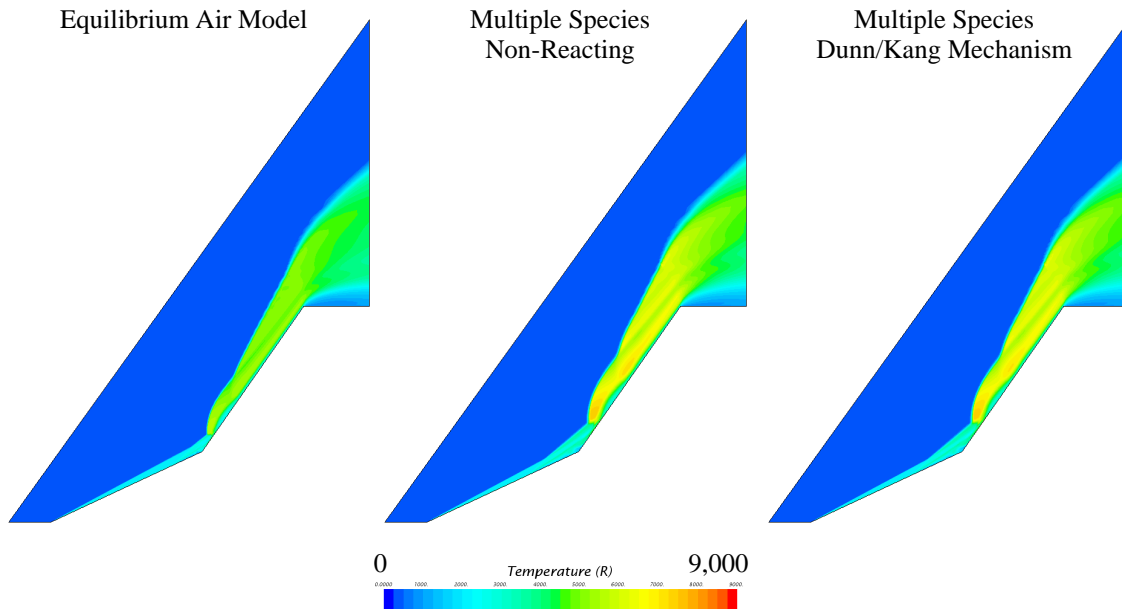


FIGURE 30. Comparison of Temperature Distribution as Predicted by Different Simulations for Double Cone Run 39.

The mass fraction distributions for the dissociation products (NO, N, O) as predicted by this final simulation for double cone run 39 are compared in Figure 31. As expected, the dissociation products occur in the high-temperature regions of the flow. Oxygen shows a significant level of dissociation, while nitrogen undergoes minimal dissociation. This is in line with expectations, based upon the temperatures experienced in the flow.

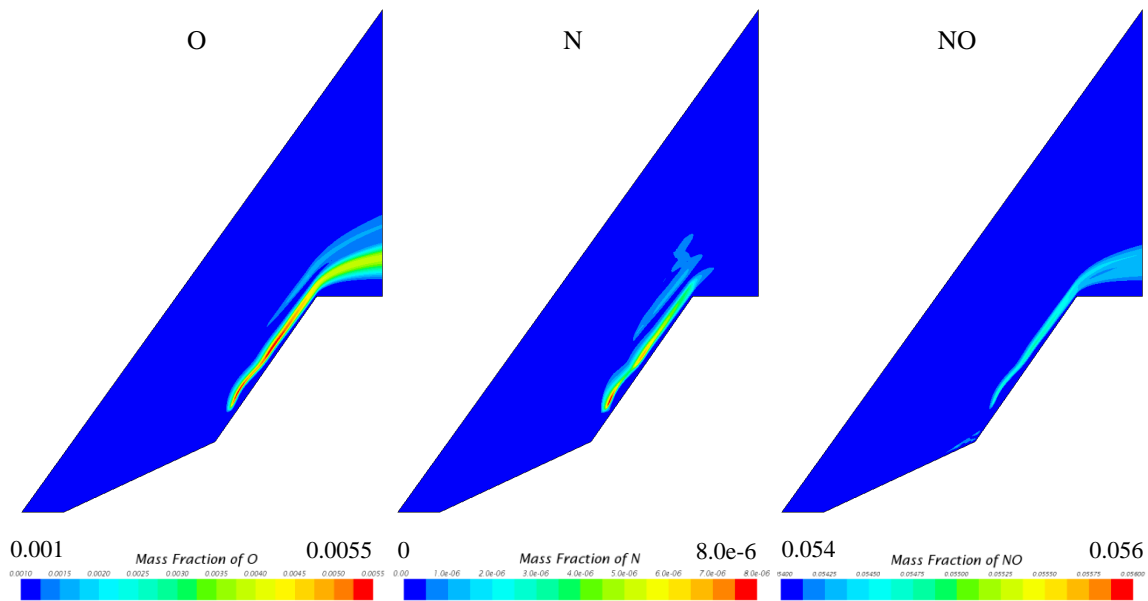


FIGURE 31. Mass Fraction Distribution for Dissociation Product Species as Predicted by Multiple Species, Reacting Simulation of Double Cone Run 39.

4.1.2 FY18 Effort

The laminar double cone geometry is revisited in the FY18 effort, with the emphasis being on simulating the newer experiments having thermodynamic equilibrium in the freestream. Specifically, runs 1, 2, 3, and 5 have been simulated; freestream conditions are given in Table 2. These simulations are performed using the recommended solver settings identified and discussed in Section 3.2. Results are presented for simulations performed using the five species gas model incorporating reactions (using the Dunn/Kang mechanism) and thermodynamic nonequilibrium. The simulation performed for run 1 computes mixture viscosity using a mass-weighted method, instead of the Mathur-Saxena averaging method used for all the other simulations. Check simulations performed for run 2 indicate that there is negligible difference in the results produced using the two methods. An additional simulation is performed for run 1 using the two species gas model, but there is negligible difference observed for the two gas models. Convergence of these simulations is determined by monitoring the location of flow separation, as well as the minimum, maximum, and average pressure and heat flux on the model surface.

The mesh used in these simulations is refined three times based on the initial pressure gradient technique discussed in Section 3.5.2. As discussed in Section 3.5.2, this technique results in additional refinement of the mesh in the prism layer. The prism layer mesh is designed such that wall Y^+ (for a preliminary, turbulent simulation) remains

below 0.8. The original mesh contains approximately 18 thousand cells, with subsequently refined meshes containing on the order of 60, 225, and 450 thousand cells.

The simulation for run 1 is observed to converge to a constant amplitude oscillating solution. The flowfield at the upstream and downstream limits of flow separation is illustrated in Figure 32 with numerical Schlieren images. The heat flux and pressure distributions are presented in Figures 33 and 34, respectively. These plots compare the maximum, minimum, and average profiles encountered for one cycle of the oscillating solution. It can be observed from these plots that separation of the flow is predicted to occur significantly farther downstream than was observed experimentally (2.8 to 2.9 inches, versus approximately 2.65 inches). The location of flow separation is observed to vary only by about 0.1 inch as the solution oscillates, but predictions downstream are observed to vary quite significantly as the solution oscillates. This is due to the flapping of the separation shock, as was observed in the FY14 simulations. The peak values of the average predicted pressure and heat flux profiles agree reasonably well with the peak values observed in the experiment, but occur farther upstream. This is due to the predicted location of flow separation being aft of the observed location. Pressure and heat flux predictions upstream of, within, and downstream of the separation bubble agree reasonably well with the experimental measurements.

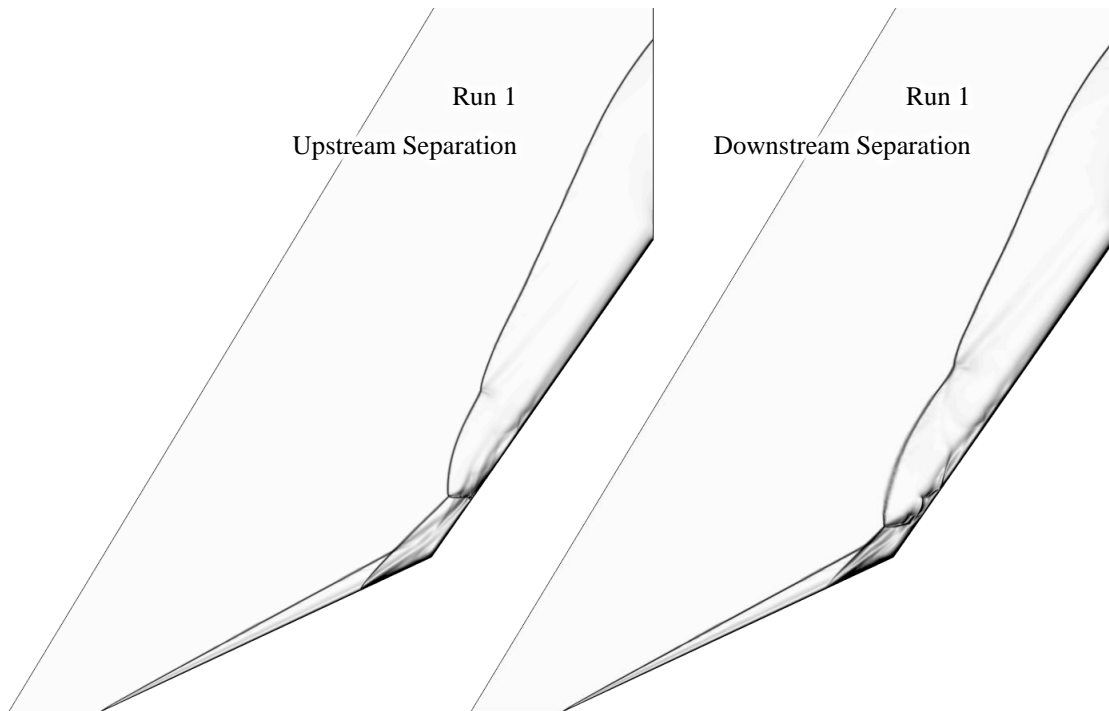


FIGURE 32. Numerical Schlieren Images of Flowfield Predicted for Double Cone Run 1.

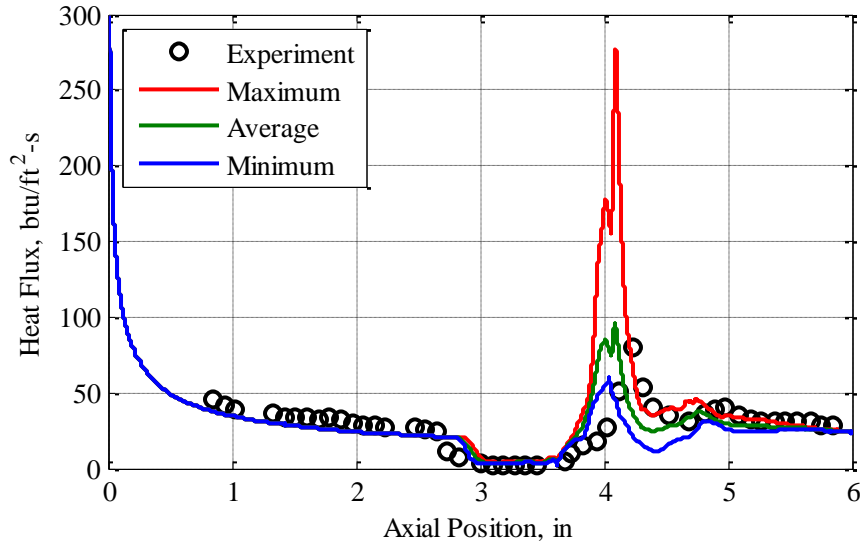


FIGURE 33. Heat Flux Distribution for Double Cone Run 1 as Predicted Using Five Species Air Model, Compared to Experimental Measurements.

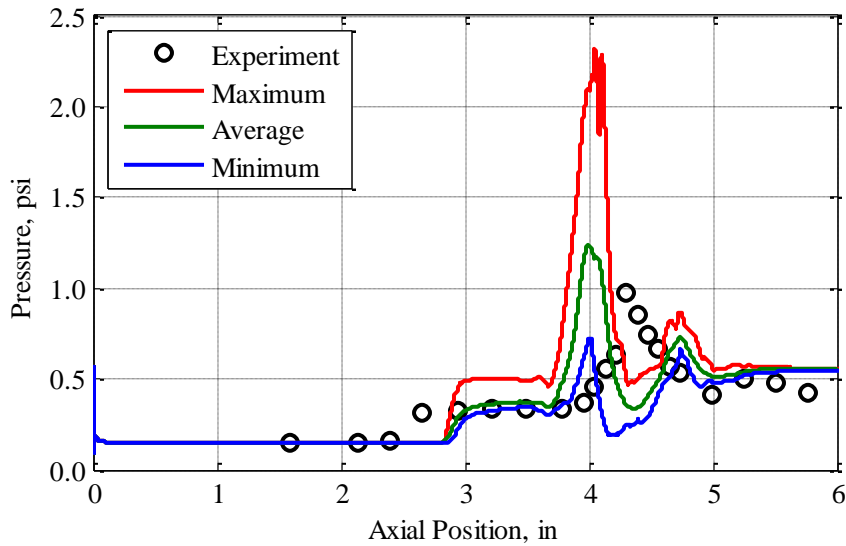


FIGURE 34. Pressure Distribution for Double Cone Run 1 as Predicted Using Five Species Air Model, Compared to Experimental Measurements.

The simulations for runs 2, 3, and 5 converge to steady solutions without any significant oscillations. Numerical Schlieren images of the predicted flowfields are compared in Figure 35. The predicted heat flux and pressure profiles for run 2 are presented in Figures 36 and 37, respectively, compared to experimental measurements. Separation is predicted to occur downstream of the point of flow separation observed in the experiment (2.95 inches vs. 2.56 inches). Except for the point of flow separation, the predicted pressure profile agrees quite well with the measurements. Similarly, the heat flux predictions follow the same trends as the experiment, but the values tend to be slightly under-predicted. The sharp drop in heat flux at an axial location of 3.95 inches is caused by a small, secondary separation bubble.

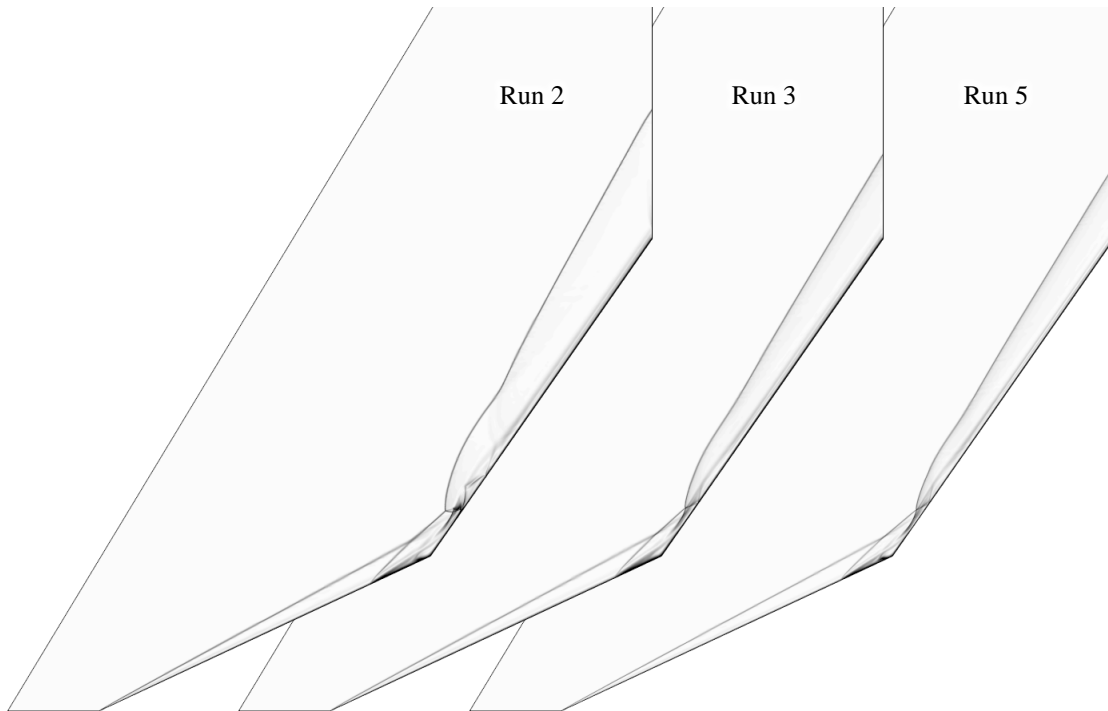


FIGURE 35. Numerical Schlieren Images of Flowfield Predicted for Double Cone Runs 2, 3, and 5.

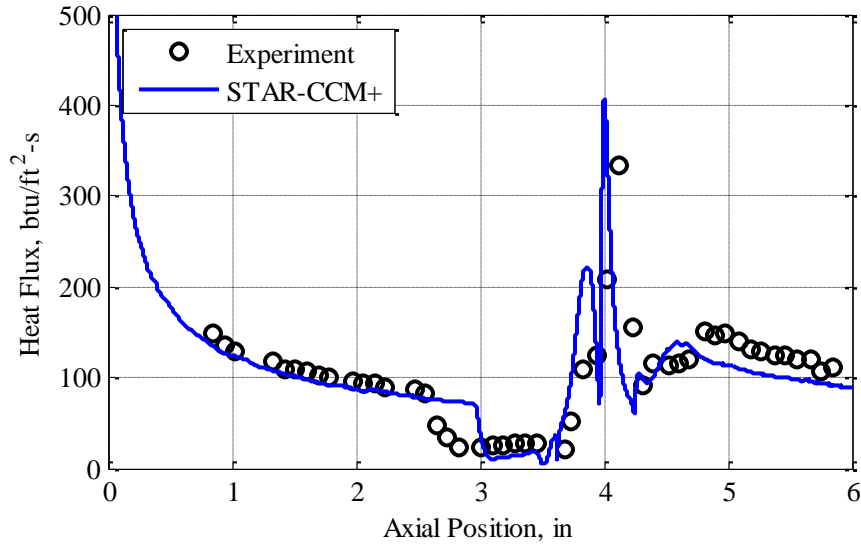


FIGURE 36. Heat Flux Distribution for Double Cone Run 2 as Predicted Using Five Species Air Model, Compared to Experimental Measurements.

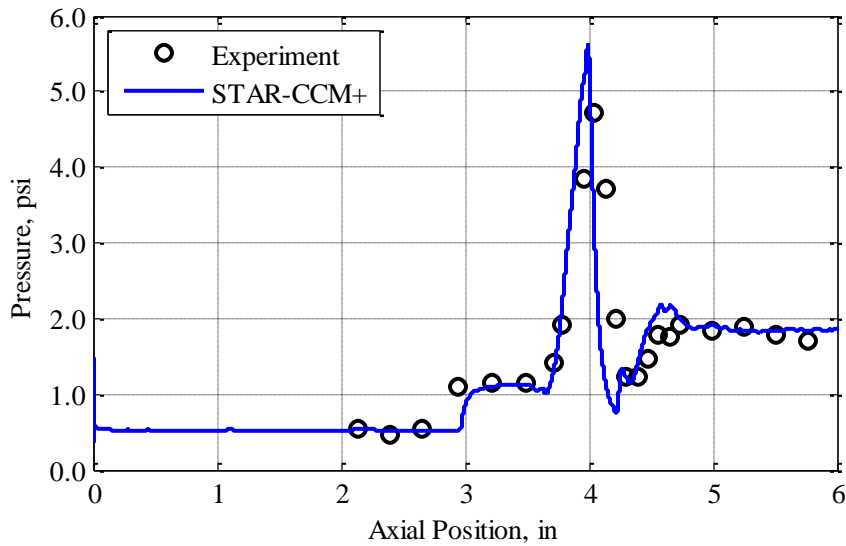


FIGURE 37. Pressure Distribution for Double Cone Run 2 as Predicted Using Five Species Air Model, Compared to Experimental Measurements.

Simulation results are compared to the experimental measurements for run 3 in Figures 38 and 39. There is excellent agreement between the simulation and the experiment, including the point of flow separation. The largest discrepancy observed is that the magnitude of the heat flux is somewhat under-predicted, especially upstream and far downstream of the separation bubble.

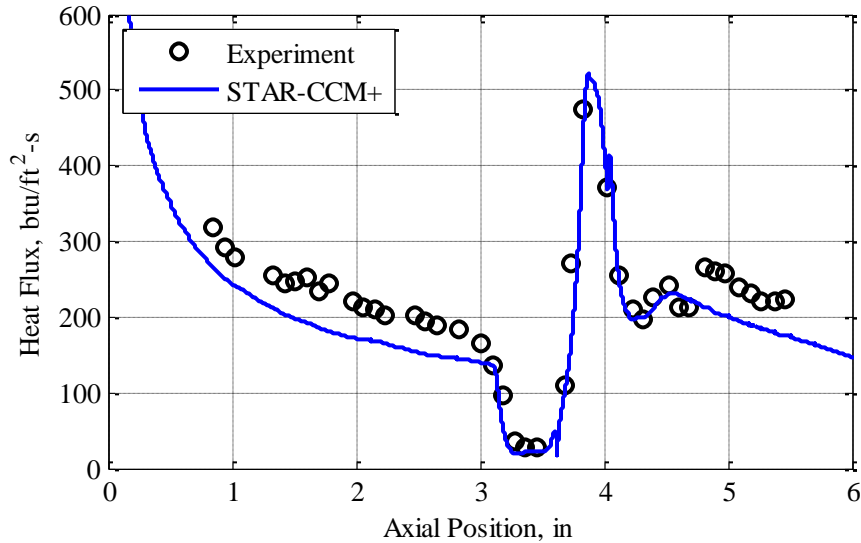


FIGURE 38. Heat Flux Distribution for Double Cone Run 3 as Predicted Using Five Species Air Model, Compared to Experimental Measurements.

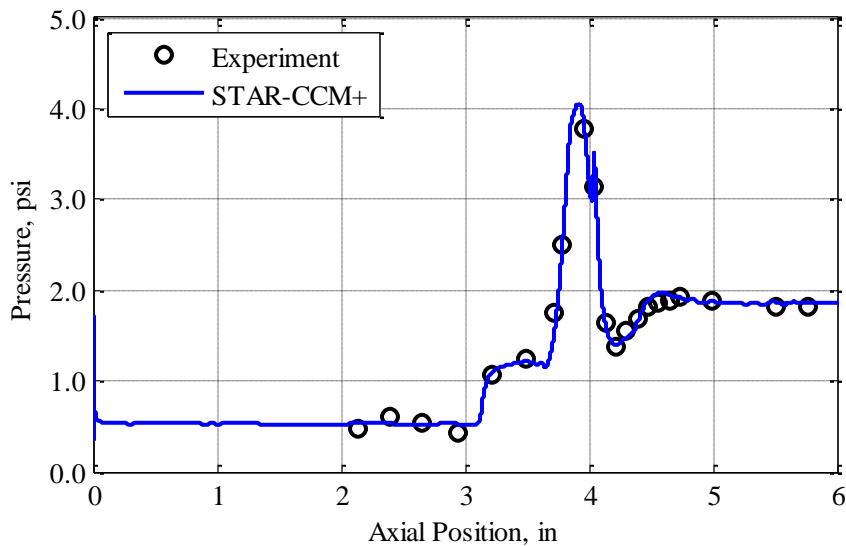


FIGURE 39. Pressure Distribution for Double Cone Run 3 as Predicted Using Five Species Air Model, Compared to Experimental Measurements.

Finally, comparisons are made for run 5 in Figures 40 and 41. With this simulation, it is observed that once again the point of flow separation is predicted to be downstream of the experimentally observed location (3.05 inches versus 2.75 inches). Except for this, the predicted pressure profile is in very good agreement with the experiment. The heat flux is observed to be fairly consistently under-predicted, though the predicted peak heat flux is somewhat higher than that observed experimentally. However, this is most likely related to the difference in the point of flow separation.

It is unclear why run 1 produces an oscillating solution, while the other runs are steady. The freestream temperature, velocity, density, and pressure are lower for this run than for the others (see Table 2); one or more of these parameters could be the cause. It is also unclear why the predicted point of separation agrees well with experiment for run 3, when the predicted separation point is downstream of the experimentally observed point of separation for the other runs. This could either be coincidental, or else related to the lower Reynolds number for run 3.

The temperature field for both energy modes in the vicinity of the 25-/55-degree double cone junction as predicted for run 3 is visualized in Figure 42. Due to the very high freestream Mach number (13.2), extremely high temperatures are produced behind the shocks, along with significant thermodynamic nonequilibrium. Maximum temperature of the translational-rotational energy mode peaks at just over 30,000 °R (16,667 K) immediately behind the shock over the second cone, then decreases due to relaxation of the vibrational-electronic energy mode. Maximum temperature of the vibrational-electronic mode is about 11,000 °R (6,111 K) and occurs farther downstream of the shock. Computed mass fractions for the five constituent species are compared in Figure 43. Note that the three minor species (NO, N, and O) use the same color bar scaling, while different scaling is used for both N₂ and O₂. These images show that a significant amount of chemistry is occurring downstream of the shocks. Most of this chemistry occurs in the flow stream that is processed by the single, strong shock over the second cone. The flow stream lying closest to the second cone, which is processed by multiple shocks (the shock over the first cone, followed by the separation shock) appears to be less reactive. This is due to the reduced temperature in this flow stream (multiple shocks are more efficient than a single, stronger shock). As expected, O₂ is observed to be more reactive than N₂. Up to 90% of O₂ is observed to dissociate, while maximum dissociation of N₂ is only about 30%. These comparisons demonstrate the significance of thermodynamic and chemical nonequilibrium phenomena for high Mach flows.

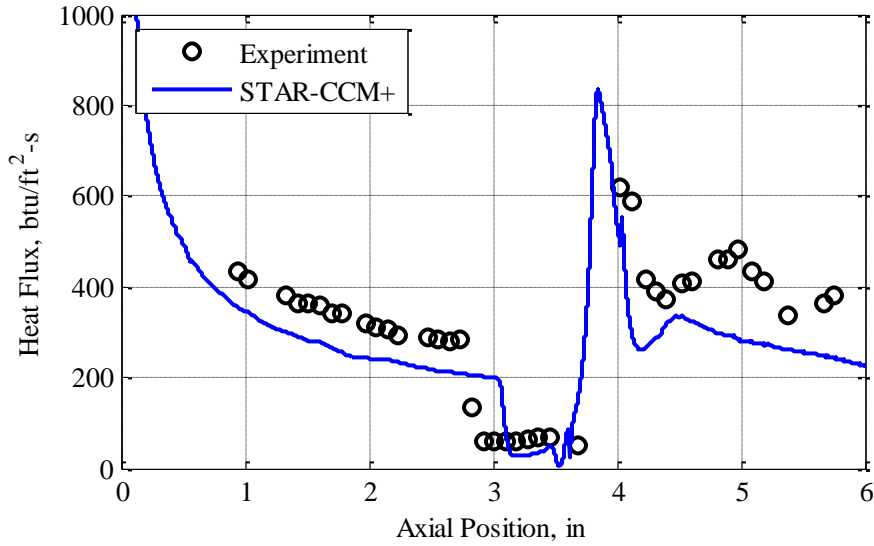


FIGURE 40. Heat Flux Distribution for Double Cone Run 5 as Predicted Using Five Species Air Model, Compared to Experimental Measurements.

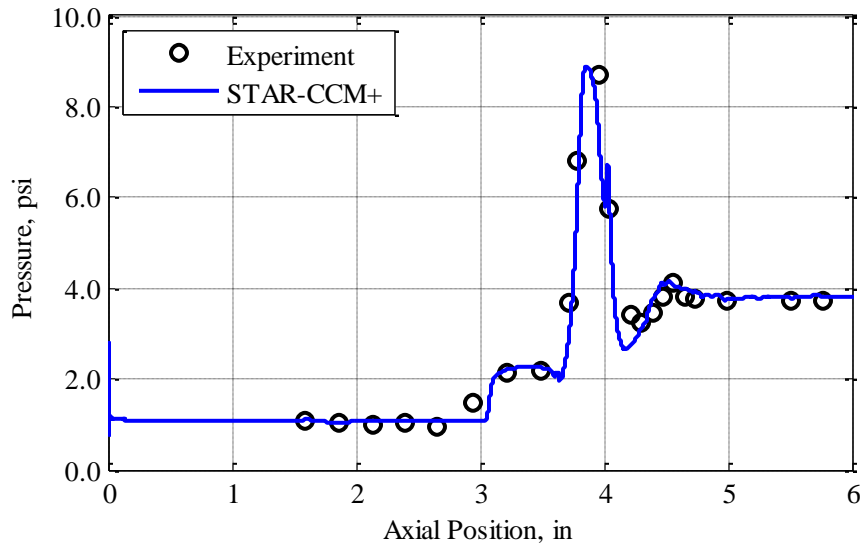


FIGURE 41. Pressure Distribution for Double Cone Run 5 as Predicted Using Five Species Air Model, Compared to Experimental Measurements.

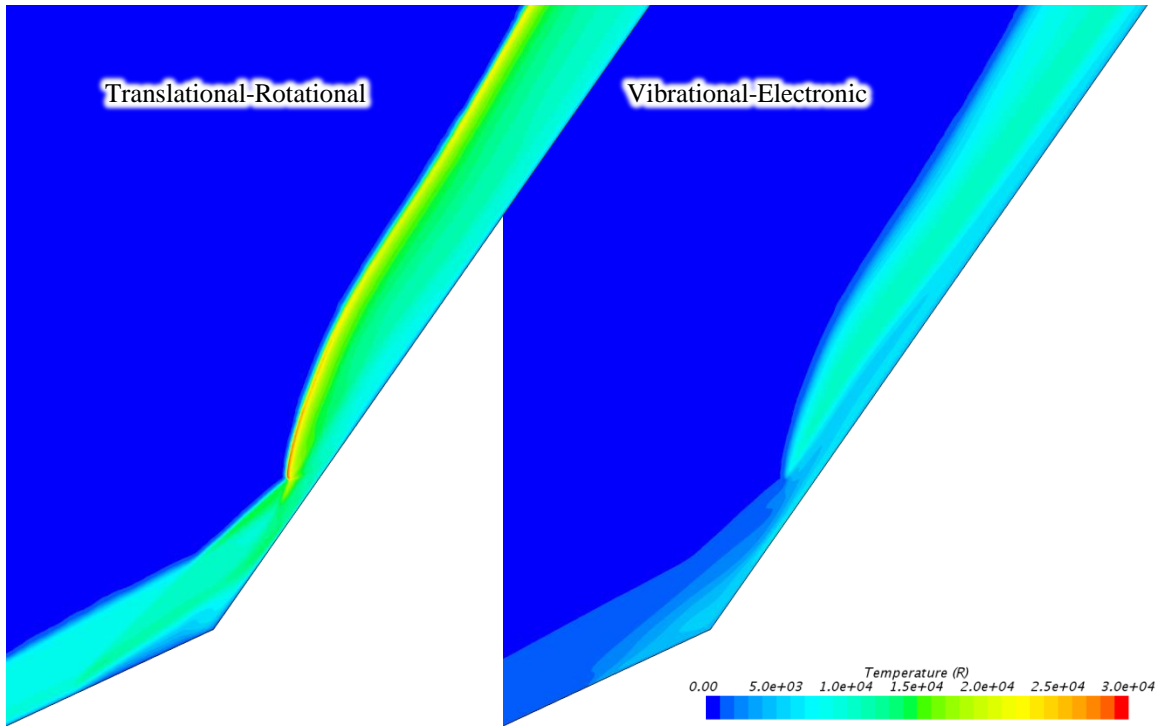


FIGURE 42. Temperature of Two Energy Modes, as Predicted for Double Cone Run 3.

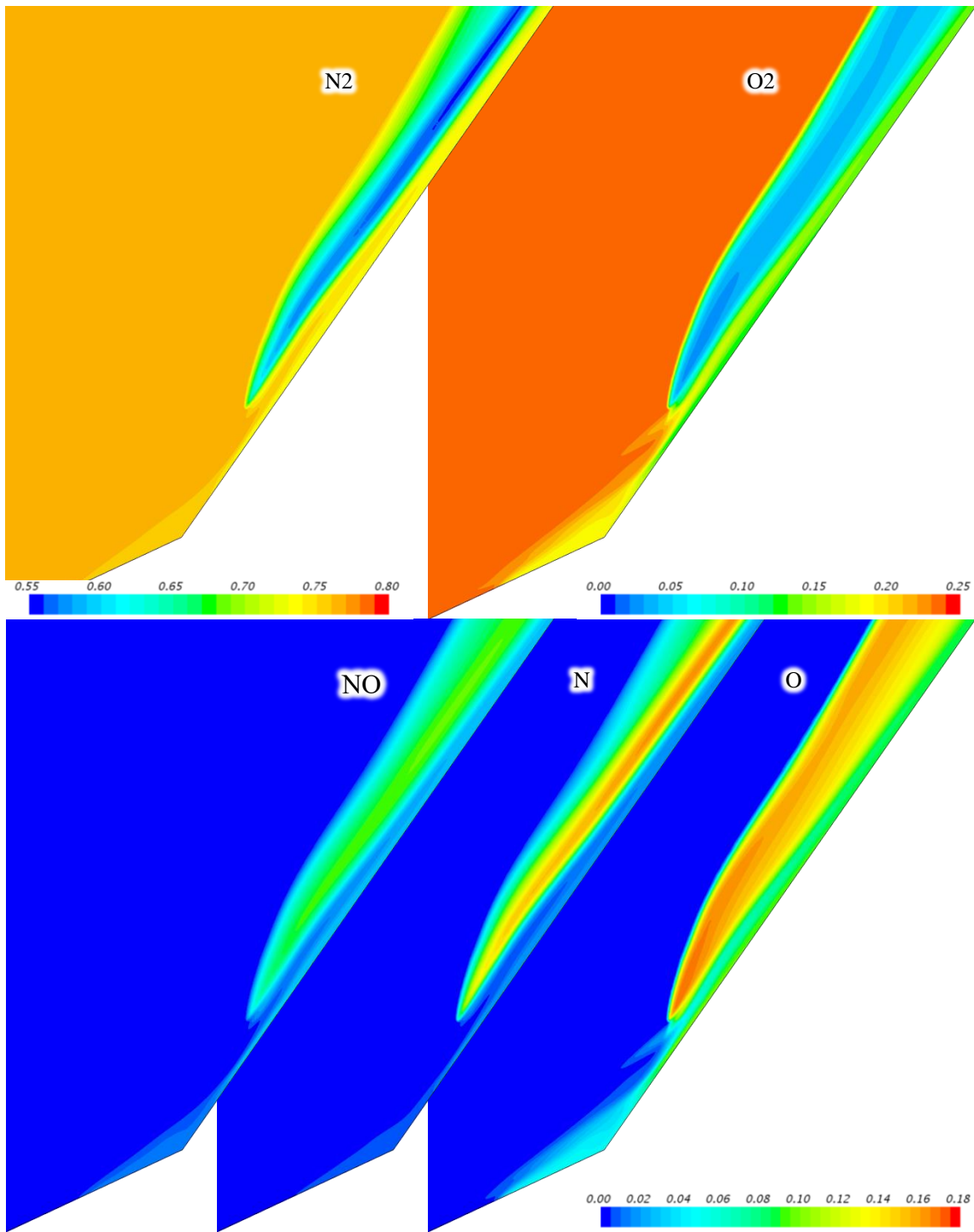


FIGURE 43. Species Mass Fractions, as Predicted for Double Cone Run 3.

These test cases have also been simulated by other analysts using research-level CFD codes. Unfortunately, their results are only available graphically (Reference 11), which hinders direct comparisons to the solutions obtained in the current work. However, the results obtained in this work are, in general, quite comparable to the simulation results presented in Reference 11. The location of flow separation predicted in this current effort agrees with the experimental measurements equally well or better than the predictions made in Reference 11 by other analysts. For run 3, the current work predicts flow separation substantially better than the previous analyses. The secondary separation bubble observed for run 2 in this work was also encountered by the earlier simulations. The largest discrepancy between this present work and the previous simulations is that the magnitude of the heat flux for the present simulations can be somewhat smaller than that predicted by the earlier simulations. This is probably worthy of further investigation.

One simulation completed, but not presented, for run 1 used the two species air model. By comparing the times required to complete this simulation and the five species simulation, it is possible to estimate the relative cost of the two air models. These simulations are performed using one cluster node consisting of two 2.6 GHz Intel Xeon E5-2690v4 processors (28 cores total). The two species simulation requires $6.77\text{E-}5$ CPU-seconds per iteration per cell, while the five species simulation needs $1.64\text{E-}4$ CPU-seconds per iteration per core. Thus, for this case, the five species model is approximately 2.4 times as costly as the two species simulation.

4.2 SMALL CYLINDER-FLARE

The laminar small cylinder-flare geometry was not considered in the FY14 work, but it is investigated as part of the FY18 effort. All five experimental runs from the latest test campaign are simulated; freestream conditions are given in Table 3. All simulations use the recommended solver settings (discussed in Section 3.2) and the five species air model, which accounts for thermodynamic nonequilibrium and dissociation reactions. Convergence of these simulations is determined primarily by monitoring the location of flow separation. All simulations are observed to converge to steady solutions, without any significant oscillations.

The mesh is refined four times (except for run 3, which is refined five times) using the normalized pressure gradient technique (except for run 1, which used the initial pressure gradient technique). The prism mesh is sized through the use of preliminary, turbulent simulations such that wall Y^+ remains below 0.7. Using run 5 as an example, the original mesh contains about 29 thousand cells, while subsequently refined meshes contain approximately 23, 38, 72, and 158 thousand cells, respectively. Due to mesh coarsening in the freestream, the first refined mesh actually contains fewer cells than the original mesh. Images of the sequence of meshes used for run 3 are shown in Figure 11.

Numerical Schlieren images illustrating the predicted flowfields are compared in Figure 44. Separation of the flow in these test cases is found to be relatively sensitive to the mesh used. The flow separation point as predicted using the initial and final meshes is compared in Table 9; as the mesh is refined, the flow separation point is observed to move forward by up to a few inches. Also, shown in Table 9 is the change in flow separation position between the penultimate and final meshes (the “final change”). The separation point has essentially stopped moving for runs 2, 3, and 5, indicating that a mesh-converged solution is obtained. Larger motion of the separation point is still being predicted for runs 1 and 4, suggesting that these solutions may not be fully mesh-converged. The very small separation bubble predicted for run 2 is consistent with the attached flow observed in the experiment. For the other runs, the predicted separation point occurs significantly upstream (by up to about 0.8 inch) of the measured point of flow separation.

The predicted heat flux and pressure distributions for these simulations are compared to experimental measurements in Figures 45 through 54. All five runs present similar trends. Heat flux and pressure upstream and within the separation bubble agree reasonably well with the experiment, with the heat flux usually being slightly under-predicted. The peak pressure and heat flux on the flare are always over-predicted in magnitude, but the location of the peaks is reasonably close. These peaks are immediately followed by a region on the flare where the pressure and heat flux are significantly under-predicted. Towards the aft end of the flare the predictions approach the measured values.

These laminar cylinder-flare test cases have also been previously simulated by a number of other researchers using a variety of research CFD codes (Reference 11). Due to the graphical presentation of their results, it is not possible to make direct comparisons with the present work. However, the simulations produced in this effort are very consistent with the previous work. There is some variability in the point of flow separation predicted by the different CFD codes in the earlier effort, but in all cases, the predicted point of flow separation occurs upstream of the experimentally observed flow separation point. The flow separation points predicted in this current work fall in line with the previous predictions. The heat flux and pressure distributions predicted from the earlier analyses also show the exact same trends and shapes as those produced in this effort.

TABLE 9. Flow Separation Position, in Inches, for Small Cylinder-Flare Test Cases.

Run	Initial Mesh	Final Mesh	Final Change	Experiment	Difference
1	3.92	3.26	-0.197	3.7	-0.44
2	3.99	3.96	0.006	4.0	-0.04
3	3.85	1.81	-0.088	2.6	-0.79
4	3.76	2.00	-0.222	2.5	-0.50
5	3.92	2.87	-0.066	3.7	-0.83

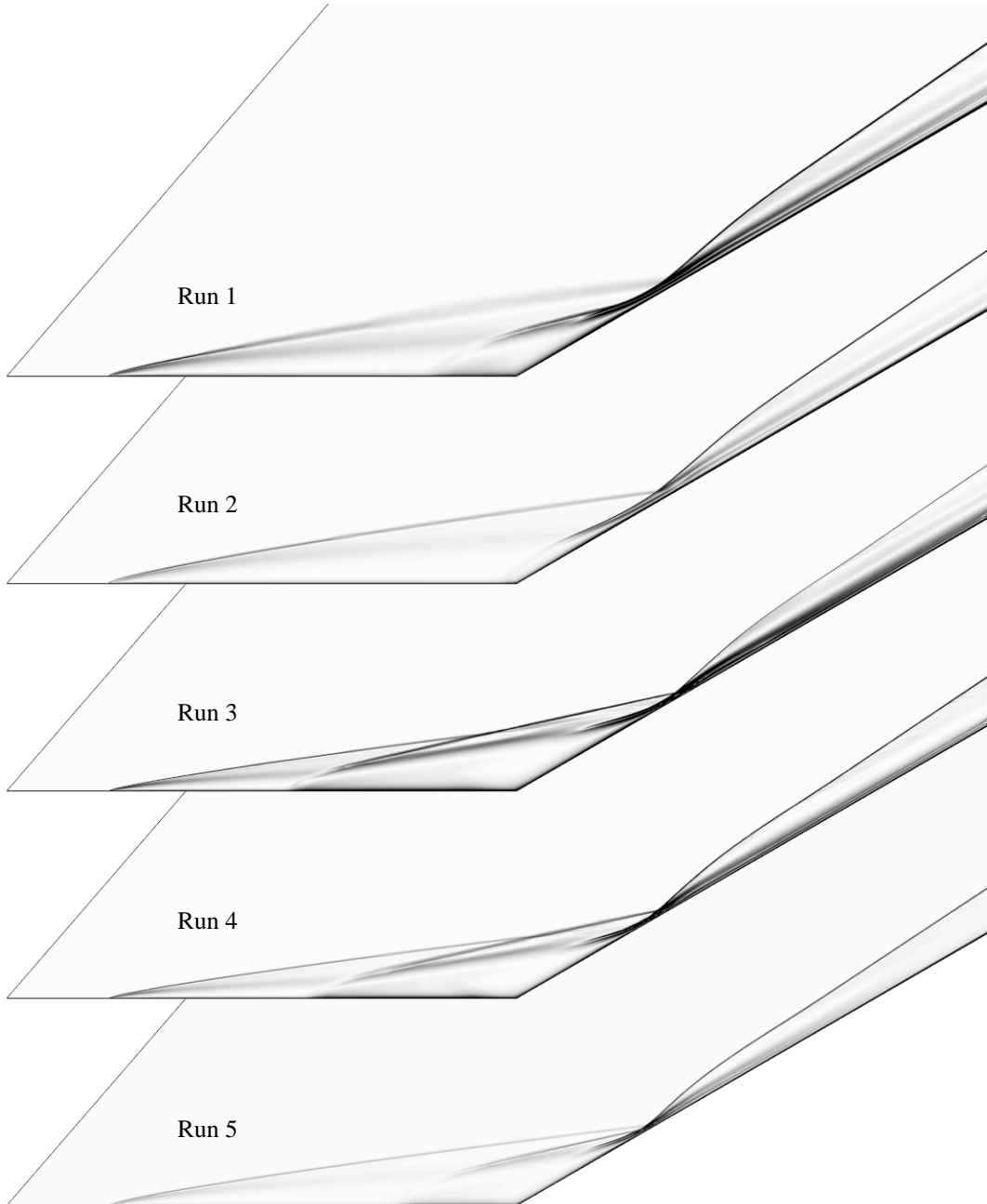


FIGURE 44. Numerical Schlieren Images of Flowfield Predicted for Small Cylinder-Flare Test Cases.

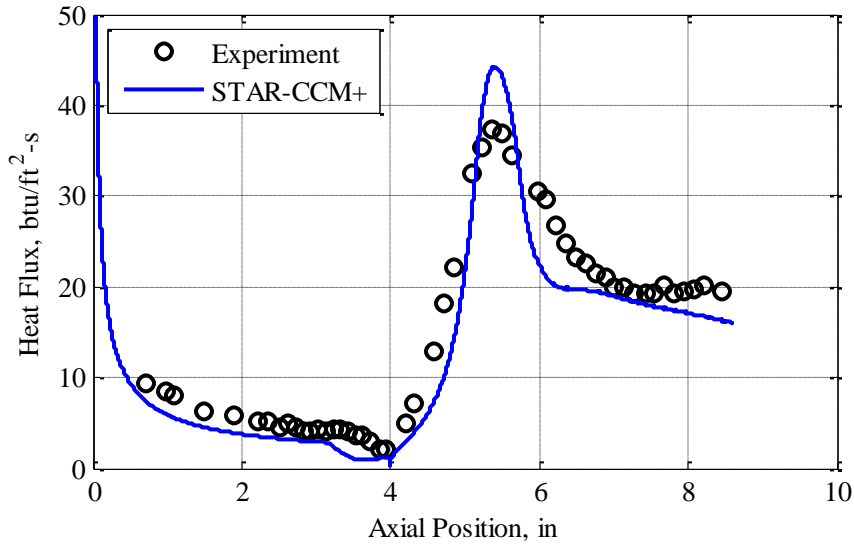


FIGURE 45. Heat Flux Distribution for Small Cylinder-Flare Run 1 as Predicted Using Five Species Air Model, Compared to Experimental Measurements.

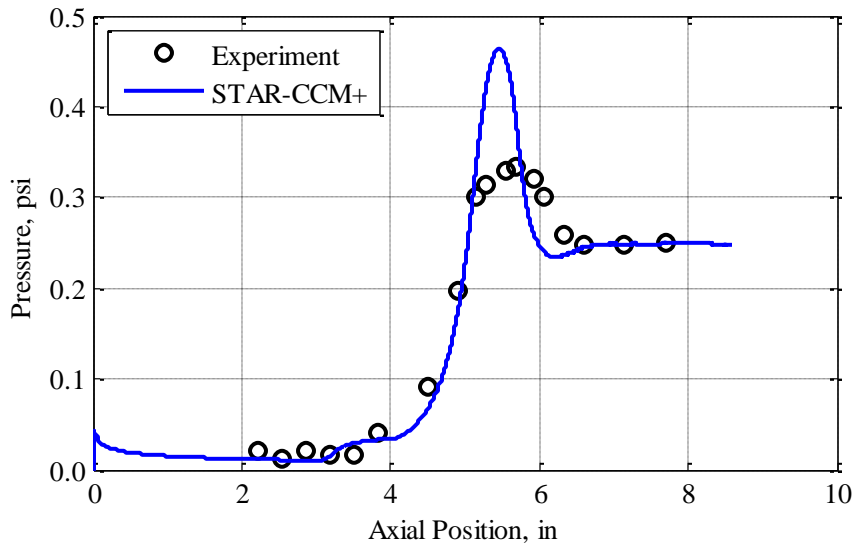


FIGURE 46. Pressure Distribution for Small Cylinder-Flare Run 1 as Predicted Using Five Species Air Model, Compared to Experimental Measurements.

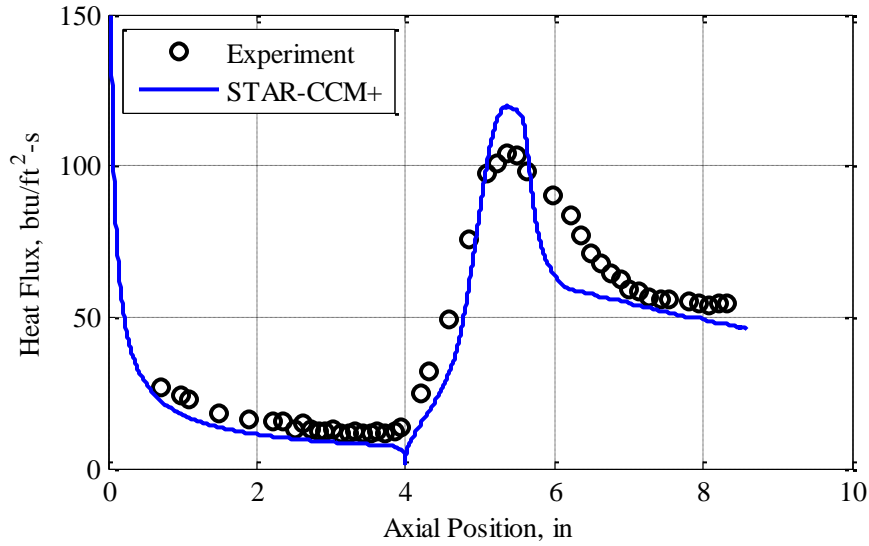


FIGURE 47. Heat Flux Distribution for Small Cylinder-Flare Run 2 as Predicted Using Five Species Air Model, Compared to Experimental Measurements.

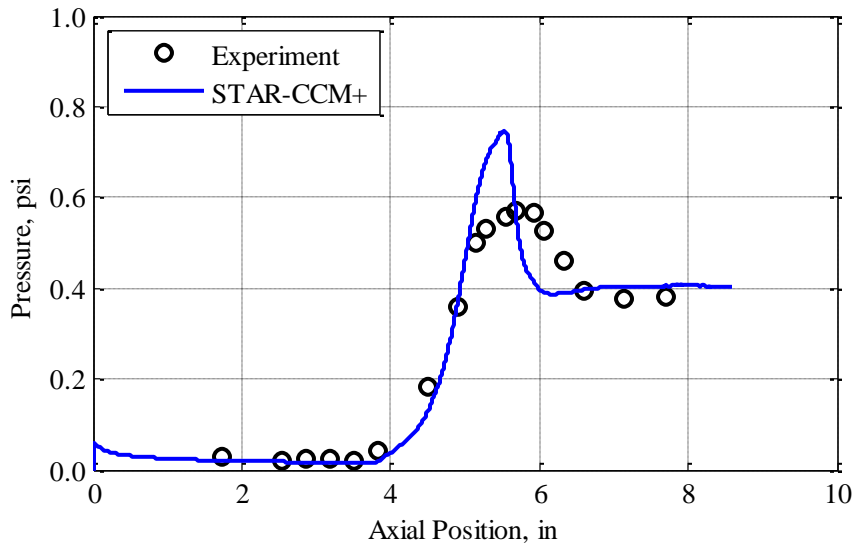


FIGURE 48. Pressure Distribution for Small Cylinder-Flare Run 2 as Predicted Using Five Species Air Model, Compared to Experimental Measurements.

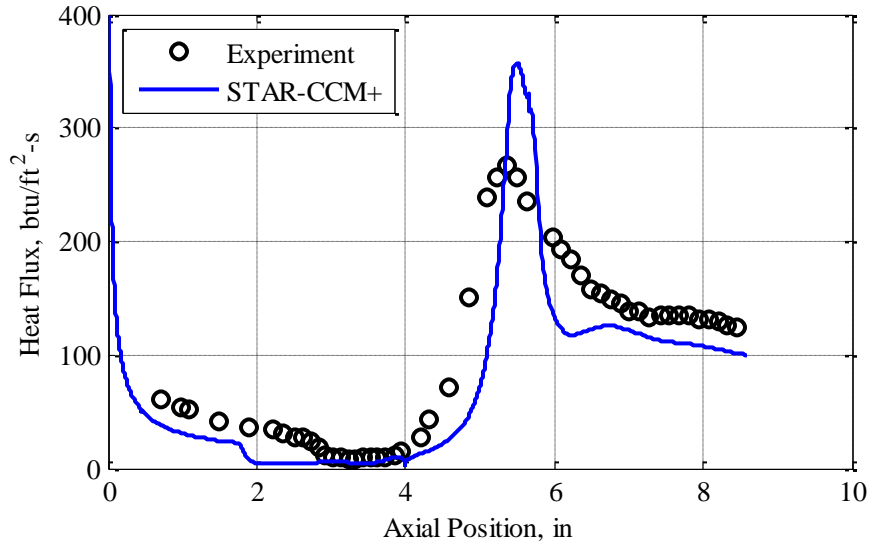


FIGURE 49. Heat Flux Distribution for Small Cylinder-Flare Run 3 as Predicted Using Five Species Air Model, Compared to Experimental Measurements.

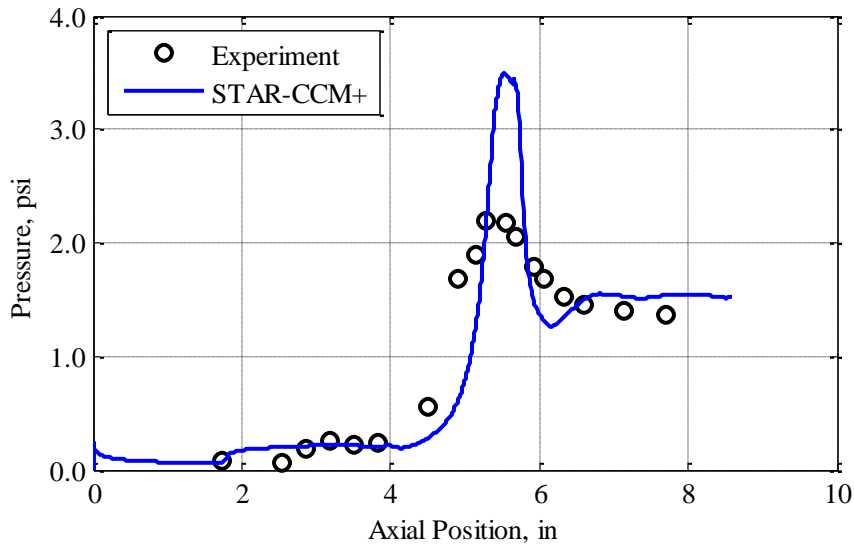


FIGURE 50. Pressure Distribution for Small Cylinder-Flare Run 3 as Predicted Using Five Species Air Model, Compared to Experimental Measurements.

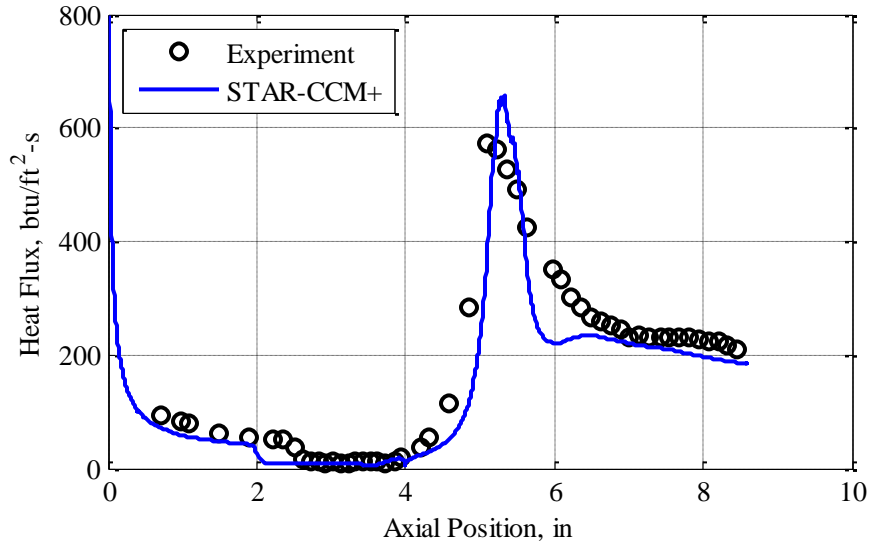


FIGURE 51. Heat Flux Distribution for Small Cylinder-Flare Run 4 as Predicted Using Five Species Air Model, Compared to Experimental Measurements.

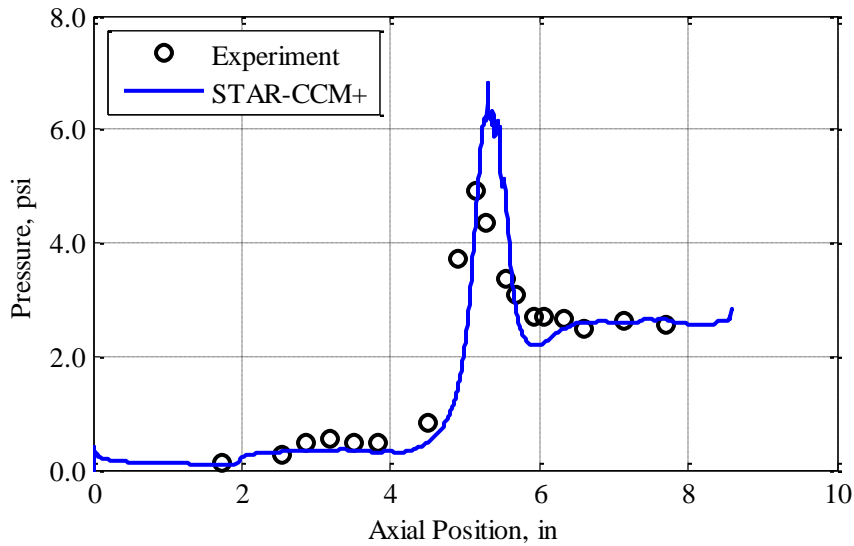


FIGURE 52. Pressure Distribution for Small Cylinder-Flare Run 4 as Predicted Using Five Species Air Model, Compared to Experimental Measurements.

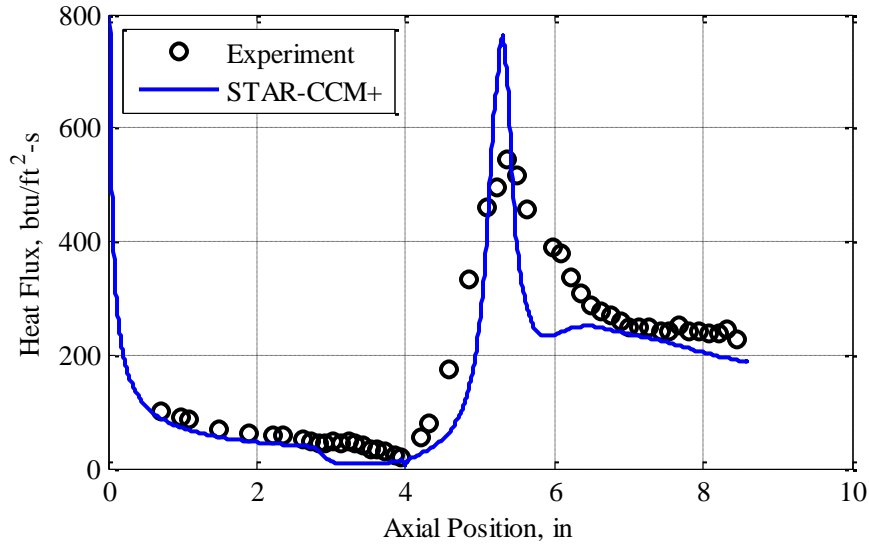


FIGURE 53. Heat Flux Distribution for Small Cylinder-Flare Run 5 as Predicted Using Five Species Air Model, Compared to Experimental Measurements.

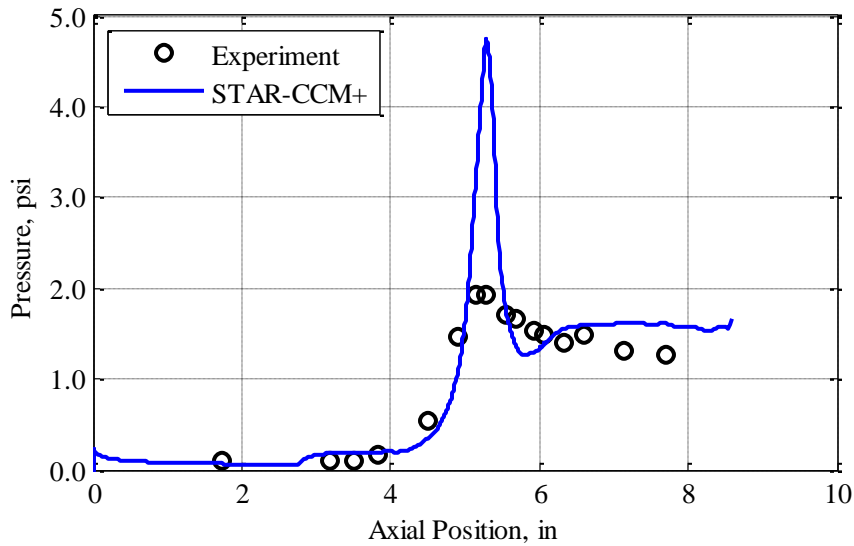


FIGURE 54. Pressure Distribution for Small Cylinder-Flare Run 5 as Predicted Using Five Species Air Model, Compared to Experimental Measurements.

4.3 CONE-FLARE

The cone-flare test case (run 4) is the second case investigated in the FY14 effort. Unlike the previously discussed test cases, which featured laminar boundary layers, the cone-flare test case produces turbulent boundary layers. Four turbulence models, with default settings, are investigated in the FY14 work. This test run is revisited in the FY18 effort, which conducts a more thorough investigation of all Reynolds-Averaged Navier-Stokes (RANS) turbulence models included in STAR-CCM+, as well as the effects of non-default turbulence model options. Additional test runs, not available at the time of the FY14 effort, are simulated as part of the FY18 work.

4.3.1 FY14 Effort

During the FY14 effort, simulations are performed for the 6-/42-degree cone-flare (experiment run number 4) investigating four different turbulence models:

- Menter SST model
- Wilcox $k-\omega$ model
- Spalart-Allmaras model
- Two-Layer Realizable $k-\epsilon$ model

Default values are used for all turbulence model options. The gas is modeled using the equilibrium air model included in STAR-CCM+. The AUSM+ flux method is employed, and the CFL number is set to 1.0. These simulations are initialized to freestream conditions (impulsive start). Attempting initialization by ramping the freestream Mach number produces very severe flow separation and leads to floating point errors. Using the grid sequencing initialization feature is also found to lead to failures in the turbulence model very early in the simulation. A structured directed mesh is used for these simulations, constructed in a manner similar to the meshes used for the double cone simulations. The geometry of the flow domain is presented in Figure 4.

The heat flux distributions predicted by the simulations using the four different turbulence models are compared to experimental measurements in Figure 55. Heat flux is presented nondimensionally as Stanton number, defined as

$$St = \frac{\dot{q}''}{\rho_{\infty} U_{\infty} (h_0 - h_w)} \quad (16)$$

where \dot{q}'' is the heat flux, ρ_{∞} is the freestream density, U_{∞} is the freestream velocity, h_0 is the total enthalpy of the freestream, and h_w is the enthalpy of the flow at the wall. Pressure distribution comparisons are made in Figure 56; pressure is presented normalized by the freestream dynamic pressure (q_{∞})

$$\frac{P}{q_{\infty}} = \frac{P}{\frac{1}{2} \rho_{\infty} U_{\infty}^2} \quad (17)$$

From these plots, it is observed that the Menter SST and the Wilcox k- ω turbulence models predict extremely large separation bubbles. As a result, agreement with the experimental measurements is quite poor for these models. These separation bubbles are very slow growing; it takes over 200,000 iterations for the separation bubble to reach its final size for the Menter SST simulation. At the point that the Wilcox k- ω simulation was terminated, the separation bubble was still growing and had not yet reached a final size. The two-layer realizable k- ϵ model predicts a separation bubble that is somewhat larger than that measured experimentally. The size of this separation bubble is observed to be stable and not growing. The Spalart-Allmaras turbulence model predicts attached flow.

All simulations predict the pressure on the cone upstream of the separation well, as would be expected. Both the Spalart-Allmaras and the k- ϵ models yield good agreement with the experiment for the pressures on the flare downstream of the flow reattachment. However, this agreement is not so good at the extreme aft end of the flare. The k- ϵ model does a fair job of capturing the pressure in the separation bubble. Heat flux predictions upstream of the flow separation agree well with the experiment for all turbulence models considered. The Spalart-Allmaras turbulence predicts heat transfer with exceptionally good agreement on the flare. The k- ϵ model predicts the correct trend to heat flux on the flare but over-predicts the magnitude slightly. There is also a spike in heat flux predicted at the attachment point that is not present in the experimental data. This turbulence model does a very poor job of predicting heat transfer within the separation bubble.

Images comparing the predicted Mach number distribution over the entire flow domain are given in Figure 57. A more detailed view of the flowfield in the vicinity of the cone/flare junction is provided in Figure 58.

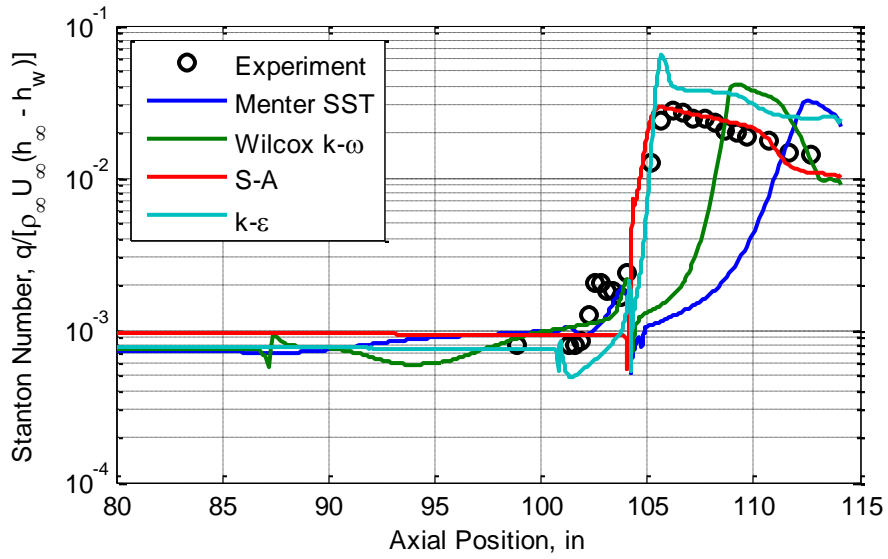


FIGURE 55. Stanton Number as Predicted by Cone-Flare Run 4 Simulations Employing Four Different Turbulence Models, Compared to Experimental Measurements.

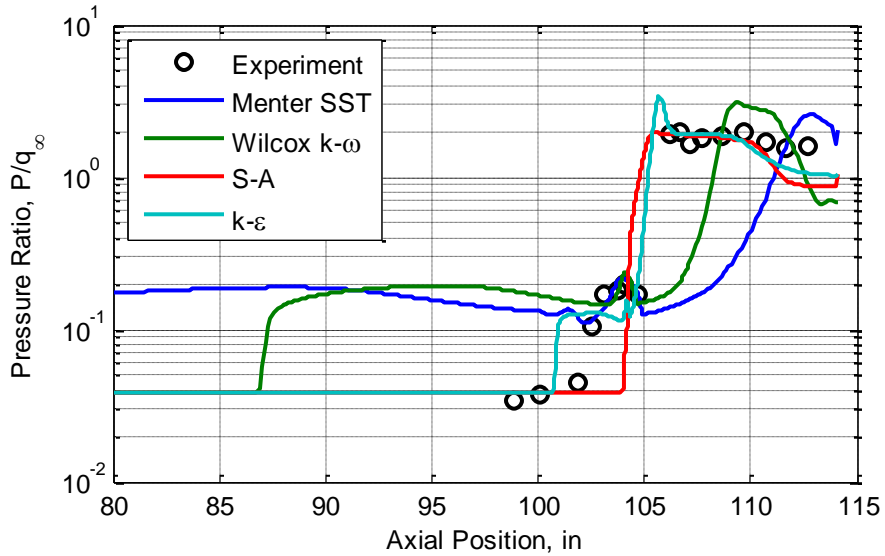


FIGURE 56. Pressure Ratio as Predicted by Cone-Flare Run 4 Simulations Employing Four Different Turbulence Models, Compared to Experimental Measurements.

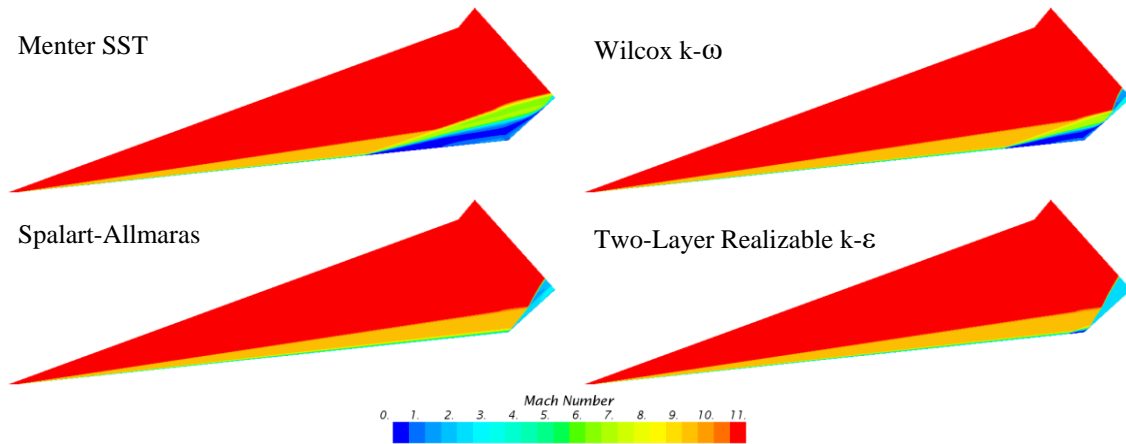


FIGURE 57. Comparison of Mach Number Distributions as Predicted by Cone-Flare Run 4 Simulations Employing Four Different Turbulence Models.

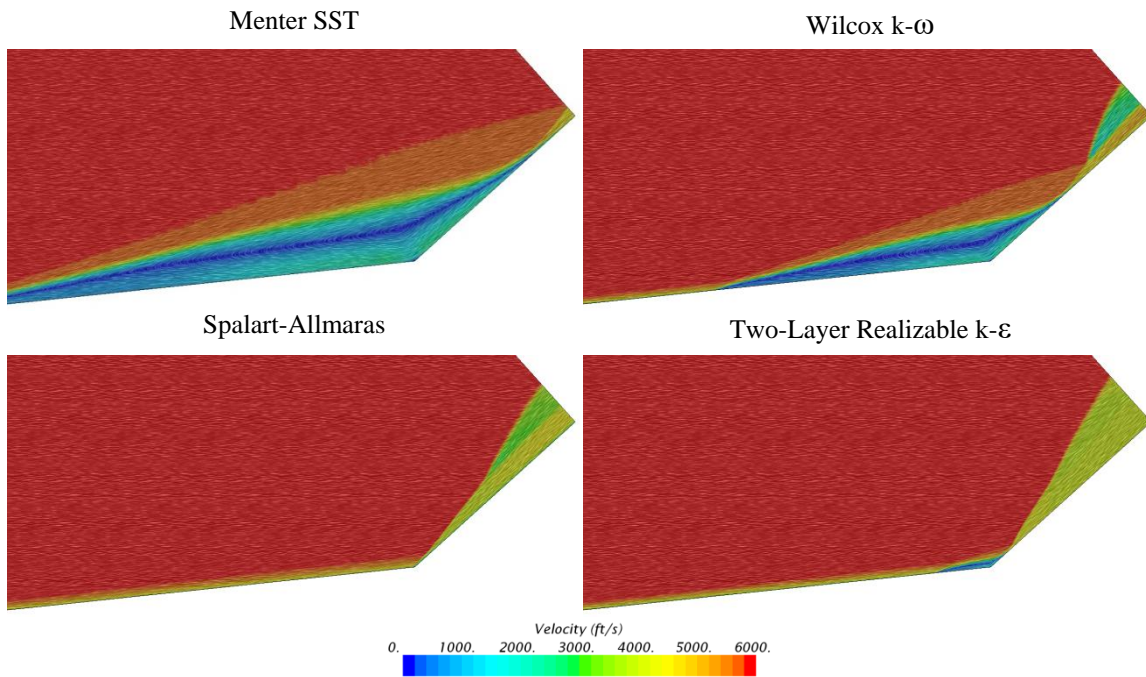


FIGURE 58. Comparison of Velocity Field in Vicinity of Cone-Flare Junction as Predicted by Cone-Flare Run 4 Simulations Employing Four Different Turbulence Models.

4.3.2 FY18 Effort

The 6-/42-degree cone-flare (experiment run number 4) test case is revisited in the FY18 effort to explore additional turbulence models and various turbulence model options. Simulations in this first study use the one species high-temperature air model and associated solver settings discussed in Section 3.0. This study is summarized in Table 10. All turbulence models selected provide a solve-to-the-wall capability; turbulence models that require the use of wall functions are not considered. Except as indicated in Table 10, default turbulence model settings are used. Most turbulence models do not provide adjustable settings suitable for investigation, the one exception being the Menter SST model, which has a number of different settings that are explored in this study. For several simulations, the mesh is refined based on the normalized pressure gradient using the technique discussed in Section 3.5.3. The number of mesh refinements is indicated in Table 10; “0” indicates the use of the original, unrefined mesh. This original mesh contains 56,342 cells and produces wall Y^+ values of approximately 0.15 on the cone and 0.25 on the flare. The first refined mesh contains nominally 60 thousand cells; the second refinement 98 thousand, and the third refinement approximately 175 thousand cells. In many simulations the predicted separation point is far forward of the experimentally observed separation point of 102 inches; in these cases, further mesh refinement is not pursued. For all simulations in this study, the point of flow separation (based on zero wall shear stress) is monitored and is observed to converge to a final, steady value. Separation bubbles that grow without bound, such as those observed in the FY14 effort, are not encountered in the FY18 simulations.

The Spalart-Allmaras predicts a very small separation bubble (note that the cone-flare junction is located at the 104.2-inch axial station), the size of which is unaffected by mesh refinement. This is consistent with the FY14 effort (where the assessment of no separation is based on the pressure and heat flux distributions and not the more accurate method used here).

The realizable two-layer $k-\epsilon$ model predicts separation far forward of the point observed in the experiment or predicted by the FY14 simulation. Additionally, the point of flow separation shifts several inches forward after the first mesh refinement. This shows that there is significant sensitivity to the mesh used for the analysis. This may explain some of the differences between the FY14 and FY18 simulations using this turbulence model. Turning off the continuity convergence accelerator feature does not appear to have a strong impact on the results (as is expected).

TABLE 10. Summary of 6-/42-Degree Cone-Flare Turbulence Model Investigation.

Turbulence Model	Model Settings	Mesh Refinement	Separation, inches
Spalart-Allmaras	Default	0	104.0
Spalart-Allmaras	Default	1	104.0
Spalart-Allmaras	Default	2	104.0
Spalart-Allmaras	Default	3	104.0
Realizable Two-Layer k- ϵ	Default	0	87.6
Realizable Two-Layer k- ϵ	Default	1	79.1
Realizable Two-Layer k- ϵ	CCA off	0	87.2
V2F k- ϵ	Default	0	66.5
Elliptic Blending k- ϵ	Default	0	76.4
Lag Elliptic Blending k- ϵ	Default	0	99.4
Lag Elliptic Blending k- ϵ	Default	1	93.2
LPS Two-Layer RST	Default	0	100.3
LPS Two-Layer RST	Default	1	96.3
Elliptic Blending RST	Default	0	71.6
Menter SST	Default	0	72.6
Menter SST	QCR on	0	74.1
Menter SST	Normal stress term on	0	68.1
Menter SST	Compressibility off	0	100.4
Menter SST	Compressibility off	1	99.0
Menter SST	Compressibility off	2	98.3
Menter SST	Compressibility off	3	98.3
Menter SST	QCR on Compressibility off $a_1 = 0.355$	0	101.8
Menter SST	QCR on Compressibility off $a_1 = 0.355$	1	101.0
Menter SST	QCR on Compressibility off $a_1 = 0.355$	2	100.4
Menter SST	QCR on Compressibility off $a_1 = 0.355$	3	100.4
Menter SST	QCR on $a_1 = 0.355$	0	82.8

The V2F k- ϵ model solves two additional equations (one for a wall-normal stress component and the other for a relaxation parameter) that are supposed to provide more accurate predictions of heat transfer, skin friction, and flow separation. However, this model actually predicts separation of the flow very far forward on the cone. Similarly, the elliptic blending k- ϵ model solves a total of four equations and is supposed to be an improvement over the realizable two-layer k- ϵ model. However, it actually predicts a rather large separation bubble. The improved lag elliptic blending k- ϵ model is supposed to provide a good predictive capability for separated flow. It does predict the smallest separation bubble of all the k- ϵ models, but separation still occurs far forward of the experimental separation point and is sensitive to mesh refinement.

The linear pressure strain (LPS) Reynolds stress transport (RST) model does not use an eddy viscosity assumption but instead directly computes the Reynolds stresses. It predicts flow separation to occur at a point relatively far aft (but still forward of that observed experimentally), but this is sensitive to the mesh. The elliptic blending RST model variant predicts separation to occur far forward on the cone.

Using default options, the Menter SST turbulence model predicts a stable separation bubble relatively far forward on the cone. This is a notable difference from the FY14 effort, where the separation bubble was observed to grow without bound. The cause for this difference in behavior is unknown. When activated, the quadratic constitutive relation (QCR) option is supposed to account for the anisotropy of the turbulence and improve predictions of flows with recirculation (the default is a linear constitutive relation). However, this provides only a marginal improvement. Activating the normal stress term option directly solves certain terms in the Boussinesq approximation that are otherwise neglected. With this option active, the flow separation point shifts forward several inches, worsening the agreement with the experiment. Deactivating the compressibility correction (which is on by default) seems to have the largest impact on the solution. With the compressibility option deactivated, separation occurs at a location relatively far aft on the cone. There is still some sensitivity to the mesh, but this is much less than what is observed with the other turbulence models, and it appears that a mesh-converged solution could be obtained after three mesh refinements.

The smallest separation bubble predicted by the Menter SST model is obtained with the combination of three non-default options: activating the quadratic constitutive relation option, deactivating the compressibility correction, and changing the a_1 model coefficient value to 0.355 (default value is 0.31). This updated coefficient value is recommended by the developers of STAR-CCM+ for shock-separated flows, based on Reference 24. While there is still some mesh sensitivity, with these options it is possible to obtain a mesh-converged solution with a separation bubble only a couple of inches larger than that observed experimentally. It is therefore recommended that these three options always be set when using the Menter SST turbulence model in STAR-CCM+ to simulate hypersonic flows with potential separation. (Unless otherwise indicated, all FY18 Menter SST simulations reported in this document set these three recommended non-default options.) When the compressibility correction is reactivated, the separation point shifts

forward by almost 18 inches. This reinforces that the compressibility correction should be deactivated for flows where separation is expected.

Stanton number (heat transfer) and pressure ratio distributions for the 6-/42-degree cone-flare run 4 test case, as computed by the Menter SST and Spalart-Allmaras (S-A) turbulence models, are compared to experimental measurements in Figures 59 and 60, respectively. An additional simulation employing the Spalart-Allmaras turbulence model and the five species reacting gas model with thermodynamic nonequilibrium is also included in this comparison. The choice of gas model appears to have negligible impact on the predictions for this test case. (It should be noted that nonphysical transient features are occasionally and randomly produced in the vibrational-electronic temperature solution. These nonphysical features appear to be related to the low freestream temperatures for this case.) The Spalart-Allmaras model under-predicts heat flux on the flare, while the Menter SST model provides good agreement with the experimental data. It is unclear why the heat flux is being under-predicted in the FY18 Spalart-Allmaras simulation, when good agreement was obtained in the FY14 effort (see Figure 55). Both turbulence models appear to predict the pressure distribution on the flare reasonably well. The predicted flowfields for these three simulations are compared in FIGURE 61. The flare shock is deflected slightly outwards for the five species simulation from its location in the single species simulation.

Computational cost information is extracted for the Spalart-Allmaras simulations for run 4 using the one and five species air models. When running on the cluster previously described, $1.63\text{E-}5$ CPU-seconds per iteration per cell are required for the one species model, and $9.88\text{E-}5$ CPU-seconds per iteration per cell are needed for the five species simulation. Thus, the five species model appears to be about six times more costly than the one species model, for this test case.

Select experiments (test runs 33 and 45) for the 7-/40-degree cone-flare geometry are also simulated (freestream conditions are given in Table 4), using both the Menter SST and the Spalart-Allmaras turbulence models. Simulations for run 33 are only performed using the single-species air model. Due to the low temperatures experienced for this run (maximum temperature is less than 500 K), the two species and five species gas models are not expected to provide any significant changes to the predictions. Simulations for run 45 are performed using the one and two species (with thermal nonequilibrium) gas models. The mesh used in these simulations is refined three or four times based on the normalized pressure gradient technique discussed in Section 3.5.3. The initial mesh has approximately 40 thousand cells, while the increasingly refined meshes have nominally 52, 82, 140, and 250 thousand cells.

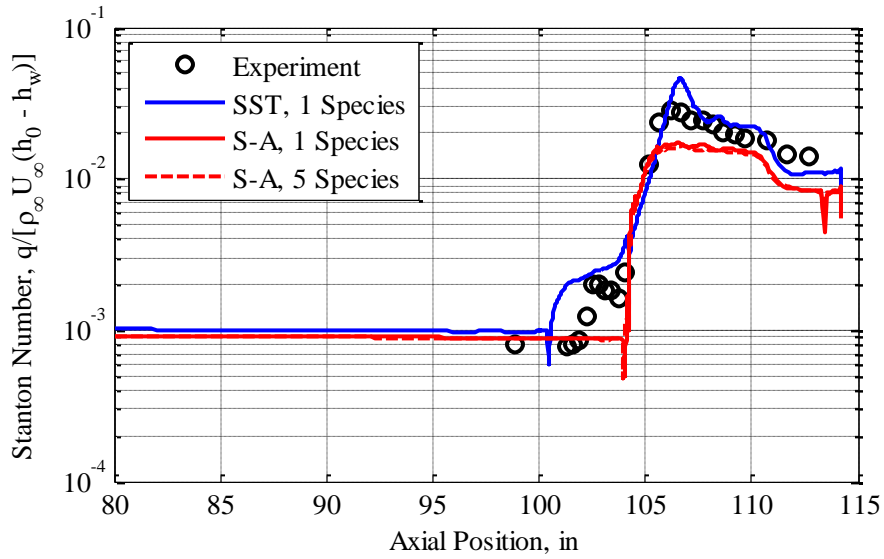


FIGURE 59. Stanton Number as Predicted by Select FY18 6-/42-Degree Cone-Flare Run 4 Simulations, Compared to Experimental Measurements.

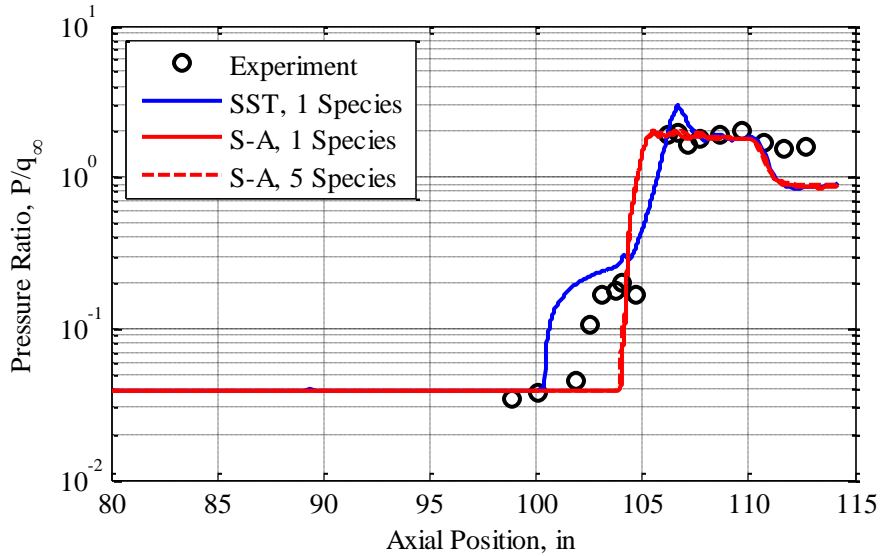


FIGURE 60. Pressure Ratio as Predicted by Select FY18 6-/42-Degree Cone-Flare Run 4 Simulations, Compared to Experimental Measurements.

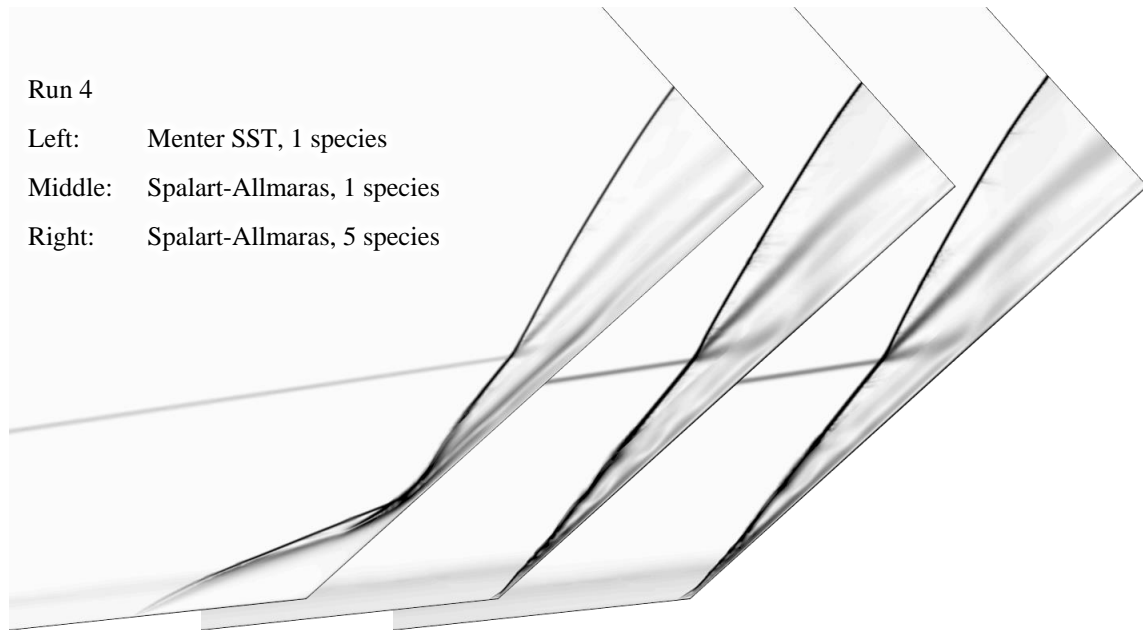


FIGURE 61. Numerical Schlieren Images of the Flowfield as Predicted by Select FY18 6-/42-Degree Cone-Flare Run 4 Simulations.

Heat flux and pressure distribution predictions are compared to the experimental measurements for run 33 in Figures 62 and 63, respectively. The predicted flowfield is illustrated in Figure 64. Both turbulence models predict flow separation, with the point of separation occurring upstream of the experimentally observed location. The Menter SST turbulence model predicts a larger separation bubble than is predicted by the Spalart-Allmaras model. Because of the differences in the separation point, agreement with the experimental measurements downstream is not particularly good. The Spalart-Allmaras model does the best at predicting the heat flux and pressure on the flare, while the Menter SST model is better at predicting heat flux within the separation bubble. Other analysts have simulated this test case using both turbulence models (Reference 15). Due to the graphical presentation of their results, direct comparisons are not possible. However, those earlier results are very consistent with the present solutions.

The flowfields predicted by the simulations for run 45 are compared in Figure 65; Figures 66 and 67 compare the heat flux and pressure predictions, respectively. The predicted distributions shown in these plots are not as smooth as expected. The cause for this is unknown and is probably worthy of further investigation. The Spalart-Allmaras model predicts attached flow, consistent with the experiment, while the Menter SST model predicts a separation bubble approximately 1.5 inches in length. For the two species gas model, separation is predicted to occur approximately 0.25 inch upstream of the separation point predicted by the one species model. This could be due to differences in viscosity, or possibly the effects of thermodynamic nonequilibrium. Otherwise, the

choice of gas model produces only small differences in the results. Both turbulence models predict the pressure distribution on the flare well, except that the peak pressure is under-predicted. The Menter SST model over-predicts heat flux on the flare, while the Spalart-Allmaras model under-predicts it. These simulations agree well with the earlier simulations presented graphically in Reference 15.

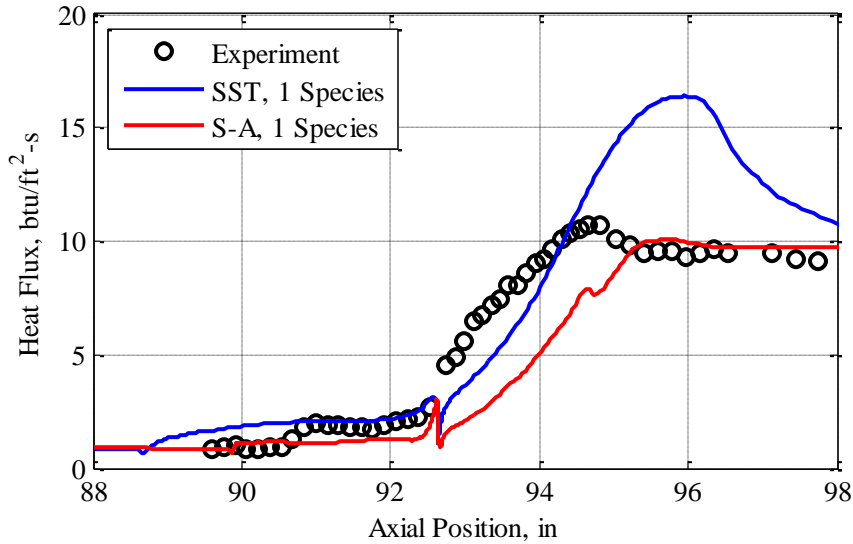


FIGURE 62. Heat Flux Distribution Predictions for 7-/40-Degree Cone-Flare Run 33, Compared to Experimental Measurements.

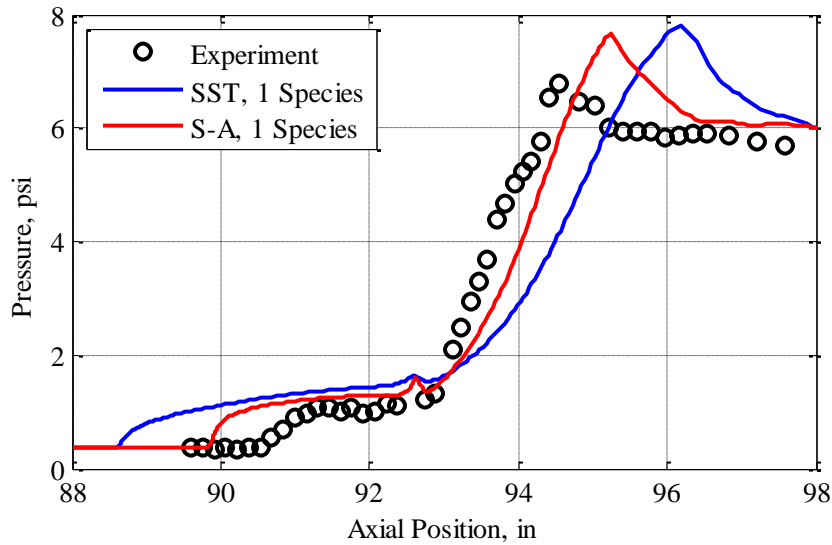


FIGURE 63. Pressure Distribution Predictions for 7-/40-Degree Cone-Flare Run 33, Compared to Experimental Measurements.

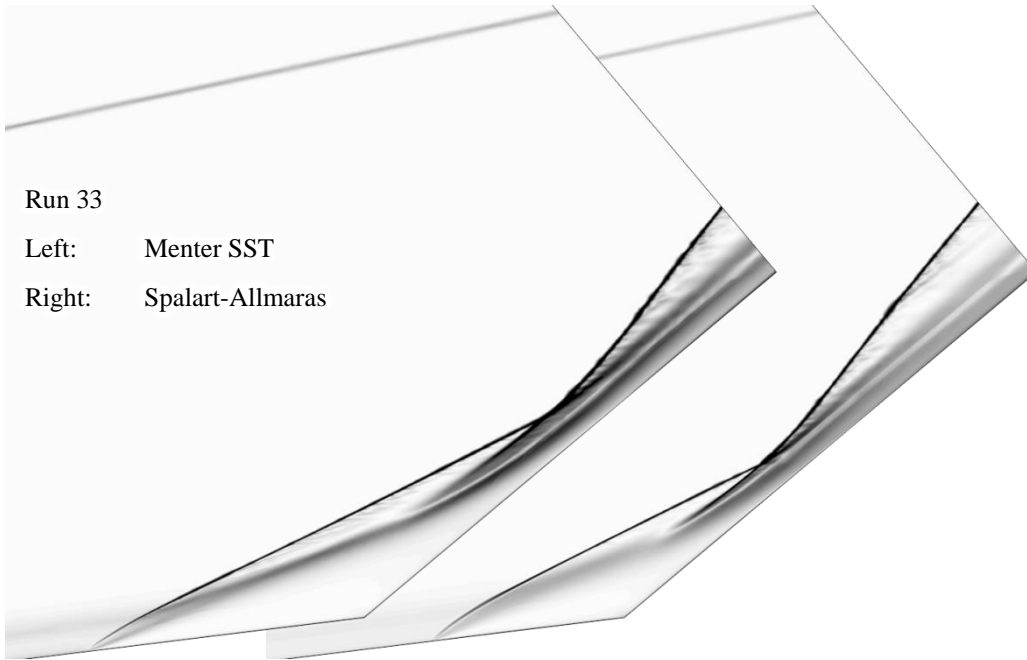


FIGURE 64. Numerical Schlieren Images of Flowfield Predicted for 7-/40-Degree Cone-Flare Run 33.

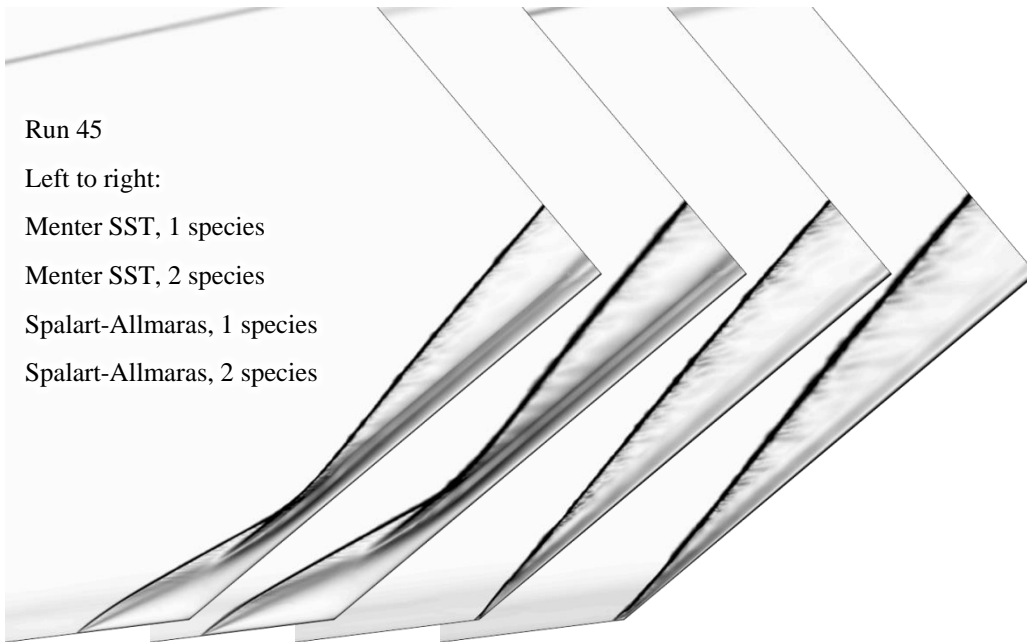


FIGURE 65. Numerical Schlieren Images of Flowfield Predicted for 7-/40-Degree Cone-Flare Run 45.

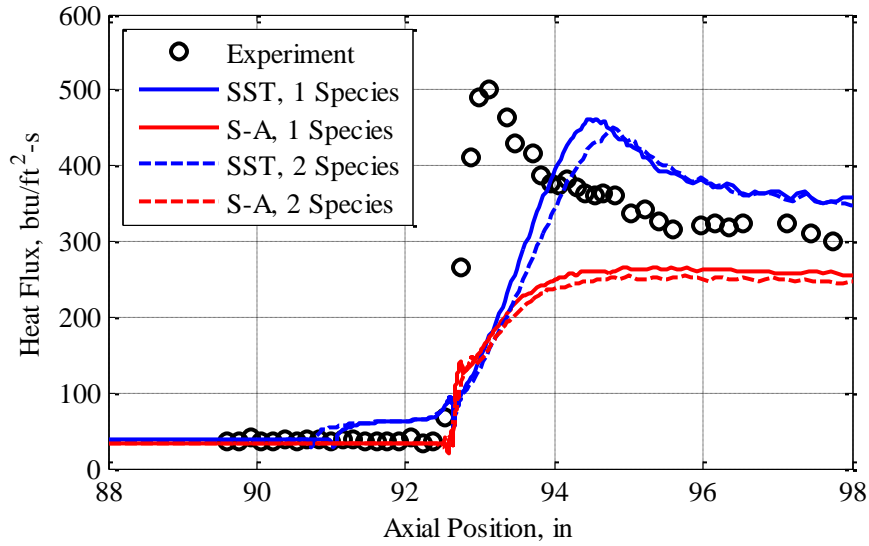


FIGURE 66. Heat Flux Distribution Predictions for 7-/40-Degree Cone-Flare Run 45, Compared to Experimental Measurements.

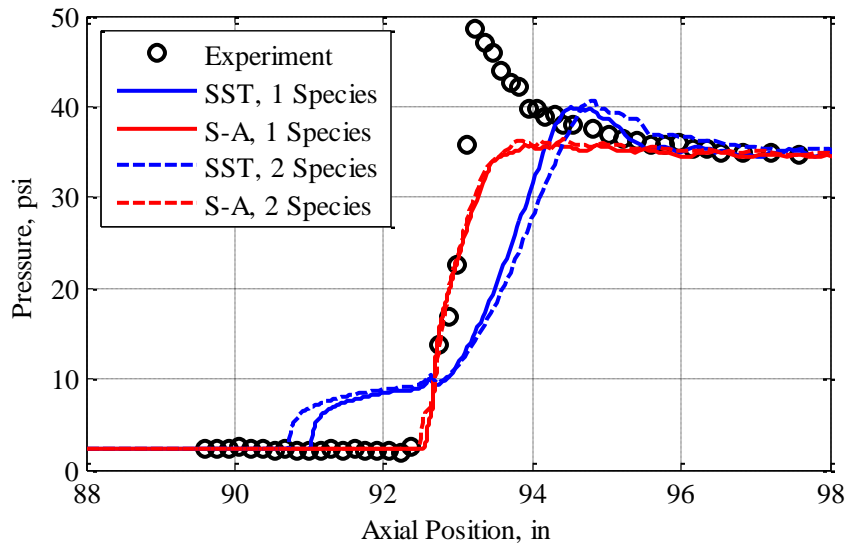


FIGURE 67. Pressure Distribution Predictions for 7-/40-Degree Cone-Flare Run 45, Compared to Experimental Measurements.

For the Spalart-Allmaras simulations performed for run 45, the one species model needs $1.51\text{E-}5$ CPU-seconds per iteration per cell, and the two species model requires $8.95\text{E-}5$ CPU-seconds per iteration per cell. The two species model is therefore about 5.9 times more costly than the one species model. This is surprising, since comparing to the timing data for run 4, it suggests that the two species model is almost as costly as the five species model. It is believed that this is not really representative of the relative computational cost of the two and five species models but more likely is caused by differences in the conditions of the two runs.

4.4 LARGE CYLINDER-FLARE

While the large cylinder-flare test case was not considered in the FY14 effort, select test runs are investigated for this test case in the FY18 effort. The primary run considered is run 18 (nominally Mach 7) while the two runs at a nominal Mach number of 6 (runs 11 and 13, at low and high Reynolds number, respectively) are secondary validation cases. Freestream conditions are presented in Table 5. All simulations make use of the recommended solver settings (see Section 3.2). Two gas models are considered: the one species model, as well as the two species model (which accounts for thermodynamic nonequilibrium). Both the Menter SST (with recommended settings) and the Spalart-Allmaras turbulence models are employed. Convergence of these simulations is determined primarily by monitoring the location of flow separation; all converge to steady solutions, without any significant oscillations.

The prism mesh is sized such that the wall Y^+ remains below 0.1 on the cylinder and below 0.25 on the flare. The mesh is refined three times using the normalized pressure gradient technique. The baseline mesh has approximately 59 thousand cells, with the refined meshes containing about 61, 71, and 91 thousand cells, respectively. The point of flow separation is sensitive to the mesh that is used. The movement of the separation point between the second and third refined meshes is less than 0.4 inch for the Menter SST simulations, and less than 0.15 inch for the Spalart-Allmaras simulations. Thus, it is possible that the results have not reached a completely mesh-converged state, though they are believed to be close.

The flowfields predicted for run 18 are visualized using numerical Schlieren images in Figure 68. It is observed that the Menter SST model predicts larger separation bubbles than are predicted with the Spalart-Allmaras model. Additionally, the two species air model (with thermodynamic nonequilibrium) results in a larger separation bubble for the Menter SST turbulence model, and leads to flow separation occurring with the Spalart-Allmaras model (in contrast, with the one species gas model, the Spalart-Allmaras turbulence model predicts attached flow). These observations are supported by the comparisons of the heat flux and pressure profiles made in Figures 69 and 70. Experimentally, the flow is observed to separate at about 94.1 inches. The one species Menter SST prediction and the two species Spalart-Allmaras predictions agree quite well with this, with separation predicted to occur at 93.66 and 94.29 inches, respectively. Separation as predicted by the two species Menter SST model is farther forward, at 92.33 inches. The pressure profiles (for these simulations predicting separated flows) agree quite well with the experiment in general, though the peak pressure is under-predicted and its location does not match. These discrepancies are caused by the mismatch in the point of flow separation. The Menter SST model does the best job of predicting the heat flux, though the peak heat flux value and the heat flux on the aft end of the flare are somewhat over-predicted. The Spalart-Allmaras model does not capture the increase in heat flux in the separation bubble, and the heat flux on the flare is significantly under-predicted.

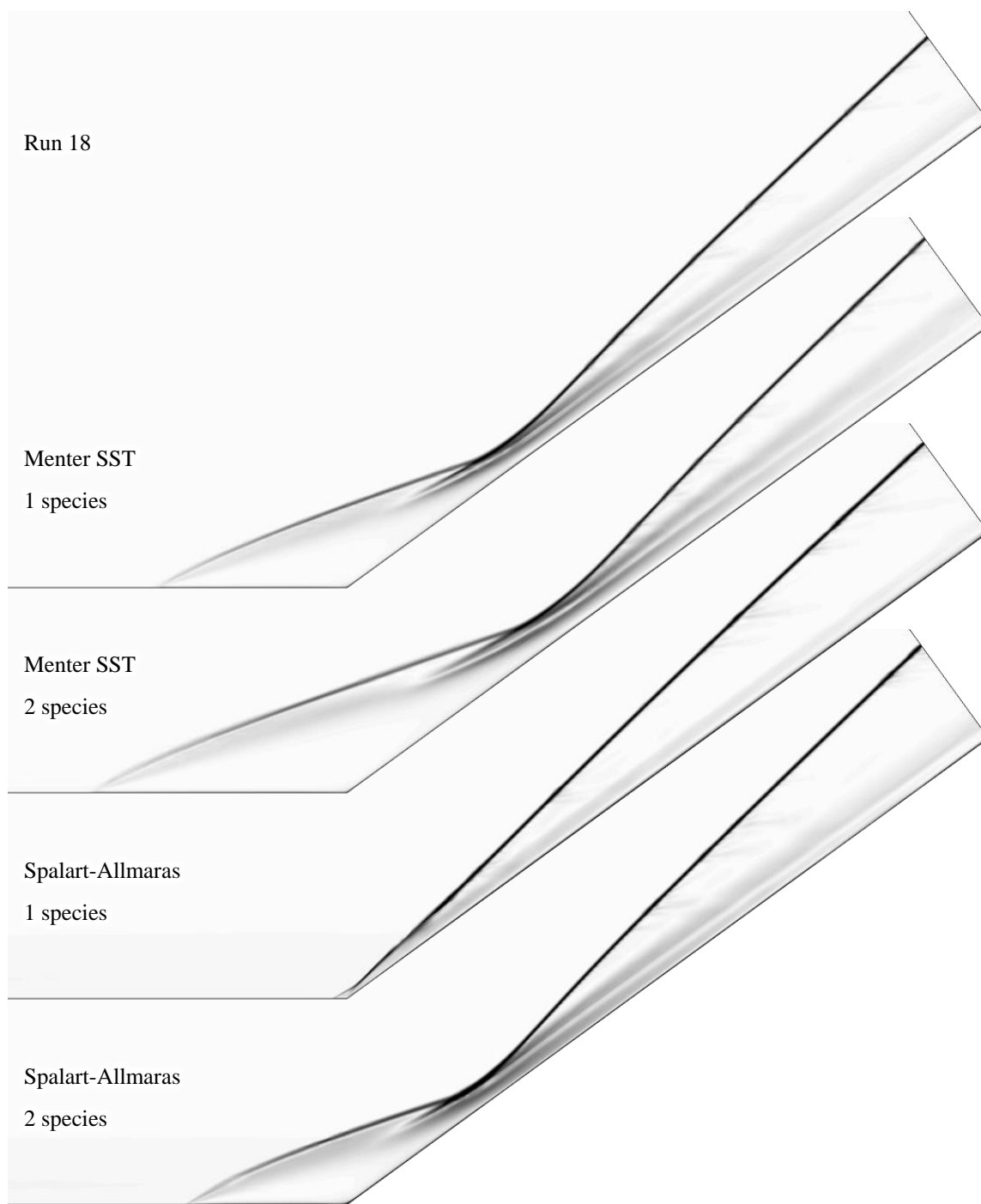


FIGURE 68. Numerical Schlieren Images of Flowfield Predicted for Large Cylinder-Flare Run 18.

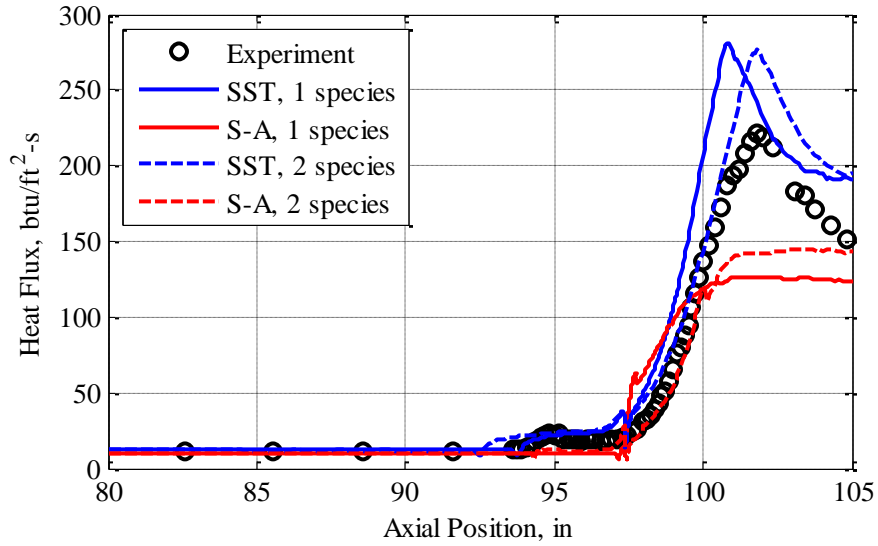


FIGURE 69. Heat Flux Distribution Predictions for Large Cylinder-Flare Run 18, Compared to Experimental Measurements.

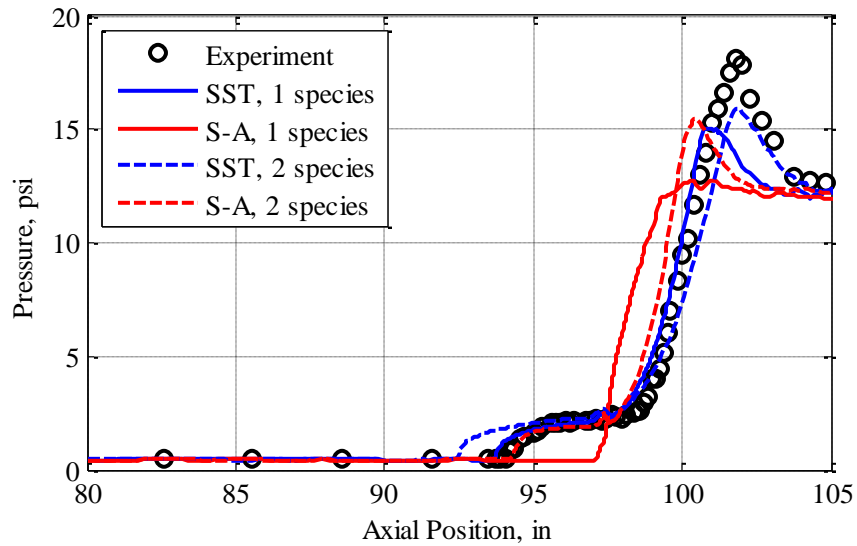


FIGURE 70. Pressure Distribution Predictions for Large Cylinder-Flare Run 18, Compared to Experimental Measurements.

The predicted flowfields for run 11 are compared in Figure 71, with the heat flux and pressure predictions compared to experimental measurements in Figures 72 and 73, respectively. The results for run 11 follow the same trends as those just presented for run 18. One notable difference is that the single species Spalart-Allmaras simulation for run 11 predicts separated flow, while the corresponding simulation for run 18 predicts that the flow would remain attached. A two species simulation with the Spalart-Allmaras is attempted but cannot be completed due to numerical difficulties. The cause for these issues remains unclear. The point of flow separation observed in the experiment for run 11 is the same as that observed for run 18 (about 94.1 inches). The Spalart-Allmaras model simulation is in good agreement, with a predicted separation point of 94.47 inches. The Menter SST turbulence model predicts larger separation bubbles, with separation at 92.60 inches (one species) and 91.70 inches (two species). Both turbulence models predict the pressure profile reasonably well, with the Menter SST model having a small advantage over the Spalart-Allmaras model. The Menter SST model is also significantly better at predicting heat flux, though peak heat flux is over-predicted.

Predictions for run 13 are presented in Figure 74 (flowfield images), Figure 75 (heat flux distribution), and Figure 76 (pressure distribution). These predictions are nearly identical to those for run 11, the only significant difference being that separation is predicted to occur slightly farther downstream. This is not surprising, as both runs 11 and 13 are performed at the same nominal Mach number, with the main difference being a factor of three for the Reynolds number. In the experiment for run 13, separation is observed to occur at about 94.2 inches. The Spalart-Allmaras simulation predicts separation at 94.71 inches; the one and two species predictions for the Menter SST model are 93.12 and 92.44 inches, respectively.

These large cylinder-flare cases have previously been simulated by other researchers using multiple flow solvers (Reference 15). Several analysts used the Menter SST turbulence model, while one analyst used the Spalart-Allmaras model to simulate runs 18 and 11. Their results are only presented graphically, which hinders direct comparisons. For run 18, they predicted separation to occur between about 91.4 and 92.4 inches. The present simulations thus agree better with the experiments in this regard. However, the previous researchers were able to predict the peak pressure and pressure distribution on the flare much more accurately than is possible in this present work. The heat flux predictions for run 18 from this present work are comparable to those obtained by the others. For run 11, the earlier simulations predict separation between about 91.5 and 91.7 inches; the present work agrees just as well with the experiment and for several simulations is significantly better. For run 13, the other analysts had predicted separation between about 92.2 and 92.4 inches; the current simulations agree with the experiment just as well (and often better). The heat flux and pressure profiles predicted in this current work for runs 11 and 13 are consistent with those obtained by the other investigators.

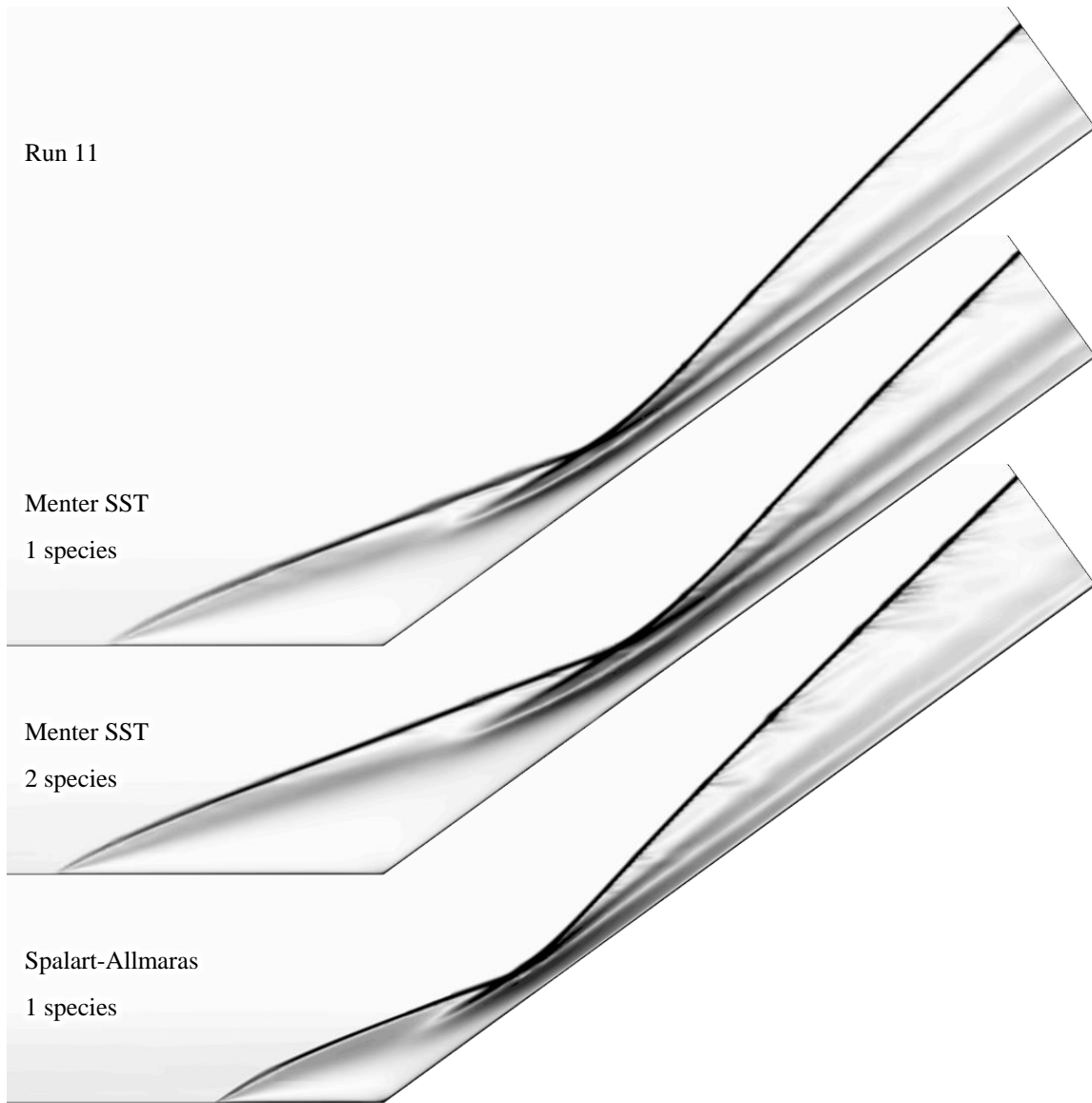


FIGURE 71. Numerical Schlieren Images of Flowfield Predicted for Large Cylinder-Flare Run 11.

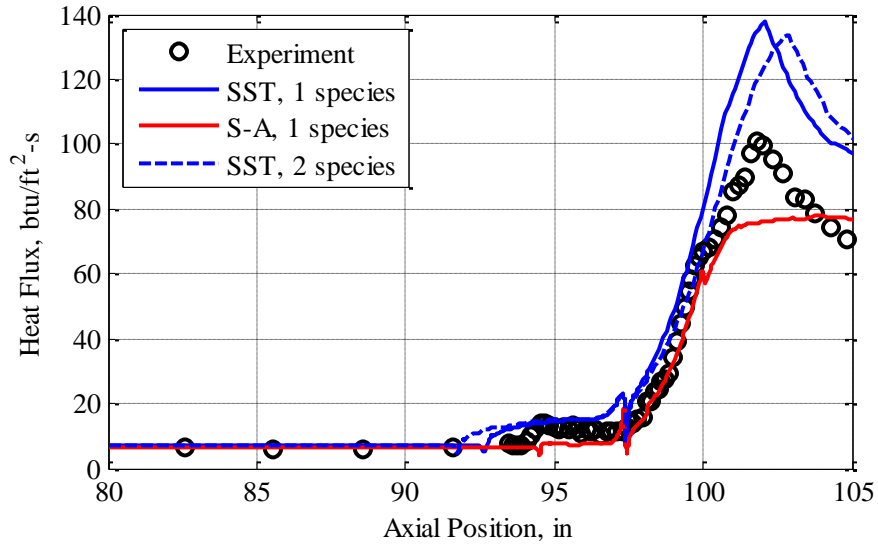


FIGURE 72. Heat Flux Distribution Predictions for Large Cylinder-Flare Run 11, Compared to Experimental Measurements.

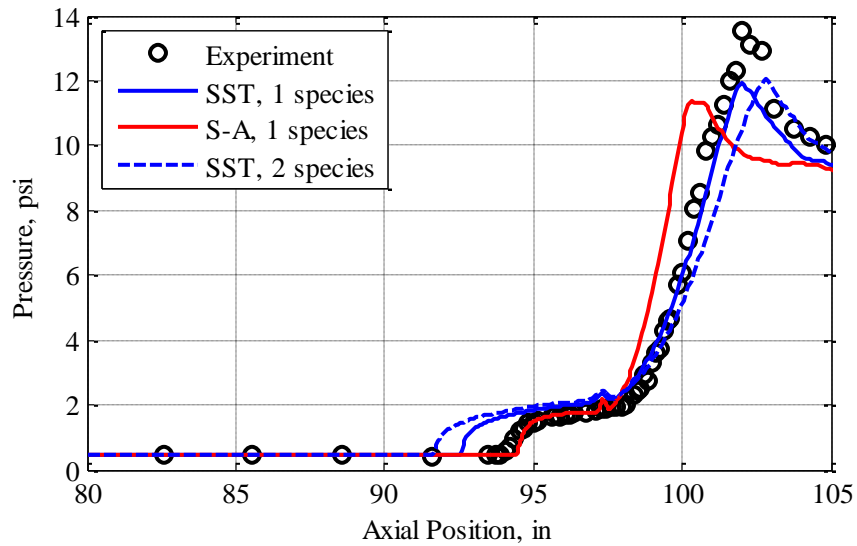


FIGURE 73. Pressure Distribution Predictions for Large Cylinder-Flare Run 11, Compared to Experimental Measurements.

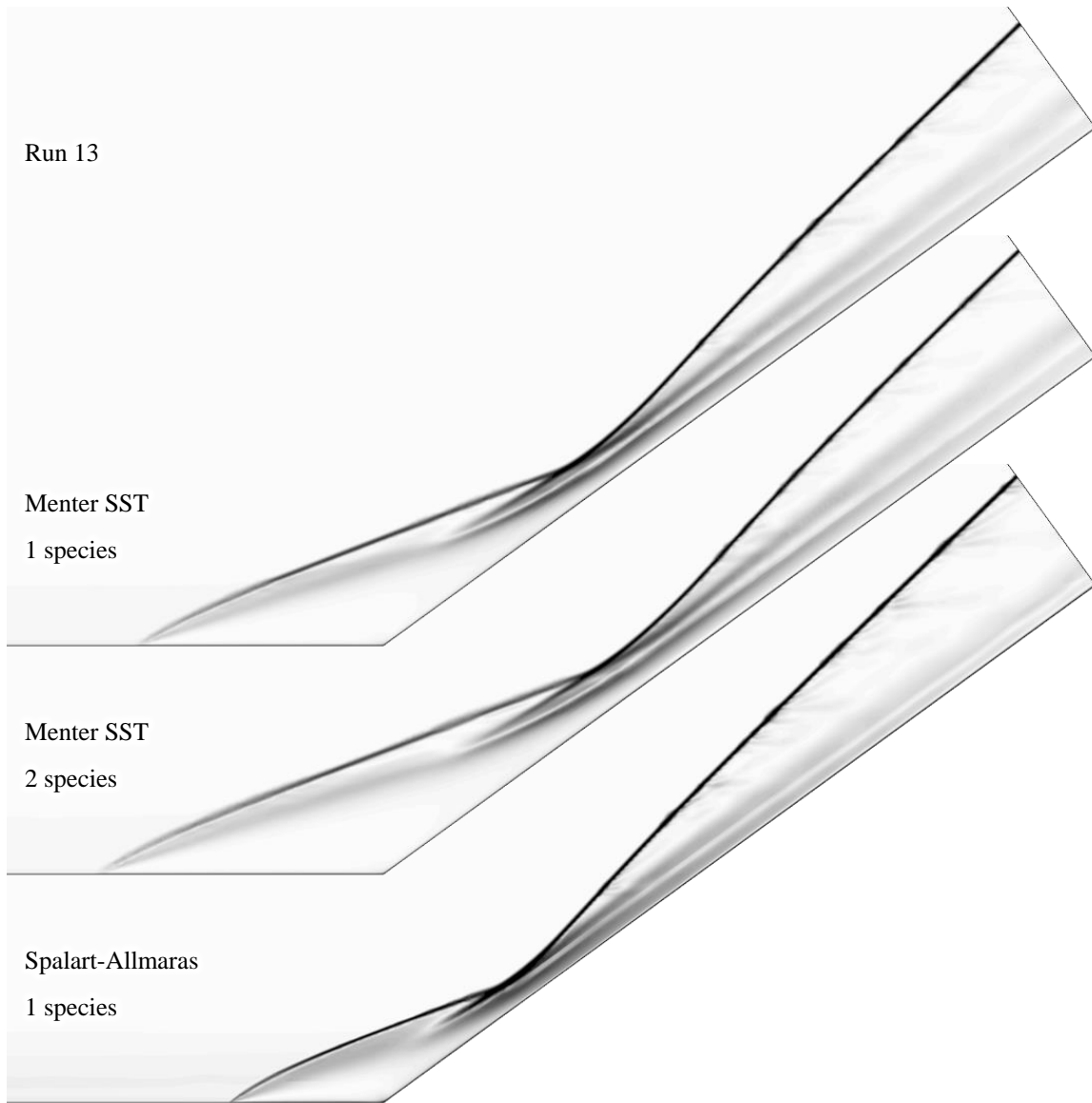


FIGURE 74. Numerical Schlieren Images of Flowfield Predicted for Large Cylinder-Flare Run 13.

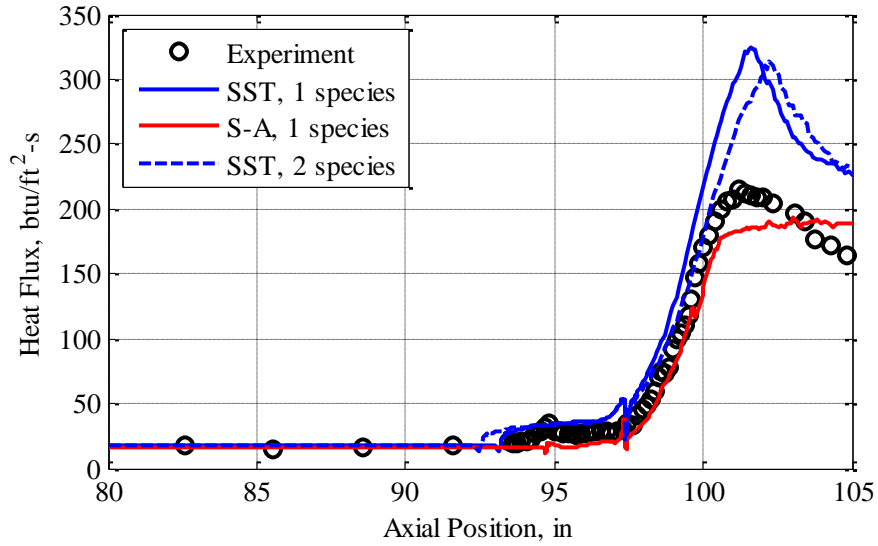


FIGURE 75. Heat Flux Distribution Predictions for Large Cylinder-Flare Run 13, Compared to Experimental Measurements.

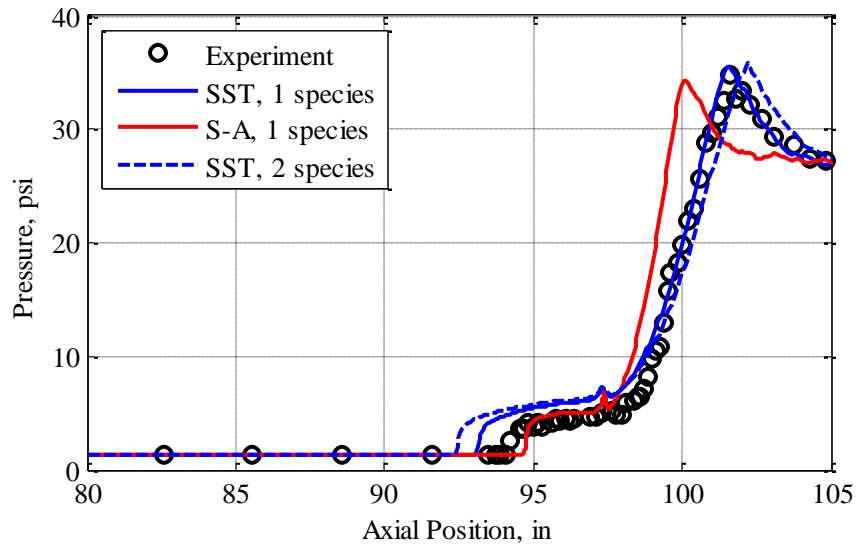


FIGURE 76. Pressure Distribution Predictions for Large Cylinder-Flare Run 13, Compared to Experimental Measurements.

4.5 SHOCK/SHOCK INTERACTION

The shock/shock interaction test case was not considered in the FY14 effort but is one of the first problems simulated as part of the FY18 work. Because these simulations were performed so early in the FY18 effort, they do not make use of some of the best practices that have since been identified. Notable solver settings used in these shock/shock interaction simulations are as follows: AUSM+ flux method, CFL ramping from 0.1 to 10 over the first 100 iterations, grid sequencing initialization, “expert driver” feature activated, and continuity convergence accelerator with enhanced stability treatment activated. All other solver settings are left at their default values. Convergence of these simulations is determined by monitoring the minimum, maximum, and average pressure and heat flux on the cylinder surface, as well as the angular position of peak heat flux and pressure. Many simulations do not converge to a truly steady solution but are observed to yield small-amplitude oscillations in the monitored values. In these cases, an averaged solution is obtained by sampling over 10,000 iterations.

Most simulations are performed using the one species air model. Additional simulations are performed for run 60 using two variants of the two species air model. The first variant assumes thermodynamic equilibrium and models species viscosity, and thermal conductivity using polynomial in temperature curve fits to data presented in Reference 23. The second variant models thermodynamic nonequilibrium; viscosity remains based on a polynomial in temperature, but thermal conductivity is computed based on nonequilibrium kinetic theory.

The mesh used in these simulations is refined three times based on the initial pressure gradient technique discussed in Section 3.5.2. (Indeed, this mesh refinement technique was developed based on these shock/shock interaction simulations.) The prism layer in the mesh is designed such that the wall Y^+ on the cylinder is approximately 1.0 at the location of peak heat flux (and is significantly less elsewhere). The initial mesh contains approximately 11 thousand cells, with subsequent refined meshes containing about 89, 235, 335, and 453 thousand cells. The rapid increase in cell count is largely a result of unintentional refinement in the prism layer region, as discussed in Section 3.5.2.

The first shock/shock interaction test simulated is run 103, with a freestream Mach number 11.63 and a laminar shear layer. Complete freestream conditions are listed in Table 6. However, as is shown in Figure 77, the shear layer and transmitted shock pass below the cylinder, without any direct impingement. This is substantially different from the experiment, which had impingement on the cylinder at an angular position of about 26 degrees below the leading edge. The cause for this discrepancy is thought to be an error in the original test report (Reference 16).

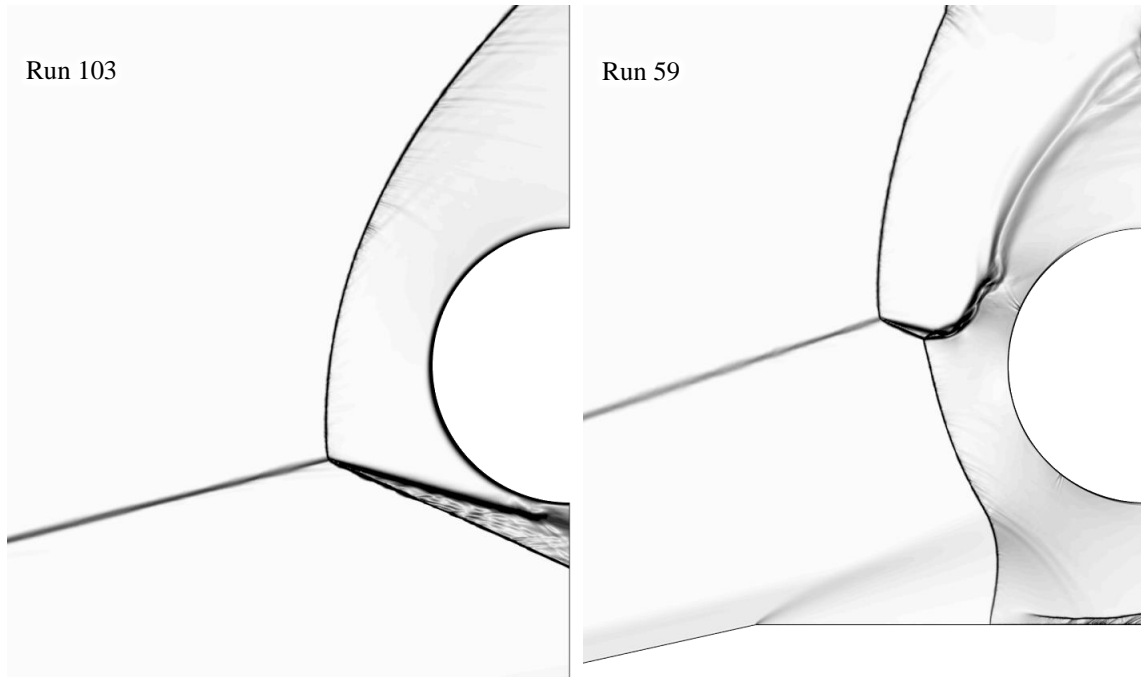


FIGURE 77. Numerical Schlieren Images of Flowfield as Predicted for Shock/Shock Test Case Runs 103 and 59.

The second test simulated is run 59 (freestream Mach 8.036). Since the shear layer was reported to have been turbulent, this simulation used the Menter SST turbulence model (using all default settings). As is illustrated in Figure 77, the predict shock/shock interaction forms a supersonic jet flow feature that passes above the cylinder, without any direct impingement. Again, this is in conflict with the experiment, where direct impingement was measured at about 20 degrees below the leading edge. However, comparing the reported geometric parameters with the Schlieren imagery in Reference 16 indicates that the dimensions listed in the original test report are obviously in error.

The final test simulated is run 60 (freestream Mach 8.039, turbulent shear layer simulated using Menter SST turbulence model with default settings). Numerical Schlieren images of the flowfield predicted using the three different air models are compared in Figure 78. A “type IV” shock/shock interaction is produced, as is evident from the formation of a supersonic jet that directly impinges on this cylinder. This behavior is consistent with the experiment. While difficult to see from these images, for the simulation modeling thermodynamic nonequilibrium the bow shock occurs slightly farther from the cylinder than is predicted by the other two air models. This causes the jet to impinge at a slightly lower point on the cylinder.

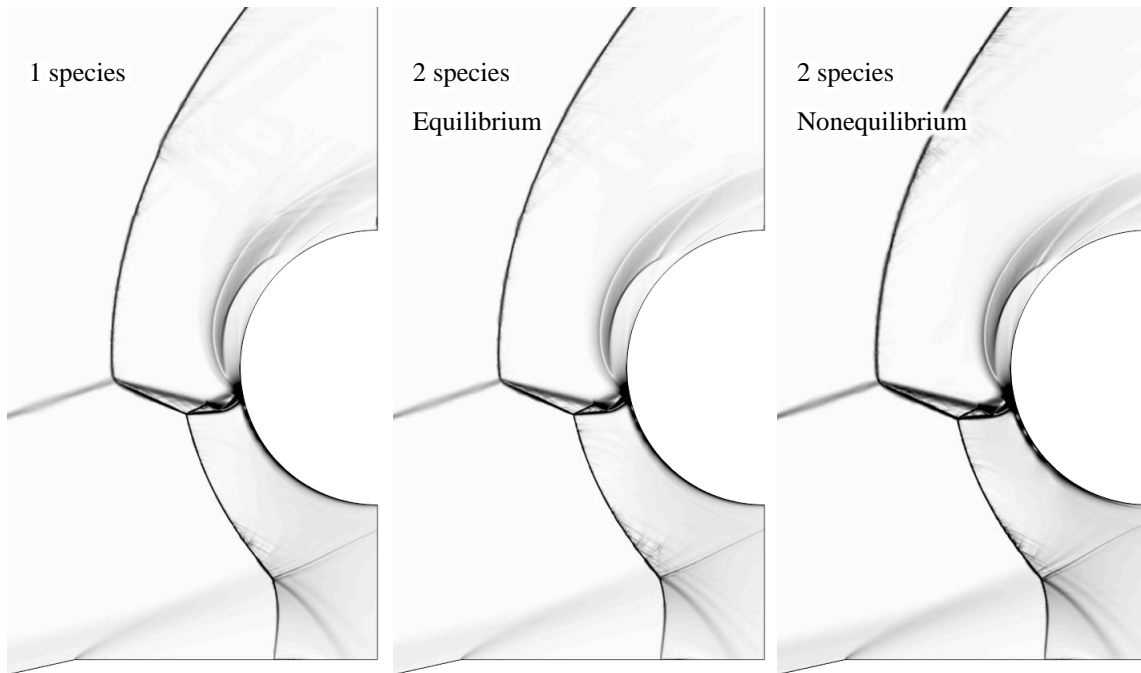


FIGURE 78. Numerical Schlieren Images of Flowfield as Predicted by Shock/Shock Run 60 Simulations.

Additional insight into the predicted flowfield from the simulation with thermodynamic nonequilibrium is given by the temperature and velocity fields presented in Figure 79. Maximum temperature of the translational-rotational energy mode is just over 3,000 °R (1,667 K), which is low enough that chemical reactions can be neglected. There is significant thermodynamic nonequilibrium, with the maximum temperature of the vibrational-electronic energy mode occurring a significant distance downstream of the bow shocks. These images also clearly illustrate the supersonic jet produced by the shock/shock interaction, which subsequently impinges on the cylinder and is mostly deflected over the top of the cylinder. A small separation bubble appears to form at an angular position of about 45 degrees above the cylinder leading edge.

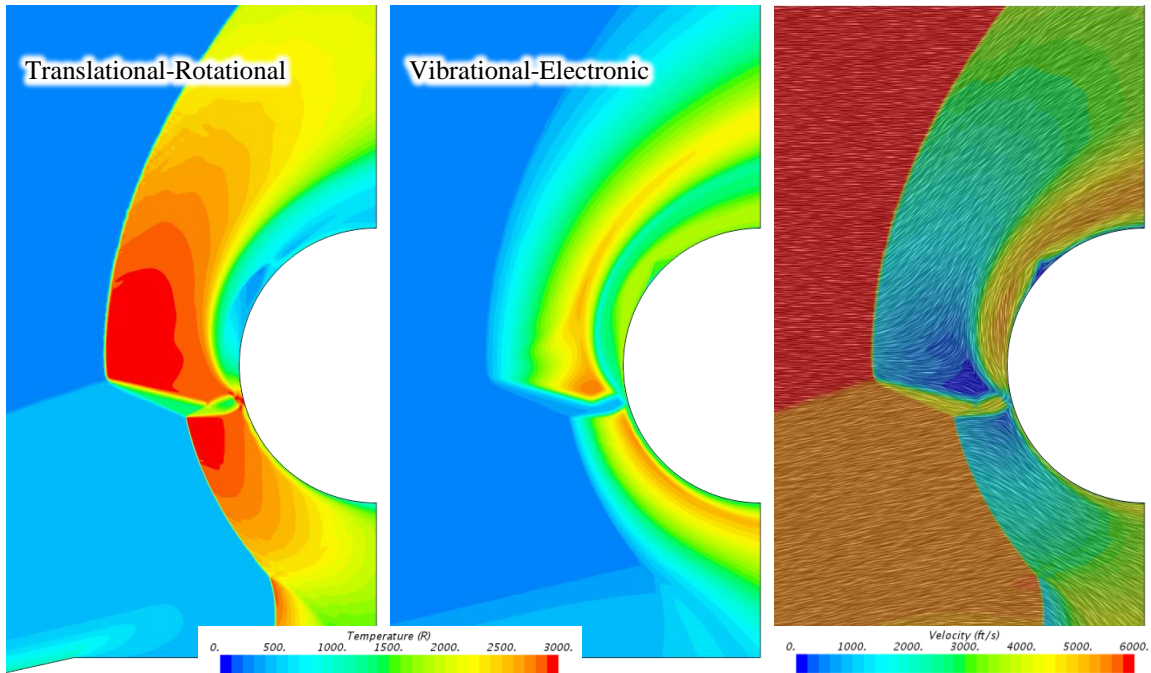


FIGURE 79. Temperature and Velocity Predictions as Predicted by Nonequilibrium Simulation of Shock/Shock Run 60 Test Case.

The predicted heat flux and pressure distributions on the cylinder are compared to experimental measurements in Figures 80 and 81, respectively. Angular position is measured anti-clockwise from the leading edge of the cylinder (thus, the upper surface of the cylinder is associated with negative angles, while positive angles correspond to the bottom surface). It is observed that the peaks in the predicted profiles all fall above (more negative angular position) the experimental measurements. The peaks for single species and the two species equilibrium gas models occur at about 12.5 degrees. For the two species nonequilibrium gas model, the peaks are predicted to occur at about 15 degrees, which provides better agreement with the measured peak location of about 20 degrees. The magnitudes of the peaks as predicted by the nonequilibrium simulation also agree with the measurements better than those predicted by the other two simulations. All three simulations show secondary peaks that occur below (more positive angular position) the main peak; these secondary peaks are not observed in the experiment. The heat flux and pressure predictions for all simulations agree well with the experiment away from the impingement region.

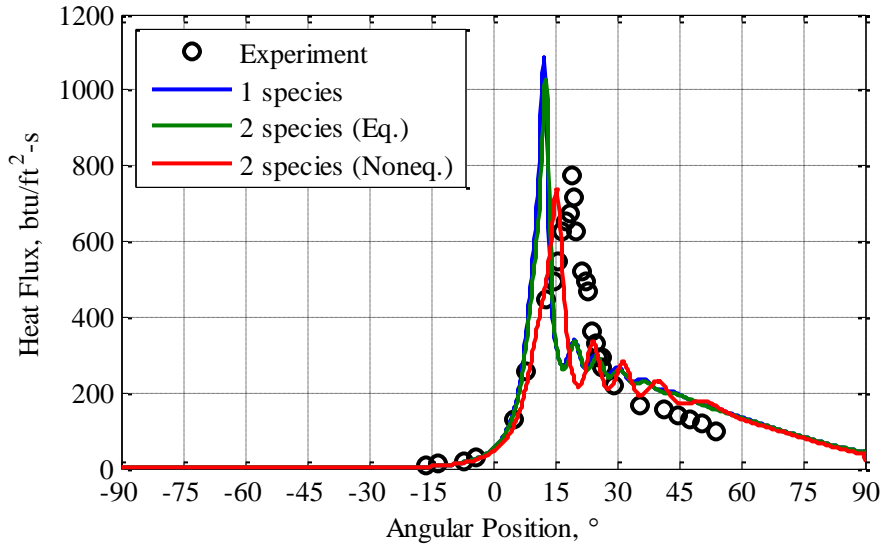


FIGURE 80. Heat Flux Distribution Predictions for Shock/Shock Run 60, Compared to Experimental Measurements.

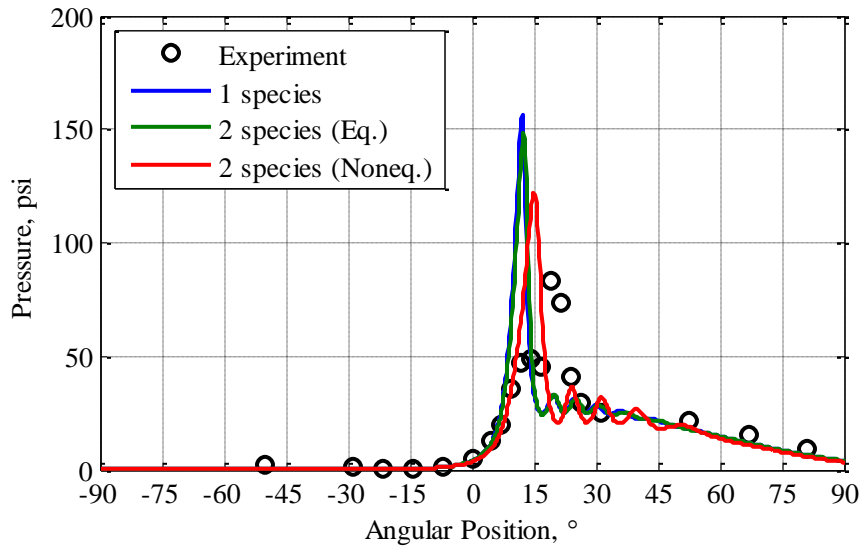


FIGURE 81. Pressure Distribution Predictions for Shock/Shock Run 60, Compared to Experimental Measurements.

This agreement between the simulations and the experiment is believed to be quite good. The small difference in the location of the peaks is considered to be relatively insignificant. Other analysts who have modeled this same basic problem geometry (though not this exact run) have noted significant sensitivity to the impinging shock location (Reference 25). It is entirely possible that imprecisely reported geometry parameters, or small deflections during the test, could explain the observed discrepancies between test and simulation.

Information describing the computational cost of the three simulations for run 60 is extracted. Computational cost is 2.09E-5, 3.46E-5, and 1.07E-4 CPU-seconds per iteration per cell for the one species, two species (equilibrium), and two species (nonequilibrium) simulations, respectively. The two species simulations are thus respectively about 1.7 and 5.1 times as costly as the one species simulation. Additionally, it can clearly be observed that modeling thermodynamic nonequilibrium incurs a large computational cost, as the time required to complete each iteration is increased by over a factor of three, even though the number of species remains the same.

5.0 LESSONS LEARNED AND RECOMMENDATIONS

In the course of executing this research activity, a number of issues were encountered and occasional missteps were made. The lessons learned from these challenges are summarized here, along with recommended best practices that can be used to guide future analyses towards success and away from known pitfalls.

- Nonequilibrium simulations are much more sensitive to mesh quality than simulations assuming thermodynamic equilibrium.
- The nonequilibrium solver has difficulty solving flows with very low temperatures. One example is cone-flare run 4, with a freestream temperature of 121°R. Symptoms of this problem include non-physical vibrational-electronic temperature predictions, often culminating in a floating point error and simulation failure. This limitation should have no real impact on free-flight problems (since the lowest ambient temperature for the standard atmosphere is 336.5°R in the mesopause) but does limit the experimental test cases that can be considered.
- STAR-CCM+ cannot properly handle freestream nonequilibrium; the vibrational-electronic temperature on inflow boundaries is always equilibrated with the translational-rotational temperature. This assumption is reasonable for simulations of free-flight problems (where the freestream is, in fact, in equilibrium) but makes it impossible to accurately predict certain experiments where the freestream is in thermodynamic nonequilibrium.

- STAR-CCM+ cannot model ionization. This may limit the suitability of using STAR-CCM+ to model flows with freestream Mach numbers exceeding 12, depending on freestream temperature.
- Some default values in the material property database in STAR-CCM+ are incorrect. Examples include the Sutherland's constants for the viscosity and thermal conductivity of N₂. The user should always verify the material properties being used against a trusted source.
- The thermodynamic polynomials in the STAR-CCM+ material property database are not applicable to temperatures below 200 K and often are not applicable above 1,000 K. For hypersonic simulations, the default polynomials need to be replaced with updated polynomials applicable over a wider temperature range.
- If specific heat polynomials are used outside their applicable range, unexpected results can be obtained. One symptom of this is that the specified freestream Mach number may not be achieved in the simulation.
- It is strongly recommended that future hypersonic simulations make use of one of the "standardized" air models described in this work, as appropriate for the given situation. If thermodynamic equilibrium is appropriate, either the one species or the equilibrium air model should be employed. The two species model should be used to capture the effects of thermodynamic nonequilibrium when reactions are not expected. Simulations involving temperatures above 2,500 K should consider the five species model to capture the effects of thermodynamic nonequilibrium and finite-rate chemical reactions.
- Future simulations should make use of the recommended solver settings listed in Section 3.2. These settings have been found to work extremely well, allowing simulations to converge quickly without significant stability or numerical issues. It may also be possible to increase the maximum CFL number above the value of 10 used in this work; this should be investigated in the future.
- Instability encountered for a CFL number of 1.0 is usually indicative of an issue elsewhere in the problem setup (often, but not always, mesh related). If this occurs, the other aspects of the problem setup should be thoroughly reviewed before reducing the CFL number further.
- Inflow and far field boundaries should be modeled using the freestream boundary condition option. Other options (e.g., velocity inlet) are found to not work well. Outflow boundaries that do not intersect the model geometry can also be modeled with the freestream boundary condition. However, if the outflow boundary intersects the geometry (as is the case in most of the test cases

considered in this work), using the pressure outlet boundary condition is found to provide the best results.

- The initial and freestream mass fractions for minor species (e.g., NO, N, and O) should be set to some low, non-zero value (e.g., 1.0E-10). Setting the mass fractions exactly to zero can cause some issues with the chemistry solver, resulting in floating point errors and simulation failure.
- When using the recommended solver settings, the grid sequencing initialization technique has been found to work very well; this is the recommended initialization approach. If this fails, initialization should be attempted using either the impulsive start or ramped inflow methods. Failure of all three of these initialization methods is usually indicative of an issue somewhere in the problem setup, which should be investigated before pursuing more exotic initialization approaches.
- Structured directed meshes can be used for two-dimensional simulations but are not well-suited for complicated three-dimensional geometries. High aspect ratio or highly skewed cells produced in the directed mesh can also be problematic.
- Mesh refinement of flows with multiple shocks with differing strengths is best accomplished with the normalized pressure gradient refinement technique. This mesh refinement technique has been successfully demonstrated for two- and three-dimensional simulations, and should be considered for use in future simulations.
- The predicted location of flow separation is found to be sensitive to the mesh that is used. Multiple refinements of the mesh should thus be employed to ensure that a mesh-converged solution is obtained.
- When thermodynamic nonequilibrium is being modeled, the predicted location of flow separation is different from (usually upstream of) the location predicted when thermodynamic equilibrium is assumed.
- Errors and other conflicts exist in the documentation for the different experiments performed at CUBRC. The test runs and freestream values reported here appear to be those most thoroughly documented, and thus best suited for use as validation cases. These identified test cases can serve as a good starting point for any future validation efforts performed for other flow solvers.
- The heat flux profiles for the laminar test cases are often consistently under-predicted, even though the trends are captured correctly. This should probably be investigated further in future work.

- The predicted location of flow separation rarely matches that observed in the experiments. The predicted flow separation point is too far downstream for the double cone test cases and is too far upstream for the small (laminar) cylinder-flare test cases. For the turbulent cone-flare and large cylinder-flare test cases, the predicted separation point is forward of the experimental location.
- The Menter SST and the Spalart-Allmaras turbulence models are found to be the most appropriate for the hypersonic flowfields considered in this work. All the other RANS turbulence models available in STAR-CCM+ produce results with very poor agreement with the experiments. To obtain the best results with the Menter SST model, three settings need to be set to non-default values, as recommended in Section 3.2.
- The Menter SST model predicts larger separation bubbles than those predicted by the Spalart-Allmaras model. The Spalart-Allmaras model often predicts attached flow, even if separation is observed in the corresponding experiment.
- Both recommended turbulence models predict pressure profiles with reasonable agreement to the experimental measurements (once the effects of differences in the predicted separation points are taken into account).
- The Menter SST model tends to over-predict heat transfer, while the Spalart-Allmaras model under-predicts heat flux, and does not capture the correct trends for heat transfer within the separation bubble. The Menter SST model is therefore assessed as being substantially better than the Spalart-Allmaras model for predicting heat flux.
- Future work needs to explore the use of non-RANS approaches (e.g., large eddy simulations) for modeling the turbulence hypersonic test cases.
- There is a need for development of new RANS turbulence models that can appropriately model high speed, separated flows. In particular, these models need to be capable of accurately predicting heat transfer.
- Modeling thermodynamic nonequilibrium is costly. For the shock/shock interaction test case, modeling nonequilibrium with a two species gas model is more than three times as computationally costly as a two species simulation assuming equilibrium. Simulations performed for one of the double cone runs using the five species model is found to be 2.4 times as expensive as the two species simulation. Different runs for the cone-flare test case suggest that both the two species and five species models are about six times more expensive than the one species model. However, these computation expense comparisons are hindered by test case differences. If more accurate computational cost

information is required, a better timing study will need to be conducted that permits more direct comparisons.

6.0 CONCLUSIONS

A review of the literature was made to identify experiments that could serve as useful hypersonic validation test cases. A large number of test cases exploring a range of different problem geometries have been investigated in the experimental facilities at CUBRC. The data acquired from these experiments appear quite rich, though the documentation was found to be quite poor. A set of test cases that appeared to be the most comprehensively and consistently described in the literature was selected for consideration in this effort and should be used as a starting point for any future validation effort of other flow solvers. A number of test cases explored in the FY14 portion of this effort featured freestream nonequilibrium; these were replaced with the FY18 effort by newer experiments with the freestream in equilibrium. Selected test case geometries include the double cone and short hollow cylinder-flare (investigating shock/laminar boundary layer interactions), the cone-flare and large hollow cylinder-flare (investigating shock/turbulent boundary layer interactions), and a shock/shock interaction test case.

Several weaknesses were identified in the default material properties database built into STAR-CCM+. A set of “standard” air models was therefore constructed based upon data from traceable sources. It is strongly recommended that these air models be used in future hypersonic analysis efforts. A set of solver settings was also identified that routinely resulted in stable simulations with fast convergence; these settings should also be employed in future simulations. A technique for refining a mesh based upon normalized pressure gradients was developed and successfully used to produce meshes optimized to capture shocks and other flow features important to hypersonic flows. Tools were created that allow this technique to easily be applied to future simulations.

The double cone simulations performed in FY14 were for test runs that had significant freestream nonequilibrium, which cannot be modeled in STAR-CCM+. It was thus not possible to accurately simulate these runs. However, it was observed that modeling the nonequilibrium behind the shock resulted in improved agreement with the experiments than simulations that assumed thermodynamic equilibrium. It was also found that the nonequilibrium solver was quite sensitive to mesh quality. Five test runs with freestream equilibrium were investigated in the FY18 effort; all were simulated with a five species air model accounting for nonequilibrium and chemistry. Separation was typically predicted to occur downstream of the point it was observed experimentally, except for run 3, where excellent agreement with the experiment was obtained. Pressure profiles were generally well predicted (taking into account differences caused by the different separation points). Heat flux followed the same trends as the experiment, but tended to be consistently under-predicted by a small amount. The double cone test case demonstrated simulations of flowfields with significant thermodynamic and chemical

nonequilibrium. The simulations completed in this work are generally equivalent to or better than those produced by other analysts using research codes, with the exception of the slight, consistent under-prediction of heat flux.

Five test runs for the short (laminar) hollow cylinder-flare test case were simulated during the FY18 portion of this effort; all used the five species air model. It was found that the flow separation predictions were quite sensitive to the mesh that was used; the resulting predicted separation point tends to be upstream of the experimental location. The pressure and heat flux profiles agreed reasonably well with the experiment. Peak pressure and heat-flux were always over-predicted and were followed by a region where the solution was under-predicted. In general, the heat flux predictions tended to be less than the measurements. Simulations from this present work are very consistent with those produced by other researchers using research codes.

The cone-flare test case was briefly investigated in the FY14 effort but was considered in much more detail as part of the FY18 work. All relevant RANS turbulence models included within STAR-CCM+ were investigated, and for one of these models, different non-default settings and options were explored. Several turbulence models predicted flow separation far forward of the location observed in the experiment. The Menter SST model (once three non-default options were set) and the Spalart-Allmaras models were found to be the most suitable for these high speed, separated flows. The Menter SST predicted larger separation bubbles than the Spalart-Allmaras model, which occasionally predicted attached flow when separated flow was encountered in the experiment. When flow separation was predicted, the separation point from the simulations was always upstream of that observed in the experiments. When nonequilibrium was modeled, flow separation occurred farther upstream than when equilibrium was assumed. As was found before, the predicted separation point was sensitive to the mesh that was used. Both models predict pressure reasonably well (excluding discrepancies related to the differences in separation point). The Menter SST model tends to over-predict heat flux, while the Spalart-Allmaras model under-predicts it. The simulations produced in the work with STAR-CCM+ agree well with analyses performed by other researchers using specialized research codes.

For the large (turbulent) hollow cylinder-flare test geometry, three different runs were simulated as part of the FY18 portion of this effort. Conclusions drawn from this test case are similar to those obtained from the cone-flare test case. Flow separation point was sensitive to the mesh. The Menter SST turbulence model always predicted separation upstream of the location observed in the experiment. The Spalart-Allmaras model typically predicted separation slightly downstream from the experimental location, though in one scenario it predicted attached flow. Modeling thermodynamic nonequilibrium increased the size of the separation bubble, which did not always improve agreement with the experiment. Pressure profiles were predicted reasonably well by both turbulence models. The Menter SST model was better at predicting heat flux, though there was some over-prediction. The simulations completed in this effort are consistent

with and comparable to simulations performed by others, with the current work actually being better at predicting the separation point.

The final test case considered was the shock/shock interaction case. Errors were found in the test report, rendering two the test runs unusable as validation cases. However, good agreement was obtained between the simulation and experiment for the third test run considered. Modeling thermodynamic nonequilibrium caused the shocks to change position slightly from their location predicted assuming equilibrium. This had a noticeable impact on the position of the supersonic jet impingement region on the cylinder. Including the effects of nonequilibrium brought the predictions into better agreement with the experiment.

In conclusion, the ability of STAR-CCM+ to predict hypersonic flows was validated against experimental data for a broad range of test cases. While agreement is not perfect, the results obtained with STAR-CCM+ were very consistent with those obtained by specialized, research-oriented solvers. In several cases, STAR-CCM+ predictions were in better agreement with the experiments than those obtained with the research codes. Additionally, a set of best practices has been established that can be used to guide future STAR-CCM+ simulations of challenging hypersonic problems. The learning curve associated with modeling hypersonic flows with STAR-CCM+ has been climbed, and the experienced gained in this effort can be applied when supporting customers. As a result of this research activity, future production simulations can be completed much more quickly and with higher confidence in the results.

REFERENCES

1. J. D. Anderson Jr. *Hypersonic and High-Temperature Gas Dynamics*, Second Edition, Reston, VA: American Institute of Aeronautics and Astronautics, 2006.
2. M. S. Holden, T. P. Wadhams, and M. MacLean. "A Review of Experimental Studies with the Double Cone and Hollow Cylinder/Flare Configurations in the LENS Hypervelocity Tunnels and Comparisons With Navier-Stokes and DSMC Computations," *48th AIAA Aerospace Sciences Meeting*, Orlando, Florida, 2010. AIAA 2010-1281. DOI: 10.2514/6.2010-1281.
3. J. K. Harvey, M. S. Holden, and T. P. Wadhams. "Code Validation Study of Laminar Shock/Boundary Layer and Shock/Shock Interactions in Hypersonic Flow. Part B: Comparison with Navier-Stokes and DSMC Solutions," *39th Aerospace Sciences Meeting*, Reno, Nevada, January 2001. AIAA 2001-1031. DOI: 10.2514/6.2001-1031.
4. M. S. Holden, T. P. Wadhams, J. K. Harvey, and G. V. Candler. "Comparisons Between Measurements in Regions of Laminar Shock Wave Boundary Layer Interaction in Hypersonic Flows with Navier-Stokes and DSMC Solutions," Buffalo, New York, 2006. RTO-TR-AVT-007-V3.
5. M. S. Holden, T. P. Wadhams, G. V. Candler, and J. K. Harvey. "Measurements in Regions of Low Density Laminar Shock Wave/Boundary Layer Interaction in Hypervelocity Flows and Comparison With Navier-Stokes Predictions," *41st Aerospace Sciences Meeting*, Reno, Nevada, January 2003. AIAA 2003-1131. DOI: 10.2514/6.2003-1131.
6. T. P. Wadhams and M. S. Holden. "Summary of Experimental Studies for Code Validation in the LENS Facility and Comparisons With Recent Navier-Stokes and DSMC Solutions for Two- and Three-dimensional Separated Regions in Hypervelocity Flows," *42nd AIAA Aerospace Sciences Meeting*, Reno, Nevada, January 2004. AIAA 2004-0917. DOI: 10.2514/6.2004-917.
7. M. S. Holden and T. P. Wadhams. "A Review of Experimental Studies for DSMC and Navier-Stokes Code Validation in Laminar Regions of Shock/Shock and Shock/Boundary Layer Interaction Including Real Gas Effects in Hypervelocity Flows," *36th AIAA Thermophysics Conference*, Orlando, Florida, June 2003. AIAA 2003-3641. DOI: 10.2514/6.2003-3641.
8. M. S. Holden, M. MacLean, T. P. Wadhams, and A. Dufrene. "Measurements of Real Gas Effects on Regions of Laminar Shock Wave/Boundary Layer Interaction in Hypervelocity Flows for 'Blind' Code Validation Studies," *21st AIAA Computational Fluid Dynamics Conference*, San Diego, California, June 2013. AIAA 2013-2837. DOI: 10.2514/6.2013-2837.

9. M. S. Holden, T. P. Wadhams, M. MacLean, and A. Dufrene. "Experimental Research and Analysis in Supersonic and Hypervelocity Flows in the LENS Shock Tunnels and Expansion Tunnel," *20th AIAA International Space Planes and Hypersonic Systems and Technologies Conference*, Glasgow, Scotland, July 2015. AIAA 2015-3660. DOI: 10.2514/6.2015-3660.
10. M. MacLean, M. S. Holden, and A. Dufrene. "Measurements of Real Gas Effects on Regions of Laminar Shock Wave/Boundary Layer Interaction in Hypervelocity Flows," *44th AIAA Fluid Dynamics Conference*, Atlanta, Georgia, 2014. http://www.cubrc.org/_iassets/docs/laminar-xx-paper.pdf
11. M. MacLean, M. S. Holden, and A. Dufrene. "Comparison Between CFD and Measurements for Real-Gas Effects on Laminar Shockwave Boundary Layer Interaction," *44th AIAA Fluid Dynamics Conference*, Atlanta, Georgia, 2014. http://www.cubrc.org/_iassets/docs/CUBRC_laminar_Atlanta.pdf
12. M. S. Holden, T. P. Wadhams, and M. MacLean. "Measurements in Regions of Shock Wave/Turbulent Boundary Layer Interaction From Mach 4 to 10 for Open and 'Blind' Code Evaluation/Validation," *21st AIAA Computational Fluid Dynamics Conference*, San Diego, California, June 2013. AIAA 2013-2836. DOI: 10.2514/6.2013-2836.
13. M. S. Holden, T. P. Wadhams, and M. MacLean. "Measurements in Regions of Shock Wave/Turbulent Boundary Layer Interaction From Mach 4 to 10 at Flight Duplicated Velocities to Evaluate and Improve the Models of Turbulence in CFD Codes," *44th AIAA Fluid Dynamics Conference*, Atlanta, Georgia, 2014. http://www.cubrc.org/_iassets/docs/Turbulent-SWTBL-paper.pdf
14. M. S. Holden, T. P. Wadhams, and M. MacLean. "Measurements in Regions of Shock Wave/Turbulent Boundary Layer Interaction on Double Cone and Hollow Cylinder/Flare Configurations From Mach 5 to 8 at Flight Velocities for Open and 'Blind' Code Evaluation/Validation," *44th AIAA Fluid Dynamics Conference*, Atlanta, Georgia, 2014. http://www.cubrc.org/_iassets/docs/1_Holden_AIAA_Atlanta_SWTBI.pdf
15. T. P. Wadhams, M. S. Holden, and M. MacLean. "Comparisons of Experimental and Computational Results From 'Blind' Turbulent Shock Wave Interaction Study Over Cone Flare and Hollow Cylinder Flare Configurations," *44th AIAA Fluid Dynamics Conference*, Atlanta, Georgia, 2014. http://www.cubrc.org/_iassets/docs/6_Wadhams_AIAA_Atlanta_SWTBI.pdf
16. Langley Research Center. *Studies of Aerothermal Loads Generated in Regions of Shock/Shock Interaction in Hypersonic Flow*, by M. S. Holden, J. R. Moselle, and J. Lee. Hampton, Virginia, Langley Research Center, 1991. NASA CR-181893.

17. Glenn Research Center. *NASA Glenn Coefficients for Calculating Thermodynamic Properties of Individual Species*, by B. J. McBride, M. J. Zehe, and S. Gordon. Cleveland, Ohio, Glenn Research Center, 2002. NASA TP 2002-211556.
18. M. E. Ewing and D. A. Isaac. "Mathematical Modeling of Multiphase Chemical Equilibrium," *Journal of Thermophysics and Heat Transfer*, Vol. 29, No. 3, July 2015, pp. 551-562. DOI: 10.2514/1.T4397.
19. Sandia National Laboratories. *A Fortran Computer Code Package for the Evaluation of Gas-Phase Multicomponent Transport Properties*, by R. J. Kee, G. Dixon-Lewis, J. Warnatz, M. E. Coltrin, and J. A. Miller. Albuquerque, New Mexico, Sandia National Laboratories, 1986. Sandia Report SAND86-8246.
20. P. G. Cross. *Conjugate Analysis of Two-Dimensional Ablation and Pyrolysis in Rocket Nozzles*. Ann Arbor, Michigan, 2017.
21. L. C. Scalabrin. *Numerical Simulation of Weakly Ionized Hypersonic Flow Over Reentry Capsules*. Ann Arbor, Michigan, 2007.
22. Langley Research Center. *Theoretical and Experimental Studies of Reentry Plasmas*, by M. G. Dunn and S.-W. Kang. Hampton, Virginia, Langley Research Center, 1973. NASA CR-2232.
23. Lewis Research Center. *Coefficients for Calculating Thermodynamic and Transport Properties of Individual Species*, by B. J. McBride, S. Gordon, and M. A. Reno. Cleveland, Ohio, Lewis Research Center, 1993. NASA TM 4513.
24. Glenn Research Center. *Recalibration of the Shear Stress Transport Model to Improve Calculation of Shock Separated Flows*, by N. J. Georgiadis and D. A. Yoder. Cleveland, Ohio, Glenn Research Center, 2013. NASA TM 2013-217851.
25. S. Walker and J. D. Schmisser. "CFD Validation of Shock-Shock Interaction Flow Fields," *40th AIAA Aerospace Sciences Meeting*, Reno, Nevada, January 2002. AIAA 2002-0436. DOI: 10.2514/6.2002-436.

NOMENCLATURE

°R	degrees Rankine
AIAA	American Institute of Aeronautics and Astronautics
btu/ft ² s	British thermal unit per square foot per second
CCA	continuity convergence accelerator
CFD	computational fluid dynamics
CFL	Courant-Friedrichs-Lewy
cm ³	cubic centimeters
COTS	commercial off-the-shelf
CUBRC	Calspan-University at Buffalo Research Center
deg	degrees
DSMC	direct simulation Monte-Carlo
EBU	eddy break-up
ft	feet
ft ³	cubic feet
FY	fiscal year
K	Kelvin
kft	kilofeet
kg	kilograms
lbf	pound-force
LPS	linear pressure strain
MJ	Megajoule
mol	Mole
ms	milliseconds
NASA	National Aeronautics and Space Administration
NATO	North Atlantic Treaty Organization
NAWCWD	Naval Air Warfare Center Weapons Division
NO	nitric oxide
QCR	quadratic constitutive relation
RANS	Reynolds-Averaged Navier-Stokes
RST	Reynolds stress transport

s	seconds
S&T	science and technology
S-A	Spalart-Allmaras
SST	shear stress transport

INITIAL DISTRIBUTION

- 1 Defense Technical Information Center, Fort Belvoir, VA
-

ON-SITE DISTRIBUTION

- 4 Code 4F0000D
 - Technical Library (archive copy) (2)
 - Wonnacott, W. M. (2)
- 1 Code 4G0000D (file copy)
- 18 Code 476100D
 - Cross, P. (12)
 - Gramanzini, J. (2)
 - West, M. (4)